受理
'96.12.20
電気・電子情報・
電子工学専攻

子・349

Wavelength Trimming Technology for Multiple-Wavelength Distributed-Feedback Semiconductor Laser Arrays
（多波長集積分布帰還型半導体レーザの波長トリミング技術）

A Thesis Presented
to the Graduate School of the University of Tokyo
in Partial Fulfillment of the Requirements
for the Degree of Doctor of Philosophy in Electronic Engineering

by

Tsurugi Ken SUDOH

December 20, 1996

Dissertation Supervisor

Professor Yoshiaki NAKANO

Acknowledgements

The work presented in this thesis would not have been possible without the fruitful contribution of many people.

First of all, I would like to express my deepest gratitude to my dissertation supervisor Prof. Y. Nakano for his guidance and constant encouragement he provided all along my doctoral work. I greatly appreciate valuable and insightful comments from Prof. K. Tada, Prof. T. Kamiya, Prof. Y. Arakawa, Prof., K. Kikuchi, and Prof. M. Tanaka.

I would like to thank all the members in Nakano and Tada Laboratory for their guidance, discussions, and enjoyable collaborations.

I am deeply indebted to all researchers of the Optoelectronics Laboratory, Yokogawa Electric Corporation for their kind and valuable cooperation.

The fellowship of the Japan Society for the Promotion of Science for Japanese Junior Scientists was generously supplied.

Last but not least, I would like to thank my parents for their constant encouragement.

Publications

[1] Tsurugi K. Sudoh, Mitsutaka Kumano, Yoshiaki Nakano, and Kunio Tada, "Wavelength trimming technology for multiple-wavelength distributed-feedback laser arrays by photo-absorption induced disordering", Post-Deadline Papers Technical Digest of First Optoelectronics and Communications Conference (OECC'96), post deadline paper PD2-2, pp. 18-19, Makuhari Messe, Japan, July 18, 1996.

[2] Tsurugi K. Sudoh, Yoshiaki Nakano, and Kunio Tada, "Wavelength trimming of distributed-feedback lasers by photo-induced refractive index change", Extended Abstracts of 57th Autumn Meeting, the Japan Society of Applied Physics, 9a-KH-7, no. 3, p. 972, Sept. 9, 1996.

[3] Tsurugi K. Sudoh, Mitsutaka Kumano, Yoshiaki Nakano, and Kunio Tada, "Wavelength trimming of distributed-feedback lasers by laser-induced quantum well intermixing", Extended Abstracts of 57th Autumn Meeting, the Japan Society of Applied Physics, 9a-KH-8, no. 3, p. 973, Sept. 9, 1996.

[4] Tsurugi K. Sudoh, Yoshiaki Nakano, and Kunio Tada, "Wavelength Trimming Technology for Multiple-Wavelength Distributed-Feedback Laser Arrays", Conference Digest of 15th IEEE International Semiconductor Laser Conference (ISLC'96), paper W1.5, pp. 133-134, Haifa, Israel, Oct. 16, 1996.

[5] Tsurugi K. Sudoh, Yoshiaki Nakano, and Kunio Tada, "Wavelength trimming technology for distributed-feedback lasers", The Transactions of the Institute of Electronics, Information and Communication Engineers C-I, vol. J79C-I, no. 10, pp. 400-401, Oct. 1996.

[6] Tsurugi K. Sudoh, Mitsutaka Kumano, Yoshiaki Nakano, and Kunio Tada, "Wavelength trimming of distributed-feedback lasers by photo-absorption-induced disordering", Conference Proceedings of IEEE Lasers and Electro-Optics Society 1996 Annual Meeting (LEOS'96), paper ThU4, vol. 2, pp. 419-420, Boston, MA, Nov. 21, 1996.

[7] Tsurugi K. Sudoh, Mitsutaka Kumano, Yoshiaki Nakano, and Kunio Tada, "Wavelength trimming of distributed-feedback lasers by photo-absorption-induced disordering", Technical Report of the Institute of Electronics, Informa-

tion and Communication Engineers, LQE96-112, vol. 96, no. 399, pp. 7-12, Dec. 1996.

[8] Tsurugi K. Sudoh, Yoshiaki Nakano, and Kunio Tada, "Wavelength trimming technology for multiple-wavelength distributed-feedback laser arrays by photo-induced refractive index change", Electronics Letters, vol. 33, no. 3, pp. 216-217, 1997.

[9] Tsurugi K. Sudoh, Mitsutaka Kumano, Yoshiaki Nakano, and Kunio Tada, "Wavelength trimming by photo-absorption induced disordering for multiple-wavelength distributed-feedback laser arrays", submitted to IEEE Photonics Technology Letters.

[10] Tsurugi K. Sudoh, Yoshiaki Nakano, and Kunio Tada, "Wavelength trimming by external light irradiation — post-fabrication lasing wavelength adjustment for multiple-wavelength distributed-feedback laser arrays", submitted to IEEE Journal of Selected Topics in Quantum Electronics.

Contents

1 Introduction **1**
- 1.1 Background of This Research 1
  - 1.1.1 Optical Communications 1
  - 1.1.2 Optical Sources for Wavelength-Division-Multiplexing 2
  - 1.1.3 Multiple-Wavelength DFB Laser Arrays 2
  - 1.1.4 Wavelength Reproducibility of Multiple-Wavelength DFB Laser Arrays 3
- 1.2 Purpose of This Research 4
- 1.3 Outline of This Thesis 4
- References 5

2 Proposal of Wavelength Trimming Technology **9**
- 2.1 Introduction 9
- 2.2 Wavelength Variation in DFB Lasers 9
- 2.3 Countermeasures for Wavelength Variation 10
- 2.4 Proposal of Wavelength Trimming Technology 12
- 2.5 Realization of Wavelength Trimming Technology 13
- 2.6 Conclusions 14
- References 14

3 Wavelength Trimming by Photo-Induced Refractive Index Change **16**
- 3.1 Introduction 16
- 3.2 Principle of Photo-Induced Refractive Index Change 16
- 3.3 Preparation of Chalcogenide Glass Films 17
  - 3.3.1 Film Preparation 19
  - 3.3.2 Composition 19
  - 3.3.3 Crystalline State 20
- 3.4 Characterization of Photo-Induced Refractive Index Change 20
  - 3.4.1 Principle of Spectroscopic Ellipsometry 20
  - 3.4.2 Measurement of Photo-Induced Refractive Index Change 25
- 3.5 Process Tolerance of Chalcogenide Glass Films 36
- 3.6 Proposal of Wavelength Trimming by Photo-Induced Refractive Index Change 39
- 3.7 Fabrication Procedures 42
- 3.8 Wavelength Trimming Experiment 51

3.9 Conclusions 57
References 57

4 Wavelength Trimming by Photo-Absorption-Induced Disordering 59
4.1 Introduction 59
4.2 Principle of PAID Process 60
4.3 Characterization of PAID Process 61
4.4 Device Structure and Fabrication Procedure 67
4.5 Wavelength Trimming Experiment 71
4.6 Control of PAID Process 79
  4.6.1 *in-situ* Temperature Measurement 79
  4.6.2 Spatial Distribution of Disordering 87
  4.6.3 Process Control by Absorption Photocurrent Monitoring 93
4.7 Conclusions 93
References 94

5 Wavelength Trimming by Magneto-Optic Effect 96
5.1 Introduction 96
5.2 Magneto-Optic Effect 96
5.3 Concept of Wavelength Trimming by Kerr Effect 96
5.4 Analysis of Wavelength Trimming by Kerr Effect 100
5.5 Conclusions 103
References 104

6 Conclusions 105

Appendix Coupled-Wave Theory of DFB Lasers 107
References 109

Chapter 1

Introduction

1.1 Background of This Research

This section sketches the development of optical communications and new demands for optical sources, and defines a point of origin of this research.

1.1.1 Optical Communications

A strong desire of all humankind for knowledge has driven the progress of communication systems. It is a duty, and at the same time, a dream of us the engineers who serve telecommunications to develop the system to have the ultimate capacity.

The optical fiber communication system utilizes the carrier with frequency of ~200 THz, and the optical fiber of its arterial waveguide not only has an extremely low transmission loss (~0.2 dB/km at 1.55 μm), but also has an enormously wide bandwidth (~30 THz), therefore, every our effort has been concentrated on increasing its transmission capacity towards the utmost limit [1].

Traditionally, increasing the transmission bandwidth has been accomplished by time-division-multiplexing (TDM) through the increase in the transmission speed, however, further increase is becoming difficult due to limitations in opto-electronic component speed and dispersive effects in the optical fiber.

Recently, remarkable progresses in increasing the transmission capacity have been made by wavelength-division-multiplexing (WDM). WDM is a transmission scheme in which many independent wavelength channels, each occupying a unique wavelength location, are transmitted simultaneously on a single fiber across a large network. It offers a very effective utilization of the fiber bandwidth directly in the wavelength domain, and it can help achieve a significant enhancement in aggregate transmission capacity and throughput over that of existing fiber networks [2]-[4]. Up to the present, 2.64 Tb/s (20 Gb/s × 132 channels) WDM transmission experiment over 120 km standard fiber has been demonstrated with 33.3 GHz spacing [5]. By using erbium-doped fiber amplifiers, WDM systems can be made cost-effective for certain applications relative to traditional TDM systems with electronic regenerators [6]. In addition, the wavelength adds a new function that can be used for routing and switching signals and for providing wavelength segregated services [7], [8]. These capabilities are especially attractive for optical networking [9]-[11].

1.1.2 Optical Sources for Wavelength-Division-Multiplexing

The practical deployment of WDM presents major challenges to optical source technology [12]. Wavelength division multiplexed optical transmission and networking requires laser sources with wavelength closely aligned to the pass-bands of wavelength routing elements and demultiplexing optical filters at the receiving end. Depending on the application, optical terminals may be expected to provide rapid wavelength tuning or selection, or to independently provide extraordinary wavelength precision and stability without any system-level reference.

In the present WDM system, a large number of discrete distributed-feedback (DFB) or distributed Bragg reflector (DBR) semiconductor laser diodes are used as its optical source. To take an instance, the optical source of the system mentioned above consisted of 132 modules of DFB laser diodes, multiplexers, and lithium niobate optical modulators. For WDM lightwave systems to be simple and cost effective, it is indispensable to integrate each component of the optical source [13].

In order to meet these requirements, various types of integrated InP-based sources have been proposed and developed, such as a large variety of monolithic active-filter tunable laser designs [14]-[17], several monolithic complex cavity geometrical-selection multiple-wavelength laser designs [18], [19], and multiple-wavelength DFB/DBR laser arrays [12], [13], [21]-[42]. The selection should be made on the basis of long-term longitudinal mode stability, long-term wavelength stability, wavelength switching range and speed, and manufacturing cost.

Among these options, intensive research has been done especially on a multiple-wavelength DFB laser array [12], [13], [21]-[38].

1.1.3 Multiple-Wavelength DFB Laser Arrays

Properly engineered distributed feedback laser resonators are well-known in their ability to offer exceptionally robust longitudinal mode stability, both in their long-term resistance to mode jumps with environmental and operating condition changes, and in basic side-mode suppression characteristics. Furthermore, highly temperature-stabilized DFB lasers or integrated DFB-electroabsorption modulated sources have been shown to have very low (0.1 nm-level) wavelength drift with aging over system life [43]. In a DFB laser array design, the independent, short cavities of each DFB provide a WDM source with same spectral and longitudinal mode stability of discrete DFB lasers. An array of DFB lasers can be configured with a monolithically integrated combiner and modulators to provide the simultaneous transmission from several sources for a single-channel source [13], [29], [33], [37].

Such a photonic integration not only simplifies the optical coupling between laser array and single-mode fibers but also reduces the packaging cost per wavelength since a single optical pigtailing including an optical isolator is shared by all the wavelengths.

Multiple-wavelength DFB laser arrays have been demonstrated in the 1.3 μm wavelength region [21] and in the 1.55 μm wavelength region [12], [13], [22]-[38]. A DFB laser array, with up to 21 wavelength, integrated with a star coupler and optical amplifiers has been achieved in the 1.55 μm region [13], [29], [33], [37]. To assure lasing at each Bragg wavelength in a DFB laser array, $\lambda/4$-shifted gratings are incorporated and the facet reflections are eliminated by anti-reflection coatings or slanting the rear facet [13], [21], [22]-[29], [31], [33], [37], [38]. A DFB laser array incorporating a gain-coupling mechanism has been also demonstrated [34]-[36]. The gain-coupling effect guarantees high yield of singlemode operation at predictable Bragg wavelengths. Wavelength spacings as small as 0.66 nm [24] and as large as 7 nm [25] have been reported. The maximum wavelength span is limited by the optical gain bandwidth of the active layer. The largest span of 131 nm was obtained by the use of compressively-strained multiple quantum well active layers [25]. The lasing wavelengths range from 1459.2 to 1590.6 nm, which is considerably wider than the optical bandwidth of erbium-doped fiber amplifiers (1535—1565 nm).

1.1.4 Wavelength Reproducibility of Multiple-Wavelength DFB Laser Arrays

To use the multiple-wavelength laser array in real system, its wavelengths have to match the network specification within the tolerance given by the optical bandwidth of the other wavelength-selective devices such as filters and demulti/multiplexers. The wavelength comb generated by a laser array can be moved as a group by adjusting the heat sink temperature to match the wavelength comb used in the system. Therefore, the practicality of the multiple-wavelength laser arrays depends on how well the wavelength spacing can be controlled during fabrication [12], [13], [37], [38].

Oscillation wavelength of DFB lasers is easily affected by small variations in device parameters due to inevitable fabrication error, and therefore it varies from device to device, as a consequence, prescribing oscillation wavelength is very difficult. Since all the wavelengths in an array have to fall within the range allowed by the optical bandwidth of the wavelength selective devices in the network, this insufficient wavelength reproducibility significantly limits the device yield. Consequently, external wavelength tuning by controlling temperature or carrier density individually [23], [26], [28], [31], [33], [35], [39]-[42], or wavelength redundancy where more than one laser per wavelength are incorporated [13], [37], [38], is necessary for practical use.

Multiple-electrode DFB laser arrays [23], [28], [31], DFB laser arrays with thin-film heater [26], [33], [35], or DBR laser arrays [39]-[42] can be tuned to a precise wavelength spacing or a variable wavelength spacing that is required by the network. However, active wavelength monitoring and feedback control are required since the tuning characteristics may change with aging. Besides, in terms of complexity, reliability, and cost, these countermeasures become impracticable as the number of wavelengths increases.

Thus it is desirable to use fixed multiple-wavelength DFB laser array without active wavelength control, and therefore, the securement of wavelength reproducibility is urgent and vital task for its realization.

1.2 Purpose of This Research

The purpose of this research is to give a solution to the problem in wavelength reproducibility of multiple-wavelength DFB laser arrays. In order to cope with the difficulty, we propose a concept of "wavelength trimming technology", in which a post-fabrication wavelength-error correction method without involving external control circuitry, and aim at its realization.

1.3 Outline of This Thesis

This thesis describes a concept of wavelength trimming technology and its realization method.

In Chapter 2, after summarizing the origins limiting the reproducibility of oscillation wavelength in DFB lasers, we propose the concept of wavelength trimming and describe keys for its realization.

Chapter 3 and 4 demonstrate wavelength trimming technologies by making use of a photo-induced refractive index change in chalcogenide glasses and a photo-absorption-induced quantum well disordering process. Both methods utilize the refractive index change of the material, which composes the laser waveguide, induced by external light irradiation. Chapter 5 describes another possibility of wavelength trimming through the resonant condition change instead of the refractive index change. Chapter 6 is a conclusion of this thesis.

References

[1] G. P. Agrawal, "Fiber-optic communication systems", John Wiley & Sons, Inc., New York, 1992.

[2] Special Issue on Wavelength Division Multiplexing, J. Lightwave Technol., vol. 8, no. 6, 1990.

[3] Special Issue on Broad-band Optical Networks, J. Lightwave Technol., vol. 11, no. 5-6, 1993.

[4] Special Issue on Multiwavelength Optical Technology and Networks, J. Lightwave Technol., vol. 14, no. 6, 1996.

[5] T. Ono, Y. Yano, K. Fukuchi, T. Ito, H. Yamazaki, M. Yamaguchi, and K. Emura, "Ultra-dense WDM experiment using optical duobinary signaling", Technical Report of Institute of Electronics, Information and Communication Engineers, vol. 96, no. 335, pp. 49-54, 1996.

[6] T. Li, "The impact of optical amplifiers on long-distance lightwave telecommunications", Proc. IEEE, vol. 81, pp. 1568-1579, 1993.

[7] C. A. Brackett, "Dense wavelength division multiplexing networks: Principles and applications", IEEE J. Select. Areas Commun., vol. 8, pp. 948-964, 1990.

[8] C. A. Brackett, "Is there an emerging consensus on WDM networking?", J. Lightwave Technol., vol. 14, pp. 936-941, 1996.

[9] C. A. Brackett, A. S. Acampora, J. Sweitzer, G. Tangonan, M. T. Smith, W. Lennon, K. C. Wang, and R. H. Hobbs, "A scalable multiwavelength multihop optical network: a proposal for research on all-optical networks", J. Lightwave Technol., vol. 11, pp. 736-753, 1993.

[10] S. B. Alexander, R. S. Bondurant, D. Byrne, V. W. S. Chan, S. G. Finn, R. Gallager, B. S. Galnce, H. A. Haus, P. Humblet, R. Jain, I. P. Kaminow, M. Karol, R. S. Kennedy, A. Kirby, H. Q. Le, A. A. M. Saleh, B. A. Schofield, J. H. Shapiro, N. K. Shankaranararyanan, R. E. Thomas, R. C. Williamson, and R. W. Wilson, "A precompetitive consortium on wide-band all optical networks", J. Lightwave Technol., vol. 11, pp. 714-735, 1993.

[11] P. E. Green, L. A. Coldren, K. M. Johnson, J. G. Lewis, C. M. Miller, J. F. Morrison, R. Olshansky, R. Ramaswami, and E. H. Smith, Jr., "All-optical packet-switched metropolitan-area network proposal", J. Lightwave Technol., vol. 11, pp. 754-763, 1993.

[12] T. L. Koch, "Laser sources for wavelength division multiplexing", Tech. Dig. 10th Int. Conf. on Intedrated Optics and Optical Fibre Communication (IOOC'95), vol. 2. WB1-1, pp. 38-39, Hong Kong, June 1995.

[13] C. E. Zah, B. Pathak, F. Favire, P. S. D. Lin, N. C. Andreadakis, R. Bhat, C.

Caneau, L. Curtis, D. D. Mahoney, W. C. Young, and T. P. Lee, “Monolithic integrated multiwavelength laser array for WDM lightwave systems”, J. Optoelectron.-Devices and Technol., vol. 9, pp. 153-166, 1994.

[14] R. C. Alferness, U. Koren, L. L. Buhl, B. I. Miller, M. G. Young, T. L. Koch, G. Raybon, and C. A. Burrus, “Broadly tunable InGaAsP/InP laser based on a vertical coupler filter with 57-nm tuning range”, Appl. Phys. Lett., vol. 60, pp. 3209-3211, 1992.

[15] Z. M. Chuang and L. A. Coldren, “Design of widely tunable semiconductor lasers using grating-assisted codirectional-coupler filters”, IEEE J. Quantum Electron., vol. 29, pp. 1071-1080, 1993.

[16] Y. Tohmori, F. Kano, H. Ishii, Y. Yoshikuni, and Y. Kondo, “Wide tuning with narrow linewidth in DFB lasers with superstructure grating (SSG)”, Electron. Lett., vol. 29, pp. 1350-1352, 1993.

[17] M. C. Amann, B. Borchert, S. Illek, and T. Wolf, “Widely tunable distributed forward coupled (DFC) laser”, Electron. Lett., vol. 29, pp. 793-794, 1993.

[18] J. B. D. Soole, K. Poguntke, A. Scherer, and H. P. LeBlanc, “Multistripe array grating integrated cavity (MAGIC) laser: a new semiconductor laser for WDM applications”, Electron. Lett., vol. 28, pp. 1805-1807, 1992.

[19] B. Glance, I. P. Kaminow, and R. W. Wilson, “Applications of the integrated waveguide grating router”, J. Lightwave Technol., vol. 12, pp. 957-962, 1994.

[20] M. Zirngible, C. H. Joyner, C. R. Doerr, L. W. Stulz, and H. M. Presby, “An 18-channel multifrequency laser”, IEEE Photon. Technol. Lett., vol. 8, pp. 870-872, 1996.

[21] H. Okuda, Y. Hirayama, H. Furuyama, J. Kinoshita, and M. Nakamura, “Five-wavelength integrated DFB laser arrays with quarter-wave-shifted structures”, IEEE J. Quantum Electron., vol. QE-23, pp. 843-848, 1987.

[22] M. Nakao, K. Sato, T. Nishida, T. Tamamura, A. Ozawa, Y. Saito, I. Okada, and H. Yoshihara, “1.55 μm DFB laser array with λ/4-shifted first-order gratings fabricated by X-ray lithography”, Electron. Lett., vol. 25, pp. 148-149, 1989.

[23] H. Yasaka, J. Nakano, M. Fukuda, Y. Nakano, and Y. Itaya, “Optical frequency spacing tunable four-channel integrated 1.55 μm multielectrode distributed-feedback laser array”, IEEE Photon. Technol. Lett., vol. 1, pp. 75-76, 1989.

[24] M. Nakao, K. Sato, T. Nishida, T. Tamamura, “Distributed feedback laser arrays fabricated by synchrotron orbital radiation lithography”, IEEE J. Sel. Areas Commun., vol. 8, pp. 1178-1182, 1990.

[25] C. E. Zah, P. S. D. Lin, F. Favire, B. Pathak, R. Bhat, C. Caneau, A. S. Gozdz, N. C. Andreadakis, M. A. Koza, T. P. Lee, T. C. Wu, and K. Y. Lau, “1.5 μm

compressive-strained multiquantum-well 20-wavelength distributed-feedback laser arrays", Electron. Lett., vol. 28, pp. 824-826, 1992.

[26] L. A. Wang, Y. H. Lo, A. S. Gozdz, P. S. D. Lin, M. Z. Iqbal, and R. Bhat, "Integrated four-wavelength DFB laser array with 10 Gb/s speed and 5 nm continuous tuning range", IEEE Photon. Technol. Lett., vol. 4, pp. 318-320, 1992.

[27] C. E. Zah, B. Pathak, F. Favire, R. Bhat, C. Caneau, P. S. D. Lin, A. S. Gozdz, N. C. Andreadakis, M. A. Koza, T. P. Lee, "1.5 μm tensile-strained single quantum well 20-wavelength distributed feedback laser arrays", Electron. Lett., vol. 28, pp. 1585-1587, 1992.

[28] T. Ohishi, H. Watanabe, M. Kawano, A. Takemoto, Y. Nakajima, E. Omura, M. Aiga, and K. Ikeda, "Wavelength tunable 4-element laser array", Proc. SPIE, vol. 1634, pp. 258-265, 1992.

[29] C. E. Zah, F. J. Favire, B. Pathak, R. Bhat, C. Caneau, P. S. D. Lin, A. S. Gozdz, N. C. Andreadakis, M. A. Koza, T. P. Lee, "Monolithic integration of multiwavelength compressive-strained multiquantum-well distributed-feedback laser array with star coupler and optical amplifiers", Electron. Lett., vol. 28, pp. 2361-2362, 1992.

[30] L. M. Miller, K. J. Beernink, J. S. Hughes, S. G. Bishop, and J. J. Coleman, "Four wavelength distributed feedback ridge waveguide quantum-well heterostructure laser array", Appl. Phys. Lett., vol. 61, pp. 2964-2966, 1992.

[31] K. Sato, S. Sekine, Y. Kondo, and M. Yamamoto, "Simultaneous operation of ten-channel tunable DFB laser arrays using strained-InGaAsP multiple quantum wells", IEEE J. Quantum Electron., vol.29, pp. 1805-1809, 1993.

[32] M. Aoki, T. Taniwatari, M. Suzuki, and T. Tsutsui, "Detuning adjustable multiwavelength MQW-DFB laser array grown by effective index/quantum energy control selective area MOVPE", IEEE Photon Technol. Lett., vol. 6, pp. 789-791, 1994.

[33] M. G. Young, U. Koren, B. I. Miller, M. Chien, T. L. Koch, D. M. Tennant, K. Feder, K. Dreyer, and G. Raybon, "Six wavelength laser array with integrated amplifier and modulator", Electron. Lett., vol. 31, pp. 1835-1836, 1995.

[34] G. P. Li, T. Makino, and C. M. Wu, "Multi- λ ridge waveguide gain-coupled DFB laser array", J. Lightwave Technol., vol. 13, pp. 196-199, 1995.

[35] G. P. Li, T. Makino, A. Sarangan, and W. Huang, "16-wavelength gain-coupled DFB laser array with fine tunability", IEEE Photon. Technol. Lett., vol. 8, pp. 22-24, 1996.

[36] A. M. Sarangan, W. P. Huang, T. Makino, G. P. Li, "Wavelength control in DFB laser arrays by tilting the ridge with respect to the gratings", IEEE Photon. Technol. Lett., vol. 8, pp. 1435-1437, 1996.

[37] C. E. Zah, M. R. Amersfoort, B. Pathak, F. Favire, P. S. D. Lin, A. Rajhel, N. C. Andreadakis, R. Bhat, C. Caneau, and M. A. Koza, "Wavelength accuracy and output power of multiwavelength DFB laser arrays with integrated star couplers and optical amplifiers", IEEE Photon. Technol. Lett., vol. 8, pp. 864-866, 1996.

[38] T. P. Lee, C. E. Zah, R. Bhat, W. C. Young, B. Pathak, F. Favire, P. S. D. Lin, N. C. Andreadakis, C. Caneau, A. W. Rahjel, M. Koza, J. K. Gamelin, L. Curtis, D. D. Mahoney, and A. Lepore, "Multiwavelength DFB laser array transmitters for ONTC reconfigurable Optical Network Testbed", J. Lightwave Technol., vol. 14, pp. 967-976, 1996.

[39] U. Koren, T. K. Koch, B. I. Miller, G. Eisenstein, and R. H. Bosworth, "Wavelength division multiplexing light source with integrated quantum well tunable lasers and optical amplifiers", Appl. Phys. Lett., vol. 54, pp. 2056-2058, 1989.

[40] M. Yamaguchi, T. Sasaki, H. Asano, T. Kato, M. Kitamura, and I. Mito, "Semiconductor photonic integrated circuit for high-density WDM light source", Tech. Dig. 12th IEEE Int. Semiconductor Laser Conf., Davos, Switzerland, pp. 160-161, 1990.

[41] J. M. Verdiell, T. L. Koch, D. M. Tennant, K. Feder, R. P. Gnall, M. G. Young, B. I. Miller, U. Koren, M. A. Newkirk, and B. Tell, "8-wavelength DBR laser array fabricated with a single-step Bragg grating printing technique", IEEE Photonics Technol. Lett., vol. 5, pp. 619-621, 1993.

[42] Y. Katoh, T. Kunii, Y. Matsui, H. Wada, T. Kamijoh, and Y. Kawai, "DBR laser array for WDM system", Electron. Lett., vol. 29, pp. 2195-2197, 1993.

[43] Y. C. Chung, J. Jeong, and L. S. Cheng, "Aging-induced wavelength shifts in 1.5-μm DFB lasers", IEEE Photon. Technol. Lett., vol. 6, pp. 792-795, 1994.

Chapter 2

Proposal of Wavelength Trimming Technology

2.1 Introduction

Oscillation wavelength of DFB lasers is easily affected by small variation in device parameters, and therefore, prescribing oscillation wavelength is very difficult. This insufficient wavelength reproducibility limits the device yield, specifically, in multiple-wavelength DFB laser arrays whose element needs to have lasing wavelength that matches pre-defined wavelength-division-multiplexed channels.

In this chapter, we propose a novel concept to manage this problem in multiple-wavelength DFB laser arrays, namely, wavelength trimming technology, where the oscillation wavelength error is corrected after the device fabrication without using external active tuning.

Section 2.2 summarizes a present state of the reproducibility of oscillation wavelength in DFB lasers. Section 2.3 describes the countermeasures for oscillation wavelength variation in DFB lasers and their problems. In Section 2.4, we propose a concept of trimming technology for oscillation wavelength error correction in DFB lasers. Finally, we describe keys for its realization in Section 2.5.

2.2 Wavelength Variation in DFB Lasers

Oscillation wavelength of DFB lasers is basically given by the Bragg relation,

$$\lambda = 2n_{eff}\Lambda \qquad (2.1)$$

where λ is the oscillation wavelength, n_{eff} is the effective refractive index which is determined by the laser waveguide structure and its parameters, such as width W, the layer thickness t, and the composition λ_{PL}, and Λ is the period of the diffraction grating, respectively. To put it more precisely, it obeys the coupled-wave theory [1], therefore, besides those parameters described above, the coupling coefficient, its longitudinal distribution, and relative position of the cleaved facets to the grating phase (facet phases) affect the oscillation wavelength. The coupled-wave theory and its threshold analysis are summarized in Appendix. These parameters fluctuate due to inevitable fabrication errors, which results in the oscillation wavelength variation [2], [3].

The change in oscillation wavelength through variation in device parameters can be expressed as

$$\Delta\lambda = \frac{\lambda}{n_g}\left(n_{eff}\frac{\Delta\Lambda}{\Lambda} + \frac{\partial n_{eff}}{\partial t}\Delta t + \frac{\partial n_{eff}}{\partial W}\Delta W + \frac{\partial n_{eff}}{\partial \lambda_{PL}}\Delta\lambda_{PL} - \frac{\lambda\alpha}{4\pi}\Delta g_{th} \right) \qquad (2.2)$$

where n_g is a group refractive index that is an effective refractive index including a wavelength dispersion defined as,

$$n_g = n_{eff} - \lambda\frac{\partial n_{eff}}{\partial \lambda} \qquad (2.3)$$

Moreover the wavelength shift is caused by the change in threshold gain Δg_{th} which can be written as

$$\Delta\lambda = -\frac{\lambda^2 a}{4\pi n_g}\Delta g_{th} \qquad (2.4)$$

where a is the linewidth enhancement factor. Therefore, the total amount of the oscillation wavelength change is the sum of equations (2.2) and (2.4).

TABLE 2.1 shows the wavelength variation caused by the variation of structure parameters which was analyzed by Y. Kotaki and H. Ishikawa, in 1991 [2]. A 1.55 μm wavelength DFB laser with a bulk active layer, a buried heterostructure, cavity of 300 μm long, and λ/4-shifted grating with AR coated facets were assumed. Variations in structure parameters are the values obtained from assuming the use of liquid phase epitaxy and wet chemical etching techniques, these are commonly used for commercially available InGaAsP/InP lasers. The results predict that the lasing wavelengths are scattered over ±7.4 nm.

Although there have been significant improvements in the epitaxial growth and dry etching technologies [4]-[6], which make it possible to perform the uniform growth and the precise control of grating depth and stripe width, the current wavelength reproducibility of DFB lasers is still insufficient. Therefore, selection from a number of devices as well as the external active tuning of wavelength is indispensable for practical use. This problem significantly limits the device yield, particularly, in multiple-wavelength DFB laser arrays whose wavelengths have to be aligned with pre-defined channels in WDM lightwave systems.

2.3 Countermeasures for Wavelength Variation

In this section, we summarize the countermeasures for oscillation wavelength variation in DFB lasers and their problems.

The straightforward way is the improvement of global uniformity in growth and fabrication. As mention in the previous section, in spite of significant improvements in the epitaxial growth and dry etching technologies, the uniformity is still

TABLE 2.1 Wavelength variation of 1.55 μm λ/4 phase shifted DFB laser.

Paramter	Variation	Wavelength variation
Active layer width	±20 %	±2.8 nm
Active layer thickness	±17 %	±6.3 nm
Guide layer thickness	±17 %	±1.3 nm
Active layer composition	±0.6 %	±2.0 nm
Guide layer compostion	±0.9 %	±0.5 nm
Grating depth	±22 %	±0.8 nm
Grating shape	sin–rectangular, 30 %	±0.6 nm
Grating pitch	±0.1 nm	±0.7 nm
The total wavelength variation		±7.4 nm

insufficient.

On the other hand, local processing and epitaxy uniformity are remarkably better than the wafer-wide uniformity [7], [8]. Although considerable improvements have been demonstrated by integrating each DFB laser closely within a small local area, wavelength precision is still a great concern.

The array yield can be improved by assigning more than one laser per wavelength. This method is called the built-in wavelength redundancy [8]. Among redundant lasers, the one with its lasing wavelength closest to the designated system wavelength is selected to be wire bonded for final packaging. This method makes a prominent contribution to the wavelength accuracy required for the multiple-wavelength laser arrays, however, as the number of wavelengths increases, it becomes impracticable in terms of size and hence cost.

Other methods are the external active tuning of oscillation wavelength of each DFB laser through the change in refractive index caused by changes of temperature [7], [9], [10], or carrier density [11]-[13].

The index change due to the temperature is approximately 2×10^{-4} K^{-1} in InGaAsP/InP at room temperature. Therefore, the change in oscillation wavelength caused by the temperature change is 0.1 nm/K. Wavelength tuning by temperature is very simple, thus it is universally used for adjustment of oscillation wavelength of discrete DFB lasers. However, the temperature change affects the threshold current and differential efficiency of the laser diodes. In the multiple-wavelength laser arrays, although it is possible to adjust each wavelength by placing the thin film heaters on every laser [9], [10], it is impractical from the point of view of complexity and reliability of systems and power consumption.

The index change by carrier injection is caused by plasma and band filling effects. The maximum carrier induced change in effective refractive index Dneff is approximately $2\text{-}3\times10^{-2}$. Thus, the large amount of wavelength shift (~10 nm at 1.55 μm) can be obtained. In conventional DFB lasers, the carrier density inside the cavity is always clamped at the threshold condition, thus, the wavelength tuning through carrier injection is realized in the multisection DFB lasers where nonuniform injection is possible. Using the integration of multielectrode DFB lasers [11]-[13], each oscillation wavelength can be adjusted independently, however, again, it is impractical from the point of view of complexity and reliability of systems.

2.4 Proposal of Wavelength Trimming Technology

As described in the previous section, the external active tuning of oscillation wavelength of each DFB laser can not be applicable to practical multiple-wavelength

DFB laser arrays.

On the other hand, in analog integrated circuits (IC) like operational amplifiers, there is "offset voltage trimming" commonly used, where the variation in output characteristics is corrected at the inspection stage after complete device fabrication [14], [15]. The offset voltage is an error voltage appeared at the output port even when the two inputs are shorted. This error voltage is caused by parameter variation and temperature gradient in the integrated circuits, and it must be canceled in applications where the high-DC-precision is necessary.

There are two ways of canceling the offset voltage; one is external tuning and the other is internal compensation.

The former method utilizes external circuitry including a potentiometer to eliminate the offset. Although flexibility is high in this method, the circuits require space and cost. Furthermore, temperature drift caused by the external circuitry must be considered.

In the internal compensation method, on the other hand, a part of on-chip thin-film resistor is "trimmed" off at the inspection stage by a high-power laser such as the Nd: YAG laser, until the offset voltage (measured simultaneously) becomes zero. Thereby, users can utilize the operational amplifier without taking care of the offset voltage.

Our "wavelength trimming" concept came from an analogy to this "offset trimming". The wavelength trimming technology is a post-fabrication wavelength-error correction in DFB lasers where no external active tuning is necessary.

2.5 Realization of Wavelength Trimming Technology

Next, we describe keys for realization of the wavelength trimming. As described in Section 2.2, the oscillation wavelength of DFB laser is affected by various parameters, such as the effective refractive index, the period of the diffraction grating, the coupling coefficient, its longitudinal distribution, and facet phases. Therefore, the oscillation wavelength adjustment can be realized by changing at least one among those parameters. In analogue IC, a high-power laser such as the Nd: YAG laser is used for trimming off a part of on-chip thin-film resistor to compensate the output error. The same technique can not be used for trimming of a part of the laser structure in optoelectronic devices, since the roughness and moreover the fatal damage might be induced by the irradiation of high-power laser. Accordingly, the key issue for embodying the concept of wavelength trimming is how to incorporate a material whose optical property is changeable after the device fabrication by a simple and low temperature process into the laser waveguide. This process should not induce any physical damage in the laser. Furthermore, long-term stability of the optical properties after processing is also requested.

On the basis of consideration described above, we have examined the possibility of wavelength trimming by a photo-induced refractive index change in chalcogenide glasses, a photo-absorption-induced quantum well disordering, and a magneto-optic effect. First two methods utilize the refractive index change of the material, which composes the laser waveguide, by the external light irradiation. The last method makes use of the resonant condition change. These methods enable the wavelength trimming without involving any physical damage in the laser. Following chapters describe those methods.

2.6 Conclusions

In this chapter, after summarizing the problem in wavelength reproducibility of DFB lasers, we have proposed a wavelength trimming technology for multiple-wavelength DFB laser arrays. Here we repeat once again, this is a post-fabrication wavelength-error correction in DFB lasers where no external active tuning is necessary. We have also described the keys to realizing this concept.

References

[1] H. Kogelnik and C. V. Shank, "Coupled-wave theory of distributed feedback lasers", J. Appl. Phys., vol. 43, pp. 2327-2335, 1972.

[2] Y. Kotaki and H. Ishikawa, "Wavelength tunable DFB and DBR lasres for coherent optical fibre communications", IEE Proc.-J, vol. 138, 1991.

[3] C. E. Zah, B. Pathak, F. Favire, P. S. D. Lin, N. C. Andreadakis, R. Bhat, C. Caneau, L. Curtis, D. D. Mahoney, W. C. Young, and T. P. Lee, "Monolithic integrated multiwavelength laser array for WDM lightwave systems", J. Optoelectron.-Devices and Technol., vol. 9, pp. 153-166, 1994.

[4] A. Katz, ed., "Indium phosphide and related materials: processing, technology, and devices", Artech House, Boston, London, 1992.

[5] T. L. Koch, P. J. Corvini, U. Koren, and W. T. Tsang, "Wavelength uniformity of 1.3 μm GaInAsP/InP distributed Bragg reflector lasers with hybrid beam/vapour epitaxial growth", Electronics Letters, vol. 24, pp. 822-823, 1988.

[6] A. J. Karter, B. Thomas, D. V. Morgan, J. K. Bhardwaj, A. M. McQuarrie, and M. A. Stephens, "Dry etching of GaAs and InP for optoelectronic devices", IEE Proc.-J., vol. 136, pp. 2-5, 1989.

[7] M. G. Young, U. Koren, B. I. Miller, M. Chien, T. L. Koch, D. M. Tennant, K.

Feder, K. Dreyer, and G. Raybon, "Six wavelength laser array with integrated amplifier and modulator", Electron. Lett., vol. 31, pp. 1835-1836, 1995.

[8] C. E. Zah, M. R. Amersfoort, B. Pathak, F. Favire, P. S. D. Lin, A. Rajhel, N. C. Andreadakis, R. Bhat, C. Caneau, and M. A. Koza, "Wavelength accuracy and output power of multiwavelength DFB laser arrays with integrated star couplers and optical amplifiers", IEEE Photon. Technol. Lett., vol. 8, pp. 864-866, 1996.

[9] L. A. Wang, Y. H. Lo, A. S. Gozdz, P. S. D. Lin, M. Z. Iqbal, and R. Bhat, "Integrated four-wavelength DFB laser array with 10 Gb/s speed and 5 nm continuous tuning range", IEEE Photon. Technol. Lett., vol. 4, pp. 318-320, 1992.

[10] G. P. Li, T. Makino, A. Sarangan, and W. Huang, "16-wavelength gain-coupled DFB laser array with fine tunability", IEEE Photon. Technol. Lett., vol. 8, pp. 22-24, 1996.

[11] H. Yasaka, J. Nakano, M. Fukuda, Y. Nakano, and Y. Itaya, "Optical frequency spacing tunable four-channel integrated 1.55 μm multielectrode distributed-feedback laser array", IEEE Photon. Technol. Lett., vol. 1, pp. 75-76, 1989.

[12] T. Ohishi, H. Watanabe, M. Kawano, A. Takemoto, Y. Nakajima, E. Omura, M. Aiga, and K. Ikeda, "Wavelength tunable 4-element laser array", Proc. SPIE, vol. 1634, pp. 258-265, 1992.

[13] K. Sato, S. Sekine, Y. Kondo, and M. Yamamoto, "Simultaneous operation of ten-channel tunable DFB laser arrays using strained-InGaAsP multiple quantum wells", IEEE J. Quantum Electron., vol.29, pp. 1805-1809, 1993.

[14] G. A. Hardway and C. C. Callihan, "Laser precision adjustment of cermet resistors in production", Solid State Technol., vol.11, pp. 29-32, 1968.

[15] T. Ngo, R. Hester, "Op amp combining precision, high speed, and high output current drive for ±5-V power supply operation", IEEE J. Solid-State Circuits, vol.25, pp. 856-862, 1990.

Chapter 3

Wavelength Trimming by Photo-Induced Refractive Index Change

3.1 Introduction

As described in Chapter 2, the key to realize the wavelength trimming is how to incorporate a material whose optical property is changeable by simple and low temperature process into the laser waveguide. In this chapter, we will examine a method which enables the wavelength trimming through the refractive index change induced by the external light irradiation. This method utilizes the chalcogenide glasses having the refractive index change induced by the light irradiation, which is called the photo-induced refractive index change, as a part of the waveguide.

In Section 3.2, the principle of the photo-induced refractive index change in chalcogenide glasses is summarized. In Section 3.3, the preparation of the chalcogenide glass films and its characterizations in terms of the composition and the crystalline state are described. The photo-induced refractive index change of chalcogenide glass films is characterized in Section 3.4. We also evaluate the chalcogenide glass film concerning the process tolerance in Section 3.5. In Section 3.6, we propose a wavelength trimming by making use of the photo-induced refractive index change. After summarizing the requirements for the device structure which enables the wavelength trimming through the photo-induced refractive index change, we propose a variety of concepts of device structures incorporated with the chalcogenide glass. From various possibilities, we have selected a mesa waveguide structure where the chalcogenide glass film is loaded at the side of the active layer. The design of the waveguide based on this structure is also shown. In Section 3.7, fabrication procedures of a mesa waveguide DFB laser is detailed. Finally, the demonstration of the wavelength trimming is presented in Section 3.8.

3.2 Principle of Photo-Induced Refractive Index Change

The chalcogenide glasses are the compounds that contain sulfur, selenium, and tellurium. The refractive index of selenium- or sulfur-based arsenic-sulfide or arsenic-germanium-selenide chalcogenide glasses are changeable through the light irradiation with energy larger than its band gap, and through heat treatment around the glass transition temperature. This phenomenon is known as "photo-induced refractive index change" [1]-[10].

The research on the chalcogenide glass has a long history and hence many physical properties such as the crystalline state, electrical and optical properties are investigated in detail. Intensive research has been done especially on the photo-induced refractive index change with regard to the application to the optical memory [1]-[4]. At the early stage of this research, the photo-induced refractive index change was used for the phase-tuning of the optical directional coupler where the chalcogenide glass was loaded on one of the two waveguides formed in a $LiNbO_3$ substrate and irradiated by a halogen lamp to change its refractive index after the device fabrication [5], [7]. This is the first implementation of the trimming technology in optoelectronic devices. The direct writing of optical waveguide and the diffraction grating by light or electron beam irradiation in planar uniform chalcogenide glass films deposited on substrates have been also demonstrated [6].

The photo-induced refractive index change in chalcogenide glasses arises from microscopic structural change inherent in amorphous materials, where a number of metastable atomic states exist and transition between different states is easily induced by applying external energy. The structural change is not the phase transition which is accompanied by the crystallization.

A schematic diagram of photo-induced refractive index change is illustrated in Fig. 3.1 [10]. Three states exist, namely, an as-deposited, an irradiated and an annealed states. Solid and dotted arrows denote the changes induced by irradiation and annealing, respectively. The refractive index changes between the as-deposited and other two states are an irreversible transition. It means that once the refractive index is changed from as-deposited value through the light irradiation or heat treatment, it is impossible to restore to the initial value. On the other hand, the transition between the irradiated and the annealed states is a reversible, thus both of the states can be repeatedly realized through the light irradiation and heat treatment.

We apply this refractive index change through the external light irradiation or the heat treatment to the wavelength trimming.

3.3 Preparation of Chalcogenide Glass Films

As described in the previous section, the refractive index of Se/S-based As-S or As-Se-Ge chalcogenide glasses is changeable through the light irradiation and heat treatment. In these glasses, arbitrary compositions of combinations of As, S, Se, and Ge are possible. We have selected two compounds, specifically, As_2S_3 and $As_4Se_5Ge_1$, and characterized these materials.

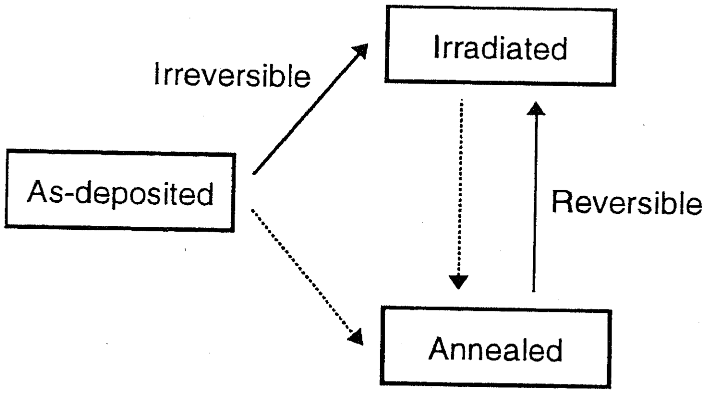

Fig. 3.1 A schematic diagram of photo-induced refractive index changes. Solid and dotted arrows denote the changes induced by irradiation and annealing, respectively.

3.3.1 Film Preparation

The As_2S_3 and the $As_4Se_5Ge_1$ chalcogenide glass films with 200 nm thickness were deposited on (100)-oriented Silicon substrates by thermal evaporation, with the background pressure of 4×10^{-4} Pa and the deposition rate of 0.5 nm/sec.

The thickness of the film and the deposition rate were controlled by using the crystal thickness monitor where the change in resonance frequency of the crystal oscillator placed inside the chamber beside the substrate, which corresponded to the product of the density of the deposited material and its thickness change, was monitored. The densities of 3.20 and 4.64 g/cm^3 were used for the As_2S_3 and the $As_4Se_5Ge_1$, respectively.

The native oxide of the Si substrate was removed with buffered hydrofluoric acid just before loading it into the thermal evaporator. A tungsten basket covered with alumina was used as the container of evaporation source materials. The distance between the source and the substrate was adjusted to about 25 cm. No heat was applied to the substrate during the evaporation.

In case that the deposition rate was too high (> 4 nm/sec), the substrate was covered with a filamentous material due to the rapid cooling of source materials during the evaporation.

3.3.2 Composition

Although both materials have approximately the same melting temperature of 360 °C, since the partial pressure of each component atom is different because of different melting temperature (arsenic: 814 °C, sulfur: 115 °C, selenium: 1539 °C, and germanium: 937 °C), the composition of the films prepared by the thermal evaporation deviates from the source material composition, which may result in change of photo-induced refractive index characteristics.

We evaluated the composition of the films by using the wavelength dispersion X-ray spectroscopy (WDX) with the source materials as references. The electron probe micro-analyzer (EPMA; SHIMADZU, EPMA-C1) having the ability to analyze the element from $_5B$ to $_{92}U$ was used.

The principle of the WDX is described below. In the EPMA, the characteristic X-rays of the sample are pumped by the electron beam irradiation. These characteristic X-rays are introduced to the X-ray monochromator to separate into each line and then their intensities are measured. The composition of the sample can be determined by the ratio of intensities of the sample to those of reference material whose composition is known.

TABLE 3.1 lists the measured intensities of the characteristic X-rays of As (Lα), S (Kα), Se (Lα), and Ge (Kα) from the sources and the films. The measurement conditions are summarized below. The acceleration voltage, the probe diameter, and the source current were 15 kV, -100 μm, and 220 μm, respectively. From TABLE 3.1, the compositions of films are readily derived and they are listed in TABLE 3.2.

In the As_2S_3 film, S is rich because of the high partial pressure of S. On the other hand, in the $As_4Se_5Ge_1$ film, the deviations are within 10 % except Ge.

Although the composition might be better controlled by optimizing the deposition rate, it is left for a future task and we decided to use these materials for the following experiments.

3.3.3 Crystalline State

We also evaluated the crystal state qualitatively by using the X-ray diffractometry (RIGAKU, RINT1000). Measurement conditions are listed in TABLE 3.3. Measured X-ray diffraction of Si substrate is shown in Fig. 3.2. Peaks found around 30 ° and 70 ° corresponded to (111) and (400) surfaces of Si substrate, respectively. Figures 3.3 (a) and (b) shows the measured X-ray diffraction of As_2S_3 and $As_4Se_5Ge_1$, respectively. No sharp peak of the crystal state is found except the peaks of the Si-substrate. Small broad peaks pointed by arrows are found around 15 ° and 30 ° in Fig. 3.3 (a) and 15 °, 30 °, and 50 ° in Fig. 3.3 (b). These peaks are called the halo peaks originated in the short range order of microscopic structure in amorphous states [11]. From these results, we have concluded that the chalcogenide glass films evaporated on the Si substrates were not the poly-crystal but the amorphous.

3.4 Characterization of Photo-Induced Refractive Index Change

Next we describe a characterization of the photo-induced refractive index changes of the chalcogenide glass films prepared in the previous section. The refractive index was measured by using the spectroscopic ellipsometry. In this section, we first explain the principle of the refractive index measurement by using the spectroscopic ellipsometry, and then show the experimental procedures and the results of the measurement of the photo-induced refractive index change.

3.4.1 Principle of Spectroscopic Ellipsometry

The principle of ellipsometry is based on the change in polarization of light induced

TABLE 3.1 Intensities of characteristic X-rays of each element of the evaporated chalcogenide glasses measured by the wavelength dispersion X-ray spectroscopy.

Compound	Element	Intensity	
		Source	Film
As_2S_3	As (Lα)	1431.3	2811.4
	S (Kα)	902.6	2514.8
$As_4Se_5Ge_1$	As (Lα)	2229.0	2691.7
	Se (Lα)	2864.4	3295.2
	Ge (Kα)	36.1	66.6

TABLE 3.2 Compositions of the chalcogenide glass films.

Compound	Element	Composition	
		Source	Film
As_2S_3	As	0.4	0.32
	S	0.6	0.68
$As_4Se_5Ge_1$	As	0.4	0.39
	Se	0.5	0.46
	Ge	0.1	0.15

TABLE 3.3 Measured conditions of X-ray diffractometry.

Tube	Cu
Tube Voltage	44 kV
Tube Current	30 mA
Goniometer	Wide Angle Goniometer
Sampling Angle	0.200 °
Scan Speed	2.00 °
Scan Axis	2θ/θ
Offset Angle	0.000 °
Attachment	Standard Sample Holder
Monochromator	Use
Monochromator Slit Width	0.60 mm
Divergence Slit Width	1/2 °
Dispersion Slit Width	1/2 °
Detection Slit Width	0.30 mm

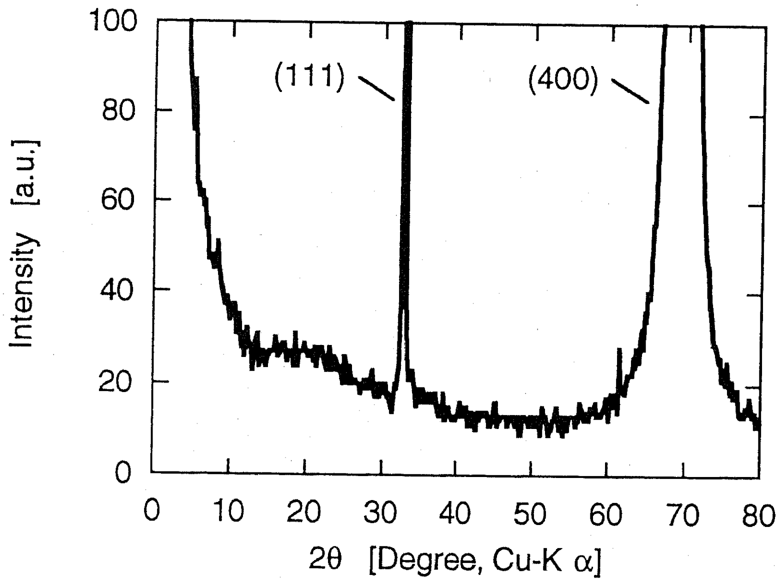

Fig. 3.2 Measured X-ray diffraction of the (100)-oriented Si substrate.

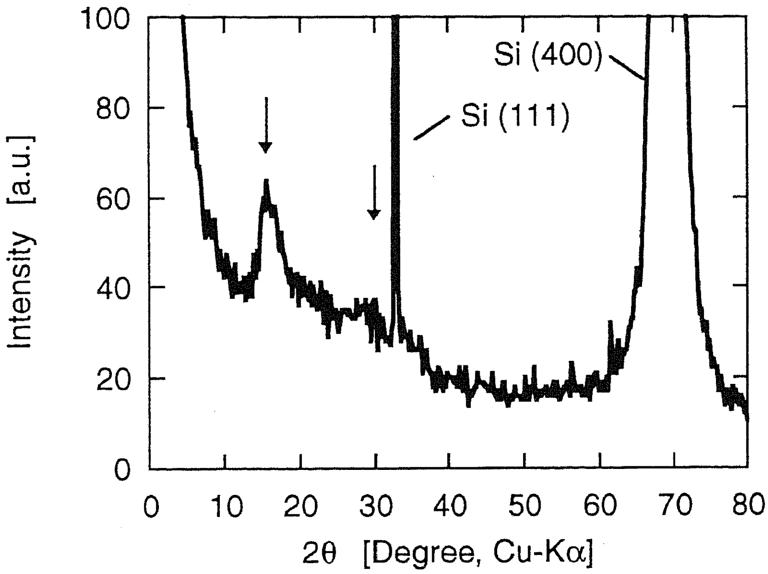

(a) As_2S_3

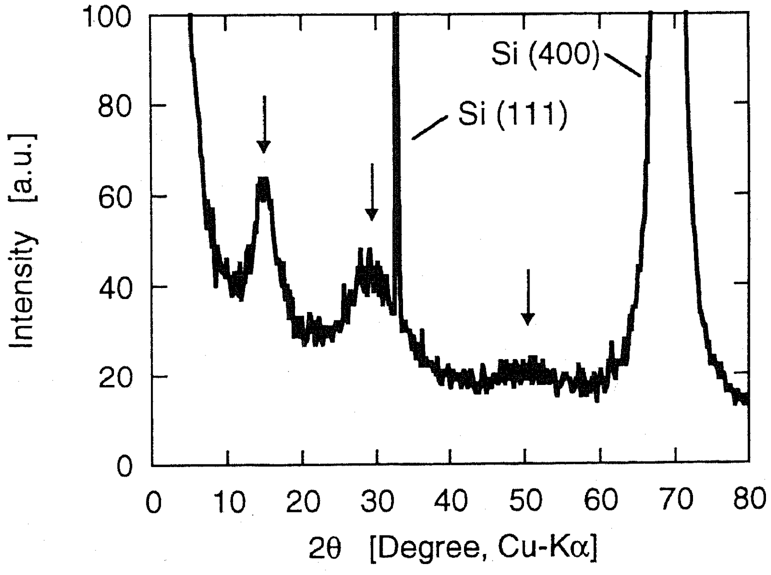

(b) $As_4Se_5Ge_1$

Fig. 3.3 X-ray diffraction of the (a) As_2S_3 and (b) $As_4Se_5Ge_1$ films deposited on the (100)-oriented Si substrate.

by the reflection from a sample surface. This change can be related to the optical properties of the reflecting material. In the most common experimental configuration for ellipsometry, linearly polarized light is incident on a surface and the polarization state of the reflected light, which is in general elliptically polarized, is analyzed. Fig. 3.4 shows the principle of ellipsometric measurements [12].

Here we formulate the relation between the measured polarization state and the refractive index. The polarization state can be expressed as the ratio of the complex reflectivities

$$\rho = \frac{r_p}{r_s}, \qquad (3.1)$$

where the subscripts p and s refer to the plane wave electric fields components, respectively, parallel and perpendicular to the plane of incidence. The polarization state is commonly expressed using ellipsometric angles of Ψ and Δ defined as

$$\rho = \frac{|r_p|}{|r_s|}\exp\left[-j\left(\delta_p - \delta_s\right)\right] \qquad (3.2)$$

$$= \tan\Psi \exp(j\Delta). \qquad (3.3)$$

In the spectroscopic ellipsometry, the ellipsometric ratio ρ is measured as a function of the photon energy E.

The complex dielectric function $\varepsilon(E)$ of a material can be deduced from equation (3.1), in the case of an interface with a semi-infinite homogeneous medium, and it is given by

$$\varepsilon(E) = \varepsilon_r(E) + j\varepsilon_i(E) \qquad (3.4)$$

$$= \sin^2\Phi_0\left[1 + \tan^2\Phi_0\frac{(1-\rho)^2}{(1+\rho)^2}\right] \qquad (3.5)$$

where Φ_0 is the angle of incidence.

The relation between the complex dielectric function ε and the complex refractive index N is

$$N(E) = n(E) + jk(E) \qquad (3.6)$$

$$= \sqrt{\varepsilon(E)}, \qquad (3.7)$$

thus the real and the imaginary part of the complex refractive index are derived as

$$n(E) = \sqrt{\frac{\varepsilon_r(E) + \sqrt{\varepsilon_r^2(E) - \varepsilon_i^2(E)}}{2}} \qquad (3.8)$$

$$k(E) = \frac{\varepsilon_i(E)}{2n(E)}. \quad (3.9)$$

In most cases, the sample under study is not homogeneous but consists of layers or is otherwise structured. In such a case, $\varepsilon(E)$ is an average over the region penetrated by the incident light, and it becomes the effective dielectric function, written as $\varepsilon_{eff}(E)$. From this effective dielectric function $\varepsilon_{eff}(E)$ and appropriate models, layer properties, such as thickness or layer dielectric functions can be derived.

Fig. 3.5 shows a schematic diagram of the concept of deduction of a dielectric function and a thickness of a film deposited on a substrate. If the dispersion of the dielectric function of the substrate $\varepsilon_{sub}(E)$ is known and also the dispersion model of the dielectric function of the film is properly selected, by fitting these dispersions to the effective dielectric function $\varepsilon_{eff}(E)$, the dielectric function $\varepsilon_f(E)$ and at the same time the thickness d can be derived as fitting parameters.

3.4.2 Measurement of Photo-Induced Refractive Index Change

Figure 3.6 shows the experimental setup for the laser beam irradiation. An argon-ion laser (NEC, GLG3300) with 514.5 nm wavelength was used as the exposure source. A shutter was placed in the incident path to control the irradiation time. In order to irradiate the sample uniformly, a beam expander with magnification of 3 was used. The beam profiles before and after the expansion are shown in Fig. 3.7. Circles and dots show the measured beam profile before and after the expansion, respectively. Solid curves are Gaussian-function fitted to the measured points by the least square method. The beam diameter was expanded from 1.3 mm to 4.0 mm through the expander. Here the diameter is defined as the point where the normalized power density is $1/e^2$. The output power of the Ar-ion laser was 175 mW, thus the power density at the sample was estimated to be 2.8 W/cm^2, using

$$I = \frac{8}{\pi\phi^2} P \qquad (3.10)$$

where I is the power density, P is the total power, and ϕ is the diameter.

The annealing was carried out in nitrogen at 170 °C for 30 min with a ramp of 50 °C/min.

We repeatedly irradiated and annealed the samples. After each step, the refractive indices were measured.

We used the spectroscopic phase modulated ellipsometer (SPME; JOBIN-YVON, UVISEL Ellipsometer) to measure the refractive index of chalcogenide glass films. The optical set-up of the SPME is presented in Fig. 3.8. The incident arm

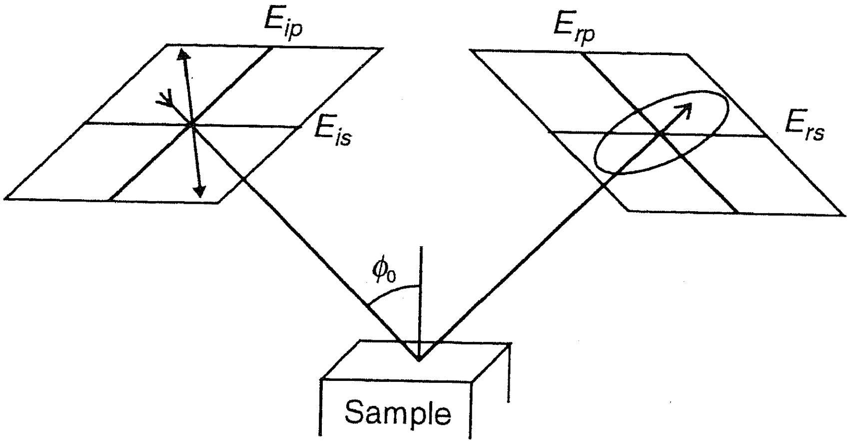

Fig. 3.4 Principle of ellipsometric measurements. Linear polarized light is incident on the sample under an angle ϕ_0 and the polarization state of the reflected light, which is in general elliptically polarized, is measured.

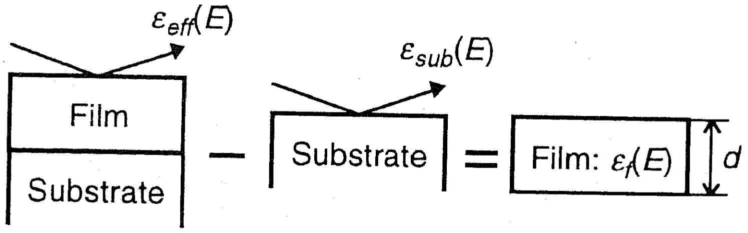

Fig. 3.5 A schematic diagram of the concept of deduction of layer properties by spectroscopic ellipsometry.

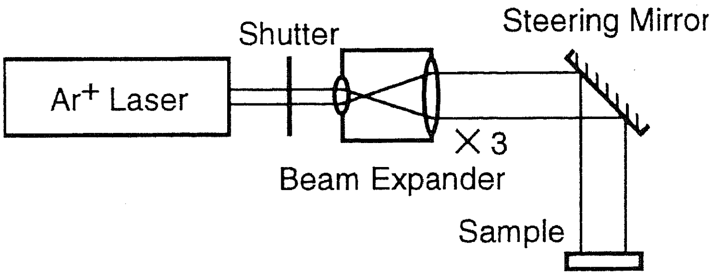

Fig. 3.6 Experimental setup for the Ar ion laser beam irradiation.

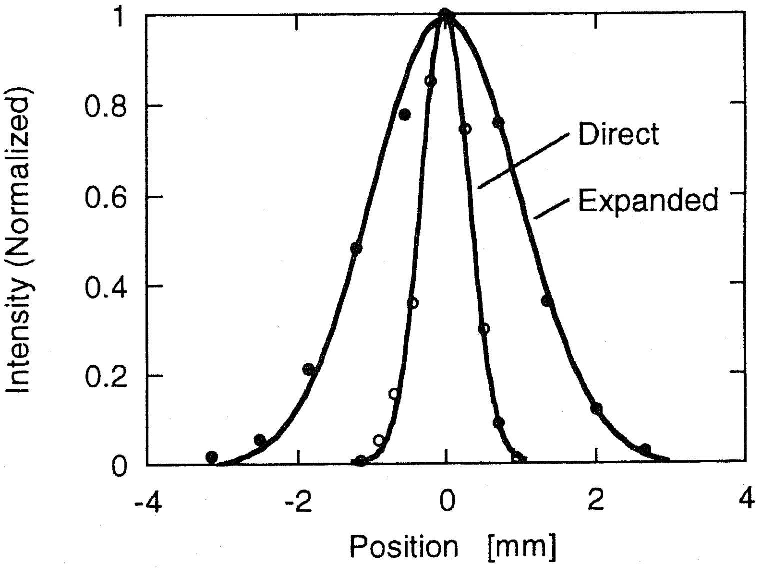

Fig. 3.7 Profiles of the direct and expanded beams of an Ar ion laser used for the irradiation.

consists of a light source, a polarizer, a photoelastic modulator where the incident polarization is modulated. After reflection on the sample, the emerging beam goes through an analyzer and a monochromator before detection.

In this configuration, the whole spectrum of the light source is incident on the sample. The light source is a xenon high pressure arc-lamp and it has a wide spectrum from ultraviolet to near infrared shown in Fig. 3.9, with a total power density at the sample of 0.03 W/cm^2. Although this power density was two orders smaller than that of the Ar-ion laser, a small amount of change in the refractive index of the chalcogenide film might be induced during the measurement. It can be avoided by inserting the low-pass-filter in front of the sample, which has the cut off at the band gap energy of the chalcogenide glass film, however, we took no account of this change in the refractive index measurement described below.

Here we illustrate the measurement procedures of the refractive index of as-deposited $As_4Se_5Ge_1$ film as an example.

Figures 3.10 and 3.11 show the measured dielectric function of the Si substrate and the as-deposited $As_4Se_5Ge_1$ film on the Si substrate. Dots and circles denote real and imaginary part of dielectric functions, respectively. They were measured from 0.75 eV to 4.5 eV at intervals of 0.05 eV. Both real and imaginary part of the dielectric function of the Si substrate gradually increases as the energy increases until 3 eV. Then slopes become steep and ei rapidly increases, which indicates the Si substrate becomes opaque. Periodic structures found in Fig. 3.11 below 2.5 eV show the interference between two reflections from the surface of the $As_4Se_5Ge_1$ film and the interface between the film and the Si substrate. This interference indicates the transparency region of the $As_4Se_5Ge_1$ film.

The dispersion relations of the chalcogenide glass film were assume to be [13],

$$k(E) = \frac{A(E - E_g)^2}{E^2 - BE + C} \qquad (3.11)$$

$$n(E) = \sqrt{\varepsilon_\infty} + \frac{B_0 E + C_0}{E^2 - BE + C} \qquad (3.12)$$

where E_g is the band gap energy, ε_∞ is the high energy dielectric constant, and,

$$B_0 = \frac{A}{Q}\left[-\frac{B^2}{2} + E_g B - E_g^2 + C \right] \qquad (3.13)$$

$$C_0 = \frac{A}{Q}\left[(E_g^2 + C)\frac{B}{2} - 2E_g C \right] \qquad (3.14)$$

$$Q = \frac{1}{2}\sqrt{4C - B^2} \qquad (3.15)$$

We fitted these dispersion relations to the measured effective dielectric function of the as-deposited $As_4Se_5Ge_1$ film on the Si substrate by using the least square method. Although it is desirable to fit dispersion relations to the whole spectrum, we restricted the fitting range to the energy lower than 3 eV, since it was hard to fit to the higher energy. This difficulty suggests that the dispersion relations we assumed do not properly represent the actual dispersion above the energy larger than 3 eV where its absorptive region. Fitting curves are shown in Fig. 3.10 as solid lines and parameters are listed in TABLE 3.4. Substituting these parameters for the dispersion relations shown above, the refractive index *n* and the extinction coefficient *k* of the as-deposited $As_4Se_5Ge_1$ film shown in Fig. 3.12 were derived. *n* and *k* are denoted by solid and broken lines, respectively.

The measured refractive index and the extinction coefficient of as-deposited, irradiated, and annealed As_2S_3 and $As_4Se_5Ge_1$ films are shown in Figs. 3.13 and 3.14, respectively. The refractive indices of as-deposited As_2S_3 and $As_4Se_5Ge_1$ films drawn in solid lines were increased towards the broken lines by the irradiation, and reached saturation after 420 sec. The change of the refractive index of As_2S_3 is about 0.1 at 1.55 μm which is twice as large as that of 0.04 in the $As_4Se_5Ge_1$ film.

After the annealing, the refractive index of As_2S_3 film was slightly increased as denoted by the dotted line, and the amount of the change was about 0.01. On the contrary, the refractive index of $As_4Se_5Ge_1$ went back to almost original position with the index change of 0.03.

The extinction coefficients of As_2S_3 and $As_4Se_5Ge_1$ films in Figs. 3.14 (a) and (b), respectively, show the band edge shifts towards the longer wavelength side (solid to broken lines) by the light irradiation. The band edges in both figures shift back towards the shorter wavelength side (broken to dotted lines) by the annealing. The band edges were determined from these figures to be approximately 0.54 μm in the As_2S_3 film, and 0.73 μm in the $As_4Se_5Ge_1$ film. The $As_4Se_5Ge_1$ film, however, has the gradual absorption tail, which is called the Urbach tail, extending towards the longer wavelength side beyond 0.73 μm. This loss must be taken into account in designing the laser structure.

Figures 3.15 (a) and (b) show the refractive index change at 1.55 μm as a function of irradiation and annealing steps. The refractive indices of as-deposited As_2S_3 and $As_4Se_5Ge_1$ films were increased by each irradiation and reached saturation. The photo-induced refractive index change of the $As_4Se_5Ge_1$ film is faster than that of the As_2S_3 film. This difference in the sensitivity to the irradiation of the Ar-ion laser having the wavelength of 514.5 nm is attributed to the difference in ex-

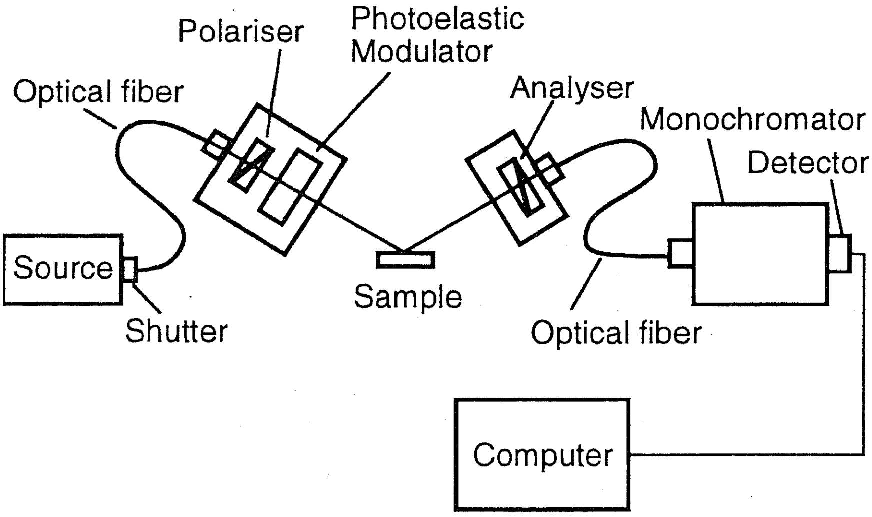

Fig. 3.8 Schematic diagram of the spectroscopic phase modulated ellipsometer.

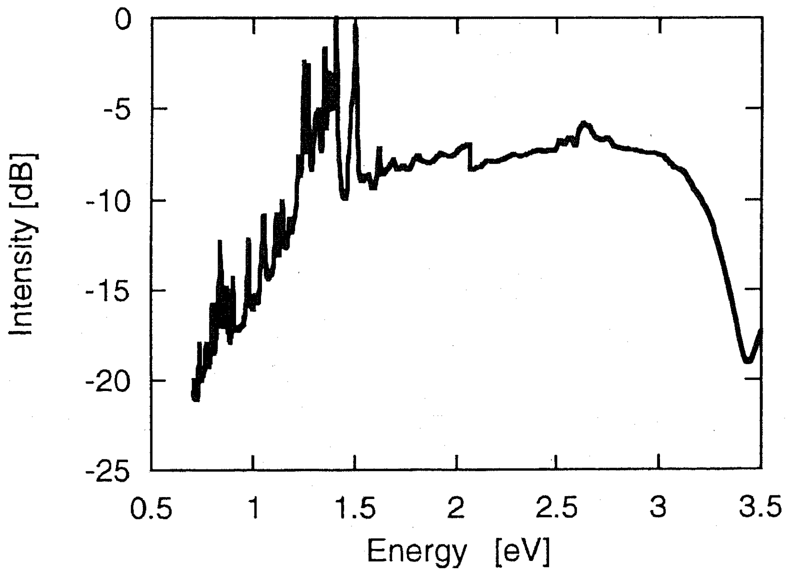

Fig.3.9 Measured spectrum of the Xe lamp used in the spectroscopic ellipsometer.

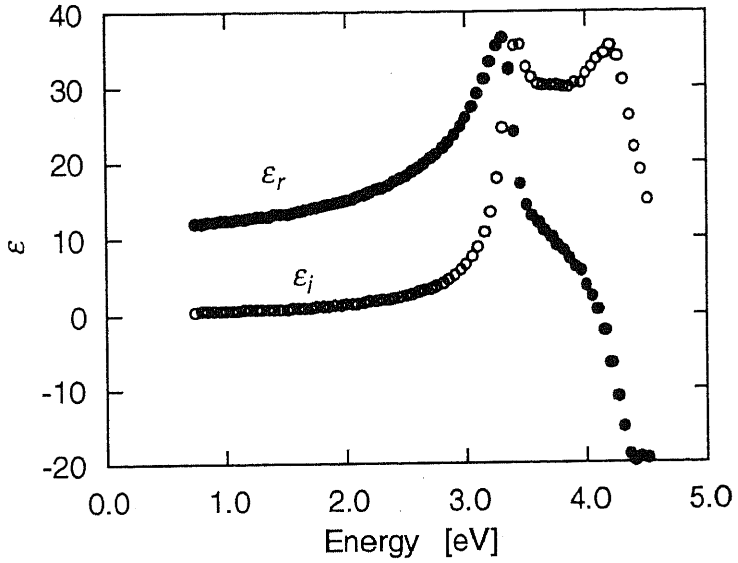

Fig. 3.10 Measured dispersion of dielectric function of the Si substrate.

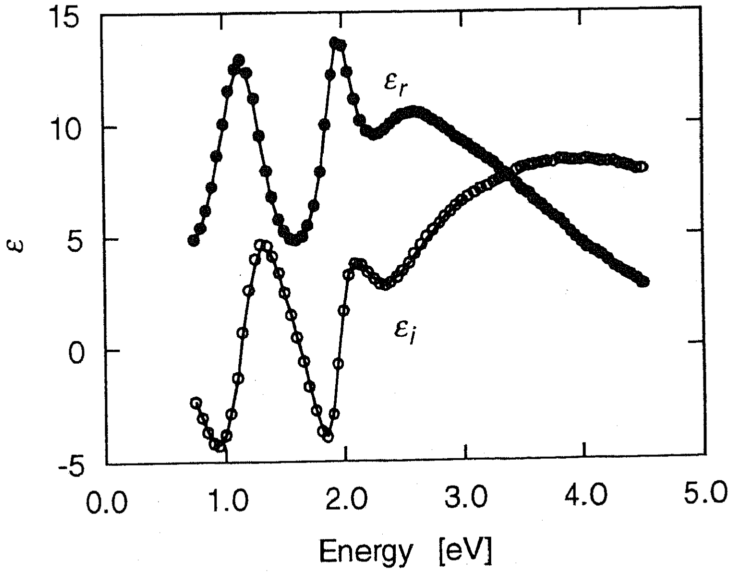

Fig. 3.11 Measured dispersion of dielectric function of the as-deposited $As_4Se_5Ge_1$ film on the Si substrate. Solid lines show the fitted curves.

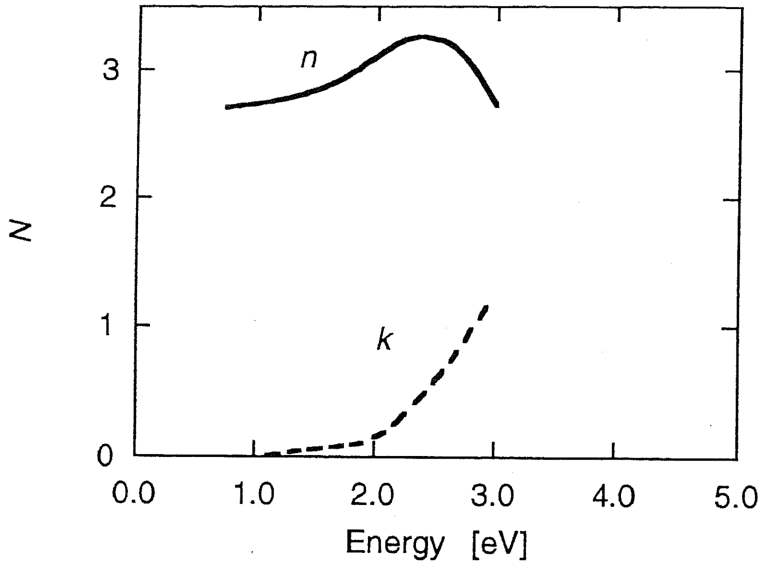

Fig. 3.12 Complex refractive index of the as-deposited $As_4Se_5Ge_1$ film.

TABLE 3.4 Fitting parameters for the as-deposited $As_4Se_5Ge_1$ film.

Parameter	Value [Unit]
Thickness d	207 [nm]
ε_∞	7.019
A	0.325
B	4.559
C	5.572
E_g	1.729 [eV]

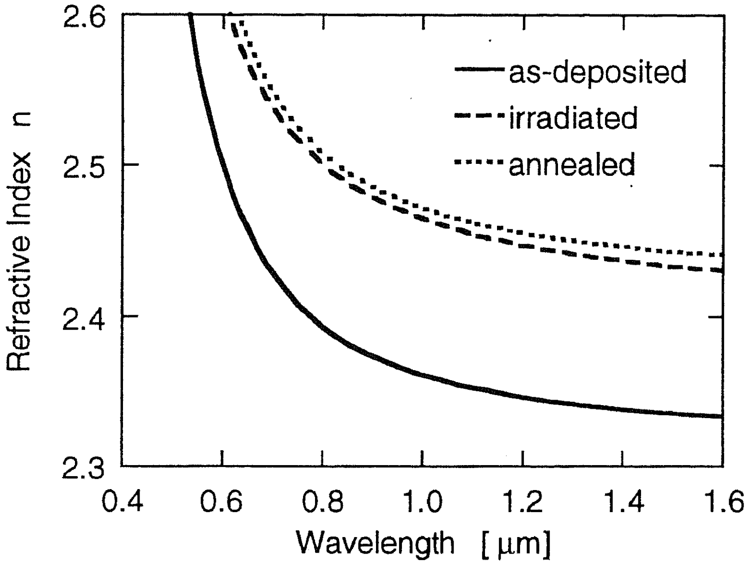

(a) As_2S_3

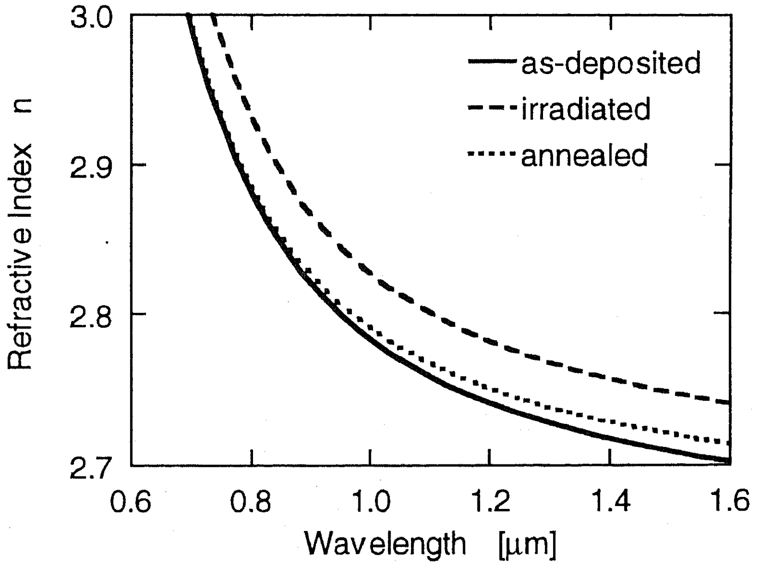

(b) $As_4Se_5Ge_1$

Fig. 3.13 Wavelength dispersion of the refractive index of as-deposited, irradiated, and annealed (a) As_2S_3 and (b) $As_4Se_5Ge_1$ films.

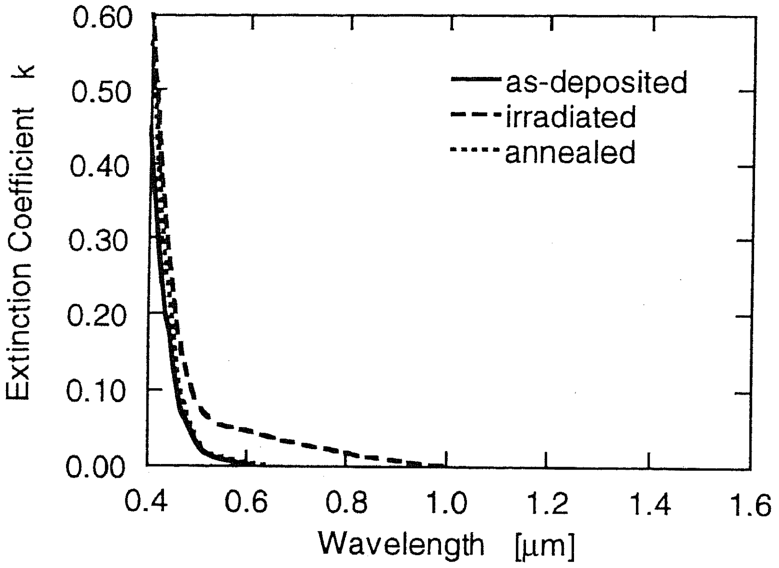

(a) As_2S_3

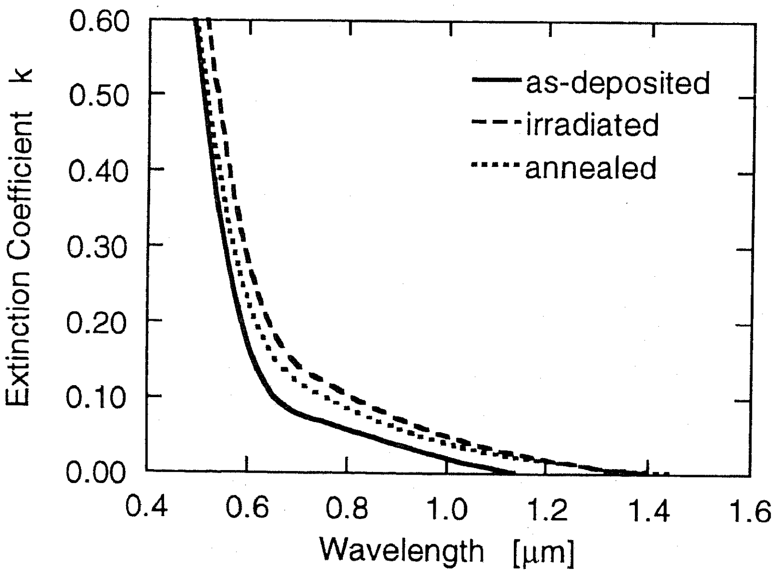

(b) $As_4Se_5Ge_1$

Fig. 3.14 Wavelength dispersion of the extinction coefficient of as-deposited, irradiated, and annealed (a) As_2S_3 and (b) $As_4Se_5Ge_1$ films.

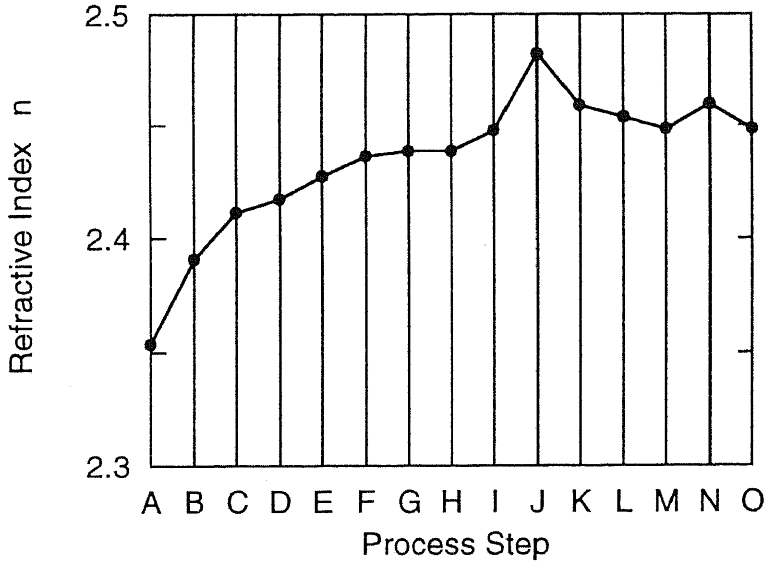

(a) As_2S_3

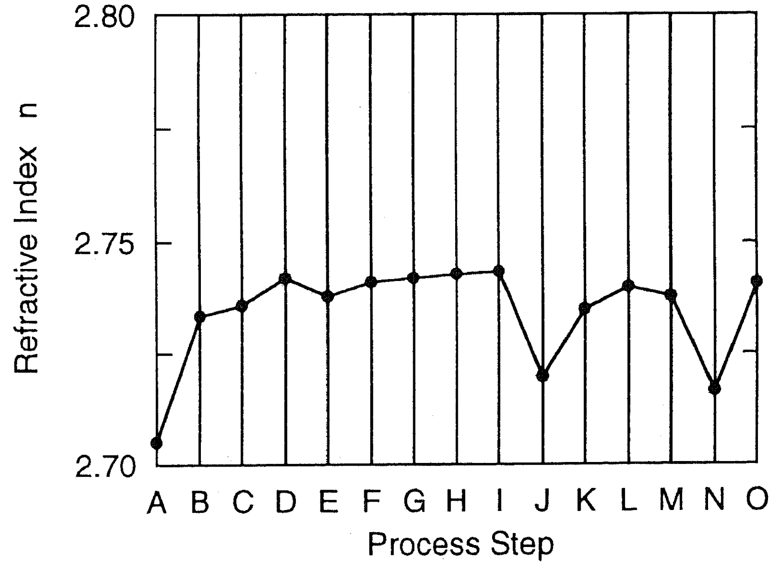

(b) $As_4Se_5Ge_1$

Fig. 3.15 Refractive index change of (a) As_2S_3 and (b) $As_4Se_5Ge_1$ films at 1.55 μm as a function of process steps.
A: as-deposited, B: irradiated for 30 sec, C: 30 sec, D: 30 sec, E: 30 sec, F: 30 sec, G: 30 sec, H: 30 sec, I: 180 sec, J: annealed, K: 60 sec, L: 180 sec, M: 480 sec, N: annealed, O: 720 sec

tinction coefficients which can be inferred from Figs 3.14, where the $As_4Se_5Ge_1$ film has the extinction coefficient two orders larger than that of the As_2S_3 film at 514.5 nm. It is understood from this figure, the refractive index of the chalcogenide glass can be adjusted by controlling the irradiation time. We have carried out annealing steps for two times to confirm that reversible change between the irradiated and the annealed states. The steps I, M and O correspond to the irradiated states and the steps J and N correspond to the annealed states. It is clearly seen that both states were repeatedly realized.

The change of refractive index between as-deposited and irradiated states, and between irradiated and annealed states at 1.55 μm are summarized in TABLE 3.5.

3.5 Process Tolerance of Chalcogenide Glass Films

The sequence of fabrication process of laser diodes is comprised of several steps of epitaxial growth, photolithography, etching, passivation, and metallization. All materials grown or deposited must have a tolerance to the following process. In this section, we describe tolerance of chalcogenide glass films to several processes.

We first investigated the process tolerance to the surface cleaning which is generally used for oil take-off. Figures 3.16 (a) and (b) show the optical micrograph of the surface of As_2S_3 before and after the ultrasonic cleaning in a trichloro ethylene, an acetone, and an alcohol, for 5 min each. The surface damage found in (b) was caused by the impact of bubbles induced by the ultrasonic. On the other hand, no damage was found on the surface of the $As_4Se_5Ge_1$ film. The surface damage indicates that the As_2S_3 film is particularly soft and easy to be scratched. Although the damage can be avoided by cleaning in boiled solvents instead of applying the ultrasonic, the fabrication process after the chalcogenide glass film deposition needs special care.

Next, we have investigated the chemical tolerance and found that both As_2S_3 and $As_4Se_5Ge_1$ had tolerance to the acid such as hydrochloric and hydrofluoric acids but they were easily eroded by developing solution of a positive photoresist which is relatively strong alkali.

Furthermore, we have investigated the tolerance to the heat treatment and found that the sulfur in As_2S_3 was easily desorbed by the annealing above 200 °C, thus the protection layer should be deposited on the chalcogenide glass film to avoid the desorption. In $As_4Se_5Ge_1$, no desorption of the selenium was found at 200 °C, but the crystallization arose after annealing the sample for 2 min at 350 °C. Figure 3.17 shows the optical micrograph of the surface of the $As_4Se_5Ge_1$ film covered with

TABLE 3.5 Photo-induced refractive index change in As_2S_3 and $As_4Se_5Ge_1$ films at wavelength of 1.55 μm.

Compound	as-deposited ↓ irradiated	annealed ↓ irradiated
As_2S_3	0.10 (4.2 %)	–0.01 (–0.4 %)
$As_4Se_5Ge_1$	0.04 (1.5 %)	0.03 (1.1 %)

(a) before (b) after

Fig. 3.16 Surface damage of the As_2S_3 film after ultrasonic cleaning.

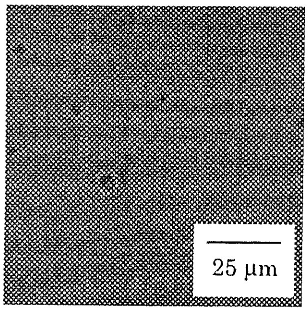

Fig. 3.17 Partial crystallization of the $As_4Se_5Ge_1$ film covered with SiO_2 after heat treatment at 350 °C for 2 min.

SiO_2 protection layer deposited by the plasma chemical vapor deposition. A geometric pattern found in the figure clearly indicates the partial crystallization of the $As_4Se_5Ge_1$. We have verified that this crystallization was not induced during the deposition of SiO_2 protection layer. The substrate temperature was adjusted to be relatively low around 190 °C during the deposition. Other conditions were summarized as follows. The background and the process pressures were 4×10^{-5} Torr and 0.3 Torr. The incident power was 50 W. The source gases were silane and nitrous oxide and their flow were 20 and 135 sccm, respectively.

From these results, we must take a precaution for the fabrication process after the chalcogenide glass film deposition. And also we have reached the conclusion that the As_2S_3 is not suitable for the laser waveguide material, even though this glass composition has larger refractive index change between as-deposited and irradiated states and hence larger wavelength adjustment is expected.

3.6 Proposal of Wavelength Trimming by Photo-Induced Refractive Index Change

In this section, we propose a wavelength trimming by making use of the photo-induced refractive index change. After summarizing keys in realization, we propose a variety of concepts of device structures incorporated with the chalcogenide glass. From various possibilities, we have selected a mesa waveguide structure where the chalcogenide glass film is loaded at the side of the active layer. The design of the waveguide based on this structure is also shown.

A concept of the wavelength trimming by making use of the photo-induced refractive index change is illustrated in Fig. 3.18. The chalcogenide glass is placed in the close vicinity of the active layer of the laser waveguide. Provided that this film is irradiated with the external light source having the energy larger than the band gap of the chalcogenide glass or heated around the glass transition temperature, the effective refractive index of the waveguide and hence the oscillation wavelength can be adjusted even after the device fabrication.

Here, we formulate the oscillation wavelength shift through the refractive index change in a specific layer which compose a laser waveguide. As described in Chapter 2, the oscillation wavelength of DFB lasers is given by the Bragg relation,

$$\lambda = 2n_{eff}\Lambda, \qquad (3.16)$$

where λ is the oscillation wavelength, n_{eff} is the effective refractive index of the laser waveguide, and Λ is the period of diffraction grating. Therefore, the wavelength shift is readily derived from equation (3.16),

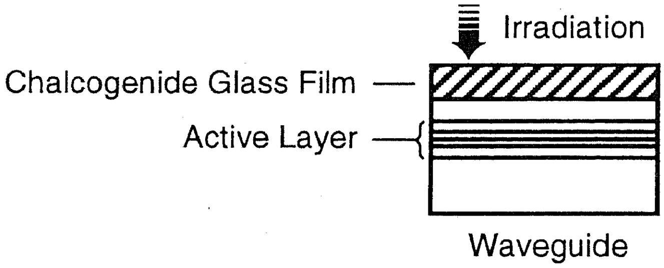

Fig. 3.18 A concept of the wavelength trimming by using the chalcogenide glass having the photo-induced refractive index change as a laser waveguide.

$$\Delta\lambda = \frac{\Delta n_{eff}}{n_g}\lambda \qquad (3.17)$$

where $\Delta\lambda$ is the wavelength shift, Δn_{eff} is the effective refractive change, and n_g is the group refractive index that is an effective refractive index including a wavelength dispersion. The effective refractive index change can be expressed as

$$\Delta n_{eff} = \Gamma_x \Delta n_x \qquad (3.18)$$

where Γ_x is the optical confinement factor in the specific layer having the refractive index change of Δn_x. Substituting equation (3.18) for equation (3.17), we finally obtain the wavelength shift through the refractive index change,

$$\Delta\lambda = \frac{\Gamma_x \Delta n_x}{n_g}\lambda. \qquad (3.19)$$

From this equation, it is understood that not only large refractive index change but also a large optical confinement are required to accomplish substantial wavelength adjustment.

The requirements for the device structure to make the wavelength trimming possible are that the chalcogenide glass layer must be loaded in the close vicinity of the laser active layer to achieve the large optical confinement since the refractive index difference between the chalcogenide glass (~2.8) and the active layer material (~3.3) is large, and that it must be seen from the outside for the external light irradiation. Moreover, in the laser structure, it must be taken account of that the current path from the contact to the active layer and the confinement of not only the optical field, but also carriers. The sequence of the device fabrication is also important, since the tolerance of the chalcogenide glass to the process is inadequate.

Figures 3.19 show examples of the structures which meet above requirements. Fig. 3.19 (a) shows the transverse junction stripe structure where the chalcogenide glass is loaded on the waveguide. All layers having the conduction type of n are grown on the semi-insulating substrate. The pn-junction is formed by the Zn-diffusion and thus the active layer is located at the diffusion front. The current is laterally injected to the active layer. This structure is a direct implementation of the concept of wavelength trimming by utilizing the photo-induced refractive index change as shown in Fig. 3.18. In practice, the development of this structure needs an uncommon process such as the diffusion, and the control of the lateral optical mode, which is indispensable for the single-mode oscillation, might be the problem.

Fig. 3.19 (b) is the ridge waveguide structure where the chalcogenide glass is periodically buried along the waveguide with the grating period. In other words, the grating consists of the chalcogenide glass. In this structure, the current can be injected from the top of the waveguide and at the same time, the lateral mode can be controlled. The obstacle to the realization would be the formation of the deep grating into the waveguide.

Fig. 3.19 (c) is the conventional ridge waveguide where the chalcogenide glass is placed beside the waveguide. Although this structure is simple and easily fabricated, it is hard to realize the large optical confinement in the chalcogenide glass.

Fig. 3.19 (d) is the mesa waveguide structure where the chalcogenide glass is placed at the side of the active layer.

We have selected this mesa waveguide structure from various possibilities as shown above. Using this structure with narrow stripe, the large optical confinement in the chalcogenide glass can be attainable. The drawbacks may arise from the etched active layer, such as the surface recombination of carries, the excitation of higher order lateral modes due to the large refractive index difference, and the reliability. The first problem of the surface recombination of carriers is, however, insignificant in InGaAsP quaternary systems, and the second problem of higher order lateral modes can be controlled by using the sufficiently narrow active layer width. The third and that would be the biggest problem of the reliability can be avoided by the epitaxial growth of the thin InP layer on the surface of the active layer or disordering the part of the active layer near the surface to form a lateral heterostructure and constrict carriers.

Next, we carried out the design of the waveguide. Figure 3.20 shows the optical confinement factor in the $As_4Se_5Ge_1$ layer as a function of the active layer width. The optical confinement in the glass was estimated by using a simple 1 dimensional 3 layer model shown as an inset [14]; the active layer was assumed to be sandwiched laterally between the Al_2O_3 passivation layer and the $As_4Se_5Ge_1$ layer with infinite thickness, and the refractive indices of active layer, Al_2O_3, and $As_4Se_5Ge_1$ were assumed to be 3.3, 1.7, and 2.8, respectively. We also assumed that the oscillation wavelength of the laser was 1.55 μm. Substituting this optical confinement factor, together with the refractive index change of chalcogenide glass films listed in TABLE 3.4, for equation (3.19), the wavelength shift can be estimated. In the case where the mesa width is 1 μm, the wavelength shift of 0.1 nm is attainable where the optical confinement factor in the chalcogenide is 1 %, the refractive index change of the $As_4Se_5Ge_1$ is 0.03, and the group refractive index is assumed to be 3.

3.7 Fabrication Procedures

Based on the above consideration, we have fabricated the mesa waveguide DFB laser. Figure 3.21 shows the cross-section of the index-coupled DFB laser where the

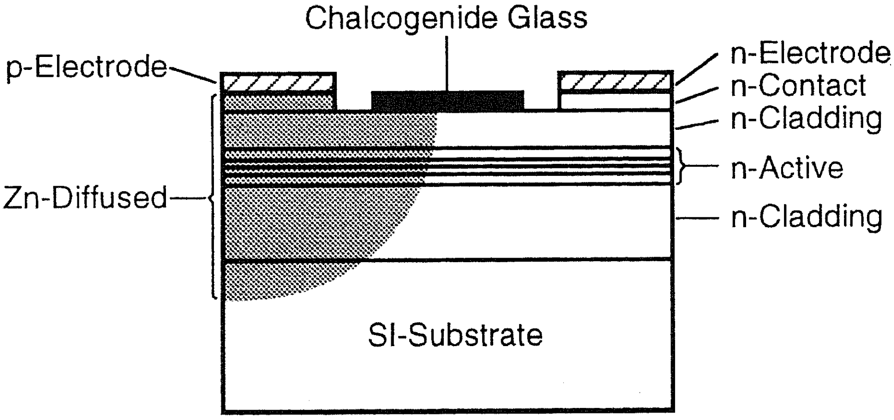

(a) Transverse junction stripe structure

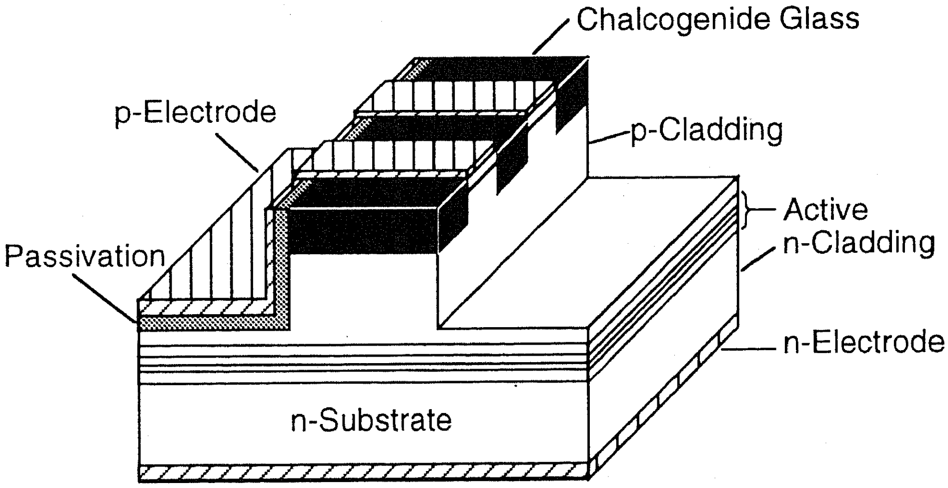

(b) Ridge waveguide structure with chalcogenide glass grating

Fig. 3.19 Various concepts of structures for the wavelength trimming by the photo-induced refractive index change. (Continued on the following page.)

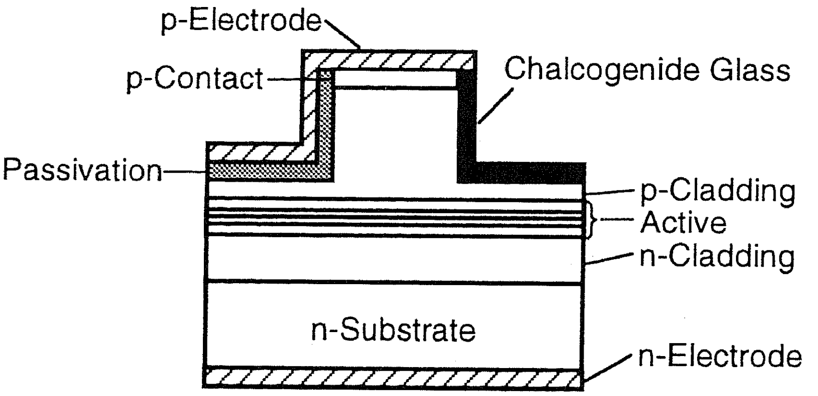

(c) Conventional ridge waveguide structure

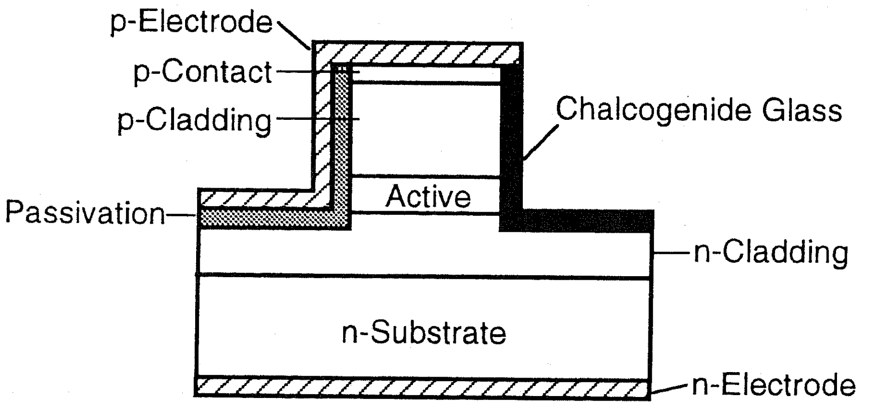

(d) Buried-hetero structure

Fig. 3.19 Various concepts of structures for the wavelength trimming by the photo-induced refractive index change.

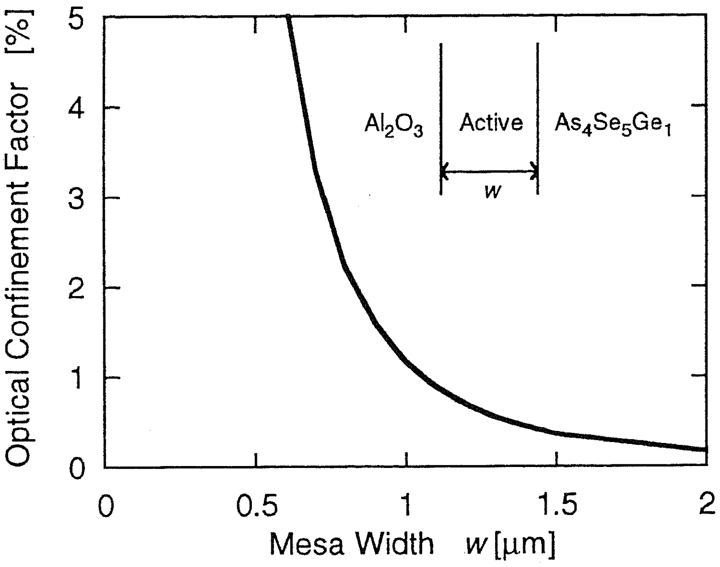

Fig. 3.20 Optical confinement factor in chalcogenide glass layer as a function of the mesa width. An inset shows the model for the calculation.

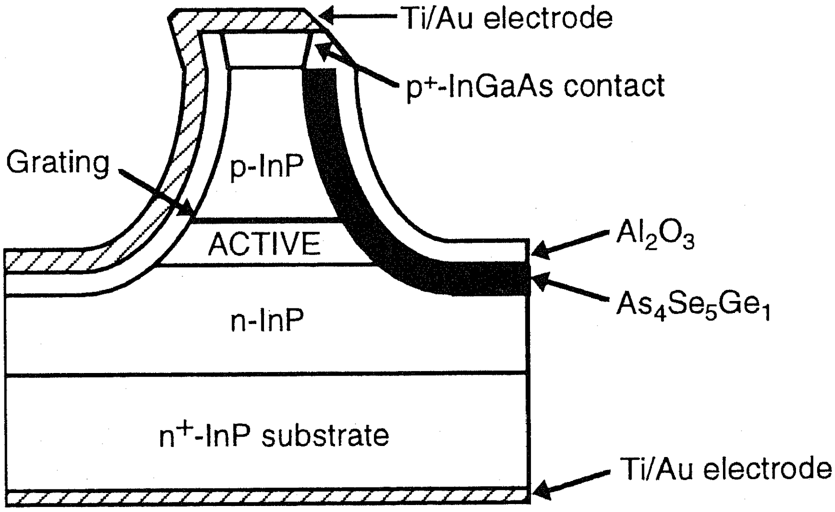

Fig. 3.21 Schematic lateral cross-section of the 1.55 μm MQW DFB laser incorporating $As_4Se_5Ge_1$ glass for wavelength trimming.

$As_4Se_5Ge_1$ film is placed alongside the active layer. In order to achieve large optical confinement in the glass, the width of the laser mesa was made sufficiently narrow (less than 1 μm).

The device fabrication sequence is schematically shown in Figs. 3.22. The epitaxial layers were grown by a horizontal-reactor low-pressure metal-organic vapor-phase epitaxy (MOVPE; AIXTRON, AIX200/4) with trimethylgallium and trimethylindium as group III precursors. Group V materials were also supplied in the form of organic metals, namely, tertiarybutylarsine and tertiarybutylphosphine. Diethylzinc was used for p-type doping. In our MOVPE system, diluted hydrogen sulfide for n-type doping is the only gas source equipped, and therefore it is by far the safer than most other systems using several raw (not-diluted) hydride gas sources. The growth pressure was 100 mbar, and the temperature was 610 °C with the exception of the period of the growth of the InGaAs contact layer where the temperature was lowered to be 550 °C to increase the doping level of zinc.

In the first step growth, an n-InP (100 nm, 5×10^{17} cm^{-3}) buffer layer, and an active region consisting of five compressively-strained 1.55 μm InGaAsP quaternary quantum wells with the separate confinement heterostructure (SCH) were grown on a (100)-oriented n^+-InP (2×10^{18} cm^{-3}) substrate (Fig. 3.22 (a)). The composition of wells and barriers were $In_{0.728}Ga_{0.272}As_{0.691}P_{0.309}$ and $In_{0.751}Ga_{0.249}As_{0.539}P_{0.461}$, respectively. The strain of +0.68 % was introduced to the well, and the thickness of wells and barriers was 10 nm. The SCH had a thickness of 120 nm. The active region was undoped. A first order uniform diffraction grating with a period of 240 nm was fabricated on the SCH by the holographic exposure method and chemical etching (Fig. 3.22 (b)). The solution used was saturated bromine water (SBW) : HBr : H_2O (1 : 10 : 40, 20 °C). In the second step growth, p-InP (700 nm, 5×10^{17} cm^{-3}) cladding, and p^+-InGaAs (200 nm, 5×10^{19} cm^{-3}) contact layers were grown on the grating (Fig. 3.22 (c)). The scanning electron micrograph of the longitudinal cross-section of the device before and after the regrowth are shown in Figs. 3.23 (a) and (b), respectively. The grating shape was trapezoidal with a height of approximately 50 nm. The grating shape was well preserved after the regrowth which might be attributed to relatively low growth temperature due to the use of tertiarybutylphosphine as a precursor of phosphorus whose decomposition rate is much higher than that of the conventional phosphine.

After the regrowth, the waveguide was delineated. In order to load the chalcogenide glass alongside the active layer, the waveguide mesa was formed by wet etching. The solution used were H_2SO_4 : H_2O_2 : H_2O (1 : 1 : 5, 5 °C) for the InGaAs contact layer, HCl (20 %, room temperature) for the InP cladding layer, and SBW : HBr : H_2O (1 : 10 : 40, 20 °C) for the active region (Fig. 3.22 (d)).

(a) 1st growth

(b) grating formation

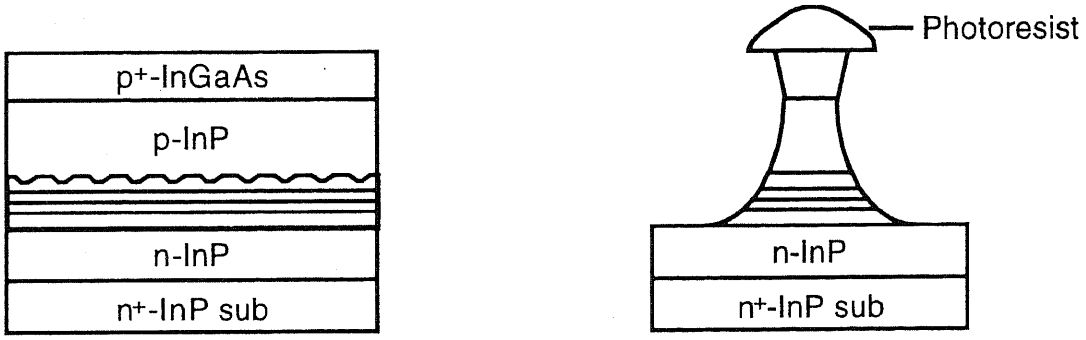

(c) 2nd growth

(d) mesa formation

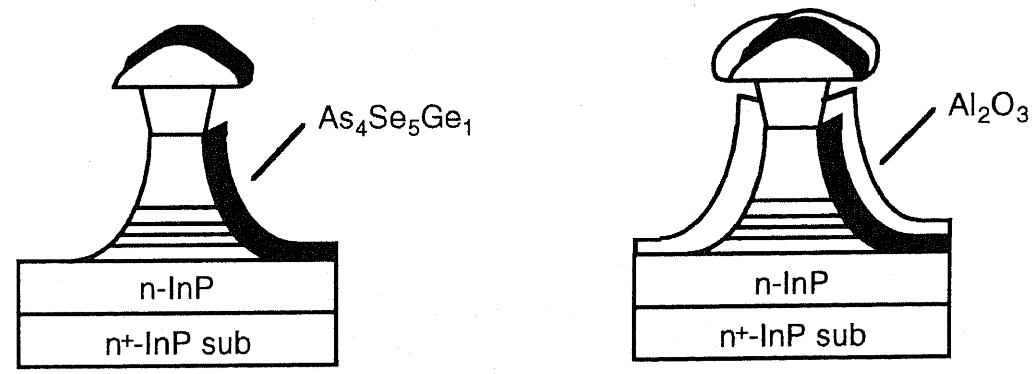

(e) $As_4Se_5Ge_1$ deposition

(f) Al_2O_3 deposition

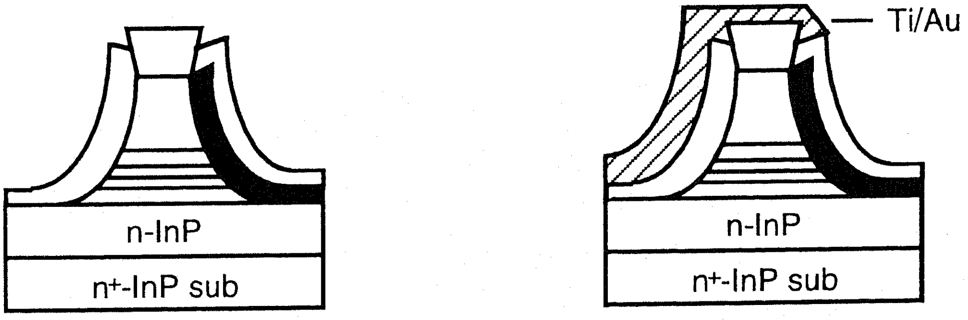

(g) lift-off

(h) Ti/Au evaporation

Fig. 3.22 The fabrication process sequence.

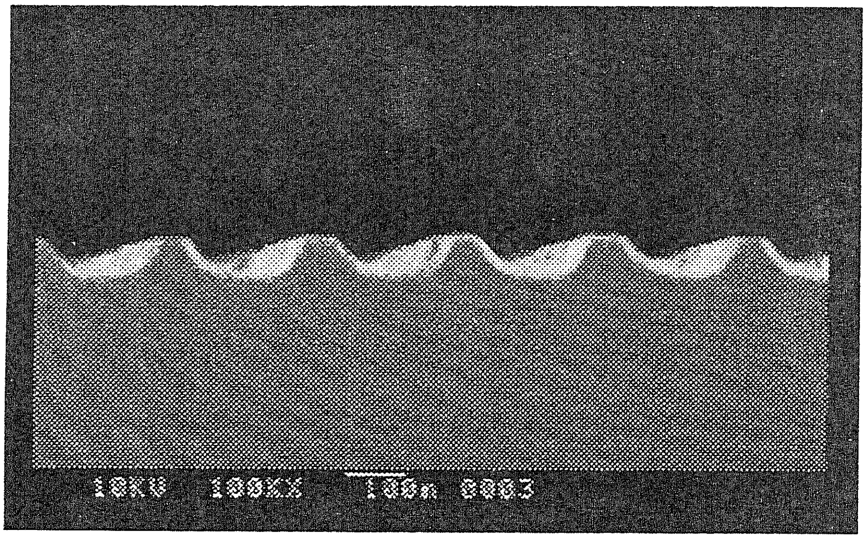

(a) before

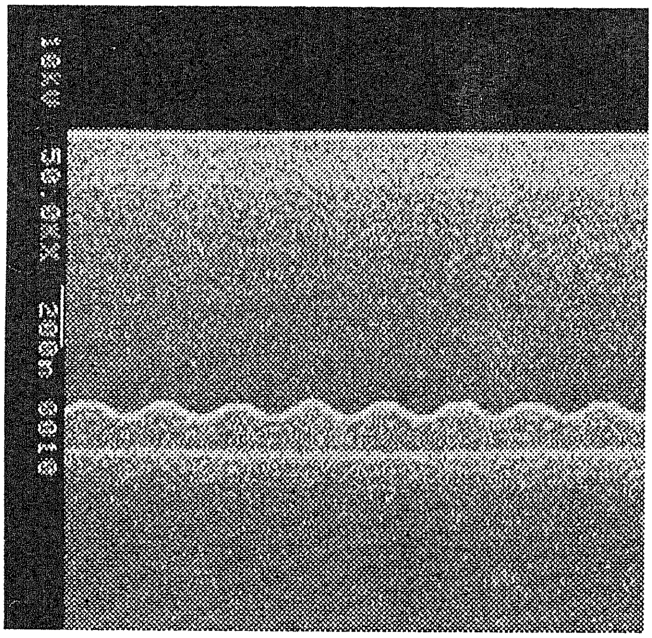

(b) after

Fig. 3.23 Scanning electron micrograph of longitudinal cross sections of the structure (a) before and (b) after the regrowth on the diffraction grating.

As described in the previous section, the robustness of the chalcogenide glass against processing is insufficient. Because of this, etching of the glass and heat treatment after deposition should be avoided. To meet this requirement, a fully self-aligned processing technique making use of "lift-off" [15], and the ohmic contact formation without the alloying heat treatment, were developed. After the mesa etching, the photoresist mask was not removed but kept on the top of the mesa as a lift-off mask. Next, the $As_4Se_5Ge_1$ glass layer with the thickness of 200 nm was deposited while holding the sample in a thermal evaporator at 45 ° off (Fig. 3.22 (e)). The deposition condition was the same as in Section 3.3. Then, the sample was placed in an electron-beam evaporator and the 200 nm thick Al_2O_3 passivation layer was deposited on both sides of the mesa (Fig. 3.22 (f)). The deposition was adjusted to be relatively high around 20 nm/sec to avoid hardening the photoresist by the radiant heat from the source since the melting temperature of Al_2O_3 is extremely high. When once the photoresist is hardened, it is quite difficult to remove. This is also beneficial to avoid the desorption or the crystallization of the chalcogenide glass film.

The $As_4Se_5Ge_1$ and Al_2O_3 on top of the mesa as well as the photoresist mask itself were removed in the next lift-off step by acetone (Fig. 3.22 (g)). It must avoid to use solvents called a stripper or a remover for removing positive-photoresists. Some of them show strong alkaline when it reacts with water during the rinse and erodes chalcogenide glasses. Both a low temperature (90 °C for 10 min) post-baking of the photoresist and the high deposition rate of Al_2O_3 facilitated the easy lift-off by acetone.

The window for the external light irradiation was formed by the angled evaporation of Ti/Au as a p-type top electrode towards the other side the $As_4Se_5Ge_1$ (Fig. 3.22 (h)). The thickness of Ti and Au were 30 and 120 nm, respectively. Then, the sample was thinned down to about 100 μm by lapping. Finally, Ti/Au was deposited on the back side of the substrate as an n-type electrode by the same amount as the top one. Owing to the high doping level of the top contact layer and the lapped rough surface of the back, the ohmic contact was achieved without the alloying heat treatment.

Figures 3.24 (a) and (b) shows the scanning electron micrograph of the cross section and the bird's eye view of the device, respectively. The width of the laser mesa was made sufficiently narrow to be 0.5 μm. The window region was formed at the right side of the mesa with the width of about 1 μm.

The completed wafer was cleaved into 300 μm long devices, and their facets were left uncoated. Then the discrete devices were bonded junction-up on chip carriers with tin solder.

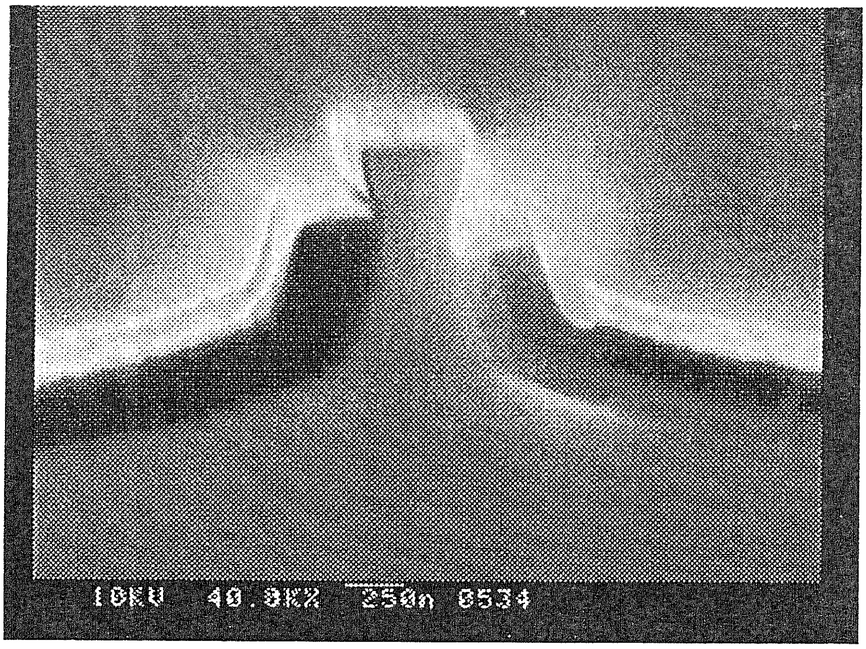

(a) cross-section

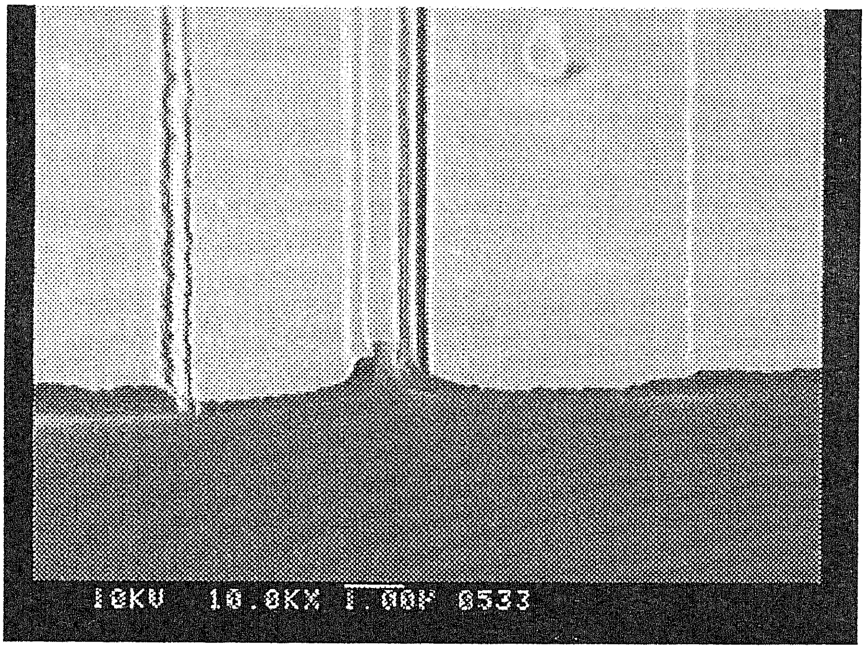

(b) bird's-eye view

Fig. 3.23 Scanning electron micrograph of (a) the cross-section and (b) the bird's-eye view of the structure.

As mentioned in Section 3.5, the partial crystallization of the $As_4Se_5Ge_1$ might be induced by the die-bonding where the maximum temperature was around 350 °C. The solder with low melting temperature such as indium or the silver epoxy is preferable. At this stage, we found that the adhesion of the chalcogenide glass film was insufficient for the wire-bonding process where the tension was applied to the device while wiring. Therefore, the first contact was made on the lead metal, and then the second one was done on the device to avoid the tension.

3.8 Wavelength Trimming Experiment

Next we have carried out the wavelength trimming experiment. Figure 3.25 shows the setup for the wavelength trimming experiment. The chip carrier was placed on a thermo-electric cooler to keep the temperature constant at 20 °C with a stability of 0.01 °C. In order to introduce the laser beam into the chalcogenide glass layer through the window formed at the side of the active layer, the sample was tilted with an angle of 45 °. The threshold current of the measured sample was 7 mA under continuous-wave operation at room temperature. We have repetitively irradiated the sample, operated above the threshold current at 10 mA, with a 632.8 nm helium-neon laser (NEC, GLG5600) beam having the power density of 1.3 W/cm^2 and the diameter of 1.1 mm, and observed the oscillation spectra. The stability of the drive current was 1 μA. A shutter was placed in the incident path to control the irradiation time.

The beam alignment was performed by monitoring absorption photo-current from the laser chip and maximizing it. During the beam alignment, the variable neutral density filter was inserted into the beam path to reduce the intensity of the beam to avoid the unintentional wavelength shift.

Although the laser beam had a Gaussian profile and its maximum was located approximately at the center of the cavity, since its diameter was large in comparison with the cavity length of the device which was 300 μm, thus it was irradiated with almost same power density along the waveguide, we did not use the beam expander.

The output light from the chip was introduced into an optical spectrum analyzer (ANDO, AQ-6315A) with 0.05 nm resolution via a single-mode fiber with the core-diameter of 10 μm. The laser sensing head (SANTEC, LSH-155) consisted of the collimation optics included the two-stage optical isolators with a return loss of 60 dB.

Wide span spectra from the laser chip as-fabricated below and above threshold currents are shown in Figs. 3.26 (a) and (b). The gain peak and the DFB mode

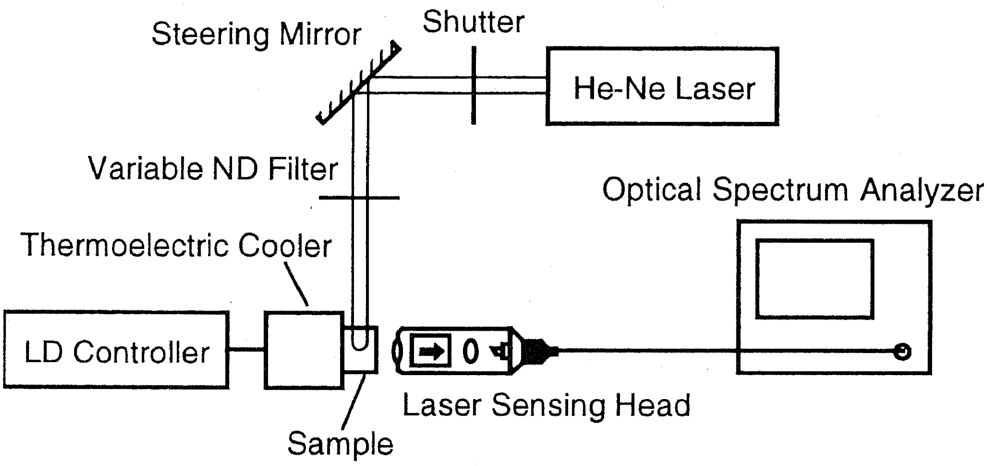

Fig. 3.25 Schematic diagram of the setup for the wavelength trimming by the photo-induced refractive index change.

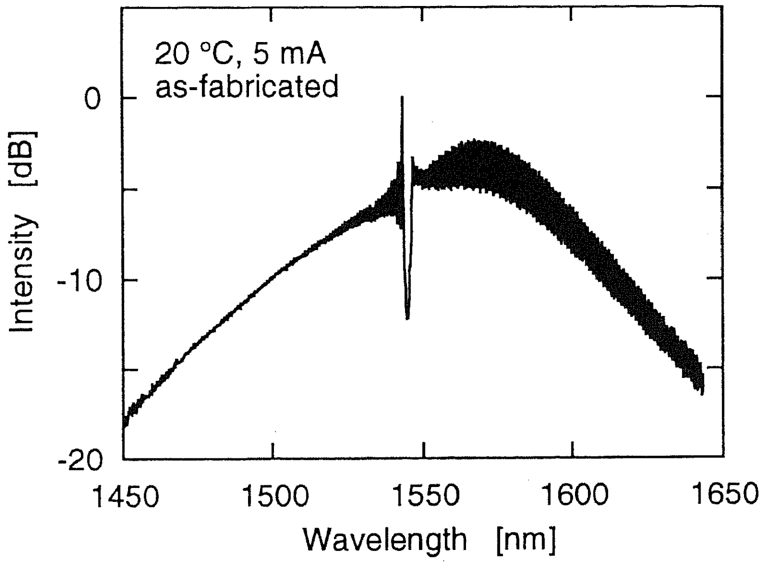

(a) below threshold

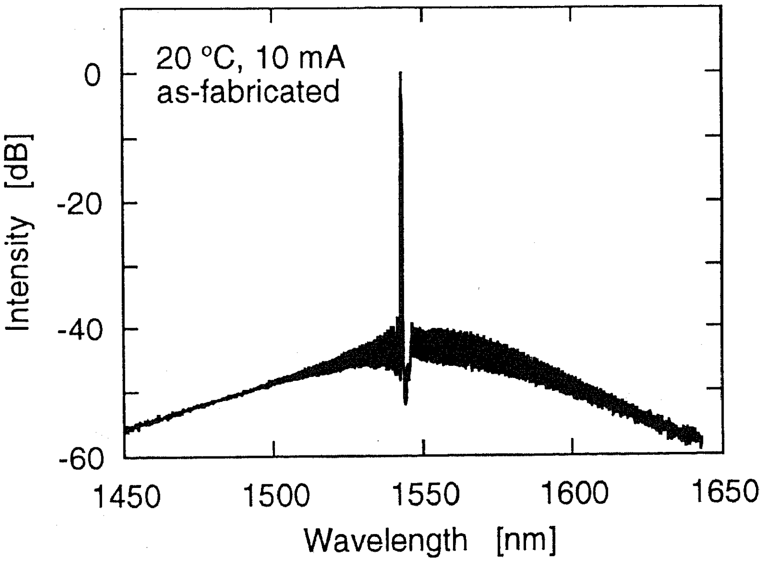

(b) above threshold

Fig. 3.26 Wide span spectra before the irradiation at currents below (a) and above (b) threshold.

are found around 1570 and 1540 nm, respectively. The dip next to the lasing mode corresponds to the stop band. No higher order lateral modes are found. The side mode suppression ratio is 40 dB at 10 mA.

Figure 3.27 shows the oscillation wavelength shift as a function of the He-Ne laser irradiation time. At each irradiation step, the oscillation wavelength shifted towards the longer wavelength side as the refractive index of the chalcogenide glass increased. The wavelength was steady and stable after stopping each irradiation. The shift reached saturation after 570 sec of irradiation where the total amount of wavelength shift was 0.14 nm. The irradiation time dependence of the peak wavelength shift obeys the exponential law as represented by the solid line, which is fitted to the measured data, using the relation,

$$\lambda = \lambda_0 \left\{ 1 + \frac{\lambda_\infty - \lambda_0}{\lambda_0} \left[1 - \exp\left(-\frac{t}{\tau} \right) \right] \right\} \qquad (3.20)$$

where t is time, τ is the time constant, and λ_0 and λ_∞ are initial and saturated wavelengths, respectively. The time constant τ in this case was 63 sec. As understood from this figure, the oscillation wavelength of the DFB laser is adjustable through the irradiation time.

The output power as a function of the driving current is depicted in Fig. 3.28. The threshold currents before and after the irradiation are 7 mA and 7.5 mA, respectively. This slight increase is attributed to the increase of the absorption in the $As_4Se_5Ge_1$ glass layer, which can be inferred from Fig. 3.14 (b).

The oscillation spectra below and above the threshold currents are shown in Figs. 3.29 (a) and (b). Below threshold, the amount of wavelength shift is 0.24 nm which is larger than the value above threshold. This difference can be explained by taking into account the small increase in the threshold current in Fig. 3.28. A fraction of the refractive index increase in the $As_4Se_5Ge_1$ glass layer was canceled by refractive index decrease in the active layer. This was caused by increase of the carrier density in the active layer due to the small increase of the threshold current. In other words, 0.24 nm shift below the threshold is the direct consequence of the index change in $As_4Se_5Ge_1$ by the light irradiation. This value agrees well with our theoretical prediction of 0.3 nm calculated from equation (3.19), where optical confinement of 2 %, refractive index change of 0.03, group refractive index of 3, and the wavelength of 1.55 μm were assumed.

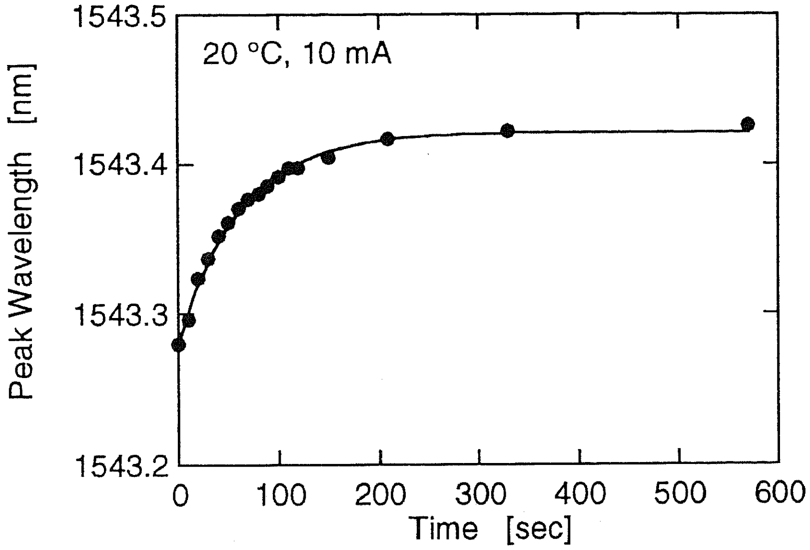

Fig. 3.27 Oscillation wavelength shift as a function of the irradiation time.

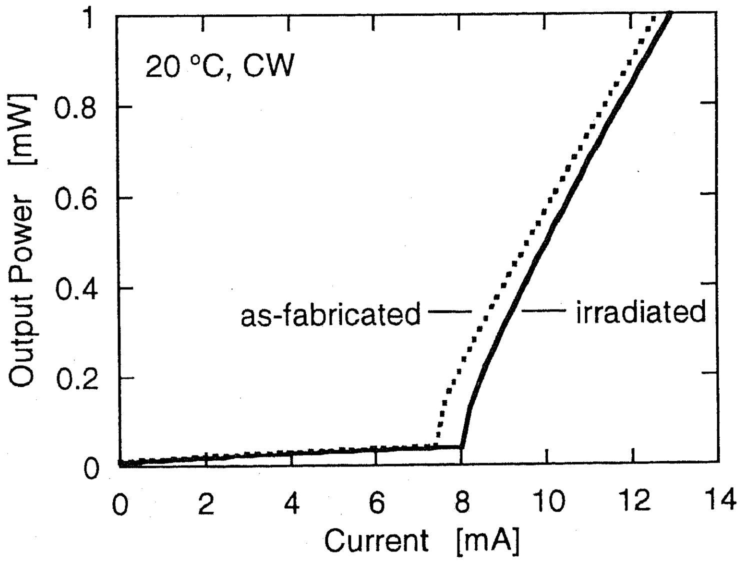

Fig. 3.28 CW LI-characteristics at 20 °C.

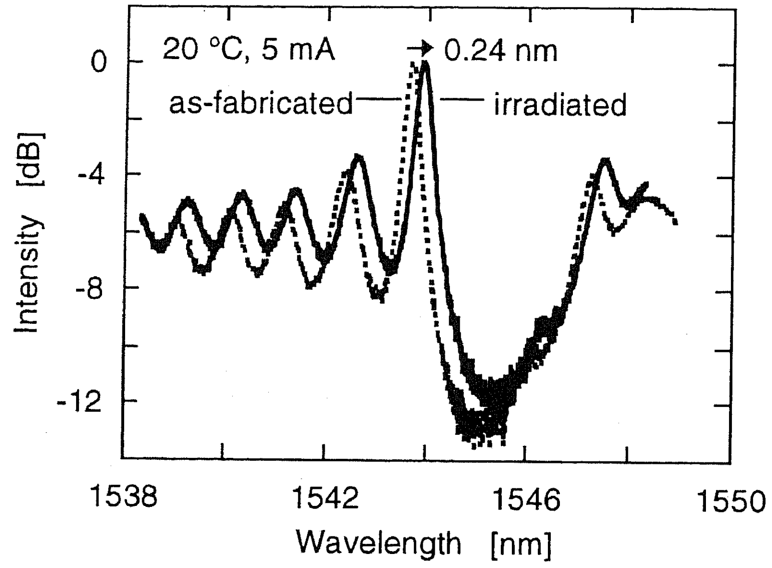

(a) below threshold

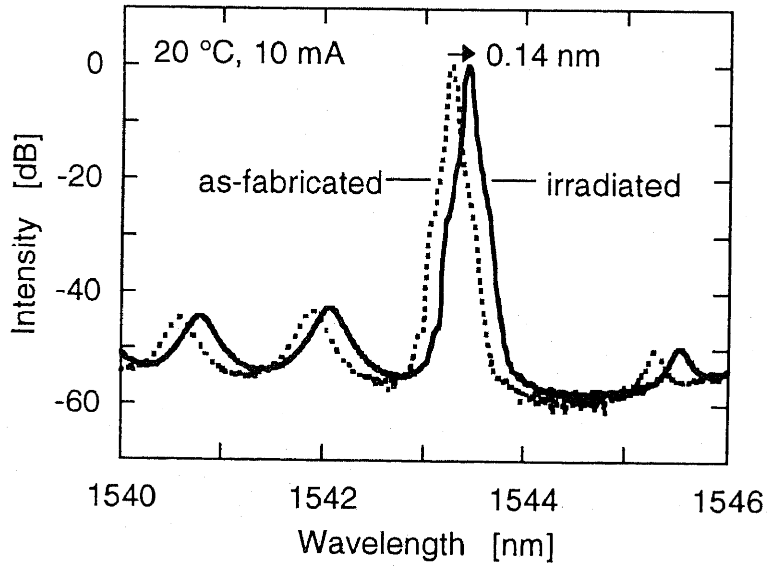

(b) above threshold

Fig. 3.29 Light emission spectra before and after the irradiation at currents below (a) and above (b) threshold.

3.9 Conclusions

In this chapter, wavelength trimming has been realized by making use of refractive index change through photon irradiation. In particular, we have utilized the Se-based chalcogenide glass having the photo-induced refractive index change of 1 % as a constituent of the laser waveguide, and demonstrated the wavelength trimming of 0.14 nm in a 1.55 μm index-coupled DFB laser. Using this method, the oscillation wavelength of the DFB laser is adjustable through the irradiation time.

The use of the external light beam for the wavelength trimming allows us to localize the region where the refractive index changes, and thereby it is possible to adjust oscillation wavelength of elemental DFB lasers, one after another, within an array.

References

[1] S. A. Keneman, "Hologram storage in arsenic trisulfide thin films", Appl. Phys. Lett., vol. 19, pp. 205-207, 1971.

[2] Y. Ohmachi and T. Igo, "Laser-induced refractive-index change in As-S-Ge glasses", Appl. Phys. Lett., vol. 20, pp. 506-508, 1972.

[3] T. Igo and Y. Toyoshima, "A reversible optical change in the As-Se-Ge glass", J. Non-Cryst. Solids, vol. 11, pp. 304-308, 1973.

[4] S. Zembutsu, Y. Toyoshima, T. Igo, and H. Nagai, "Properties of (Se, S)-based chalcogenide glass films, and an application to a holographic supermicrofiche", Appl. Opt., vol. 14, pp. 3073-3077, 1975.

[5] O. Mikami, J. Noda, S. Zembutsu, and S. Fukunishi, "Phase tuning in optical directional coupler by photostructural effect of chalcogenide glass film", Appl. Phys. Lett., vol. 31, pp. 376-378, 1977.

[6] H. Nishihara, Y. Handa, T. Suhara, and J. Koyama, "Direct writing of optical gratings using a scanning electron microscope", Appl. Opt., vol. 17, pp. 2342-2345, 1978.

[7] O. Mikami and S. Zembutsu, "Coupling-length adjustment for an optical directional coupler as a 2×2 switch", Appl. Phys. Lett., vol. 35, pp. 38-40, 1979.

[8] K. Tanaka and Y. Ohtsuka, "Composition dependence of photo-induced refractive index change in amorphous As-S films", Thin Solid Films, vol. 57, pp. 59-64, 1979.

[9] K. Tada, N. Tanio, T. Murai, and M. Aoki, "Sputtered films of sulphur- and/or selenium-based chalcogenide glasses for optical waveguides", Thin Solid Films, vol. 96, no. 2, pp. 141-147, Oct. 1982.

[10] K. Tanaka, Y. Imai, and A. Odajima, "Photo-optical devices by amorphous As-S waveguides", J. Appl. Phys., vol. 57, pp. 4897-4900, 1985.

[11] C. Kittel, "Introduction to solid state physics", 6th ed., John Wiley & Sons, Inc., New York, 1986.

[12] G. Bauer and W. Richter, ed., "Optical characterization of epitaxial semiconductor layers", Springer-Verlag, Berlin, 1996.

[13] A. R. Forouhi and I. Bloomer, "Optical dispersion relations for amorphous semiconductors and amorphous dielectrics", Physical Review B, vol. 34, pp. 7018-7026, 1986.

[14] T. Tamir, ed., "Guided-wave optoelectronics", 2nd ed., Springer-Verlag, Berlin, Heidelberg, 1990.

[15] F. Vermaerke, I. Moerman, G. Vermeire, L. Buydens, P. Van Daele, and P. Demeester, "Simple reliable processing technique for low-threshold high-power strained InGaAs-AlGaAs GRINSCH SQW laser diodes", IEE Proc.-J, vol. 140, pp. 75-79, 1993.

Chapter 4

Wavelength Trimming by Photo-Absorption-Induced Disordering

4.1 Introduction

The change in effective refractive index of the waveguide is determined by the product of the refractive index change and the optical confinement factor in a specific layer where its refractive index changes. Therefore, not only a large refractive index change but also a small refractive index difference between the specific layer and the active layer material, which results in the large optical confinement, are required to accomplish the substantial wavelength adjustment through the refractive index change. In Chapter 3, we have used Se-based chalcogenide glass film having photo-induced refractive index change as a part of the laser waveguide, and demonstrated the wavelength trimming of 0.14 nm at 1.55 μm in an index-coupled DFB laser by He-Ne laser irradiation. This amount of wavelength trimming, however, is smaller than what really is needed in the present WDM systems. The limitation arises from the large refractive index between the chalcogenide glass film (~2.8) and the active layer material (~3.3). At the moment, it is not available the material which has the large refractive index change, together with the refractive index close to that of the active layer material. The optical field is confined in the active layer material most. If we can change its refractive index directly, we can obtain a large amount of the wavelength adjustment.

In this chapter, we propose a wavelength trimming by a photo-absorption-induced disordering (PAID) process. This process enables us to do a permanent refractive index change of the active layer material, which consists of quantum wells, through the external laser beam irradiation. In Section 4.2, the principle of the PAID process is summarized. In Section 4.3, we describe a PAID experiment where an extent of the quantum well disordering was characterized by the photoluminescence measurement. We have applied this PAID process to the conventional ridge waveguide index-coupled DFB laser to adjust its oscillation wavelength. The fabrication sequence of the device is detailed in 4.4 and then the demonstration of the wavelength is presented in Section 4.5. In Section 4.6, we discuss crucial issues for quantitative control of the PAID process.

4.2 Principle of PAID Process

The quantum well structure used as the active layer of the semiconductor laser is an ordered structure and it consists of a stack of multiple layer having the different composition separated spatially by the hetero-interface. Although this structure is stable at the ordinary device operation temperature [1], when it is heated to a certain temperature, different layers separated by hetero-interfaces intermix together and become an alloy state [2]. This phenomenon is commonly known as an alloying, an intermixing, or a disordering since ordered compositions become random order.

Optical properties of this disordered structure are different from those of the original ordered structure. By utilizing this disordering process, it can be locally formed the area having the different band gap energy and the refractive index in a uniform multiple layer structure after the epitaxial growth [3]. This technique is widely used for the fabrication of the optoelectronic devices and their integration, such as an integration of laser diodes, passive waveguides, optical modulators, and photodiodes [4].

Diverse methods have been devised to induce such disordering. In general, localized intermixing is achieved by selectively enhancing the interdiffusion rate of the various layers by increasing the density of dopants introduced by methods such as diffusion of dopants [5], from encapsulants [6] and ion implantation [7] followed by thermal annealing, or point defects, such as vacancies introduced by thermal annealing with dielectric caps, in the crystal [8].

The PAID process is an alternative method to realize the localized intermixing [9]-[13]. This method uses the band gap dependent absorption of the incident laser beam within the active region consists of the quantum wells in a multiple layer structure. By the laser beam irradiation having the proper wavelength, the band-to-band absorption occurs only in the wells and barriers and the free carrier is excited. Then the heat is generated by carrier cooling and nonradiative recombination. This heating has the effect of increasing the interdiffusion rate between the well and barrier materials. As a consequence, the shape of quantum well changes from abrupt to graded and its optical properties changes. The method is impurity free and does not involve a melt phase in the semiconductor processing. Most importantly it is layer composition selective, which is additionally advantageous that it is not restricted to near surface layers. By focusing the incident laser beam, it can be localized that not only the layer but also the area where the intermixing occurs.

Next, we explain the PAID process in the InGaAsP quaternary system grown on the InP substrate. The concept is schematically shown in Fig. 4.1. A Nd: YAG laser beam having the wavelength of 1.064 μm is used for the irradiation. In this system, the InP used as the cladding layer or the substrate is transparent for the laser beam and only the active layer consists of quantum wells absorbs the energy and generates heat which results in the intermixing between the wells and barriers. As the intermixing progresses, the optical gain profile shifts towards the shorter wavelength side and the refractive index near the band gap decreases. We have applied this refractive index change towards the wavelength adjustment.

4.3 Characterization of PAID Process

We first characterized the extent of the quantum well disordering induced by the laser beam irradiation in the InGaAsP quaternary system grown on the InP substrate.

A schematic cross-section of the layer structure of the sample is shown in Fig. 4.2, together with the multiple quantum well band diagram. The active layer consists of five compressively-strained 1.55 μm InGaAsP quaternary quantum wells with the separate confinement heterostructure (SCH) terminated by the InP layer. Both wells and barriers were quaternary and their compositions were $In_{0.728}Ga_{0.272}As_{0.691}P_{0.309}$ and $In_{0.751}Ga_{0.249}As_{0.539}P_{0.461}$, respectively. The strain of +0.68 % was introduced only to the well, and the thickness of wells and barriers were 10 nm. The thickness of the SCH and the top InP were 120 nm and 8 nm, respectively. All layers undoped were grown on a (100)-oriented n^+-InP (2×10^{18} cm^{-3}) substrate by the metal-organic vapor-phase epitaxy (MOVPE). The details of the epitaxial growth were described in Chapter 2.

A layer of SiO_2 was deposited by the magnetron sputtering on the top surface of the material to act both as an antireflection coating for the incident laser beam and to prevent surface reactions with surrounding atmosphere during the irradiation. Assuming that the refractive index of the anti-reflection coating is nf, the optimum thickness d which gives the minimum reflectivity is given by

$$d = \frac{m\lambda}{4n_f} \qquad (4.1)$$

where m is integer and λ is the wavelength of the incident light. On the basis of this equation, the thickness of the SiO_2 with the refractive index of 1.5 at 1.064 μm was adjusted to be 180 nm by controlling the deposition time.

The deposition conditions were summarized as follows. The background and process pressure were 3×10^{-5} Pa and 0.5 Pa, respectively. The distance between the sample and the target was 8 cm. Oxygen and argon were introduced to the chamber with the flow of 3 and 1 sccm, respectively. The incident power was 300 W. No heat

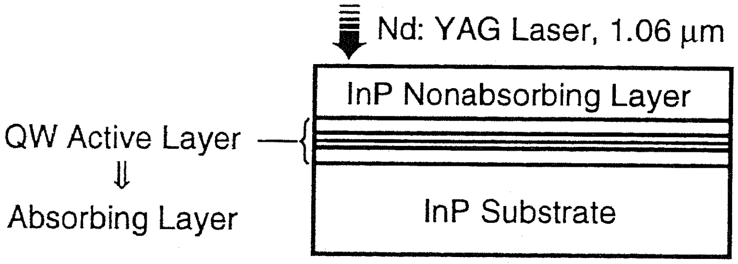

Fig. 4.1 A concept of the photo-absorption-induced disordering.

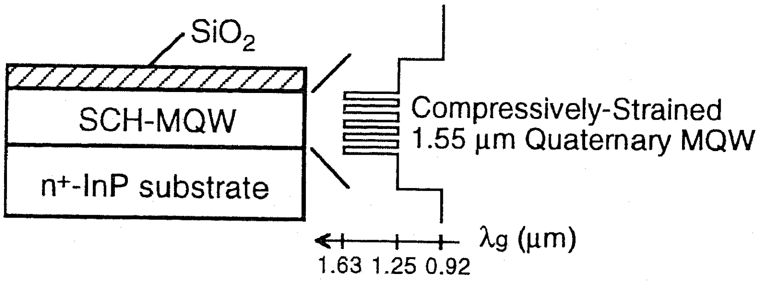

Fig. 4.2 A cross section of the layer structure of the sample for photo-absorption-induced disordering experiment with multiple quantum well band diagram.

was applied to the substrate. The deposition rate was 0.2 nm/sec.

We measured the reflectivity by pointing a neodymium yttrium-aluminum-garnet (Nd: YAG) laser with wavelength of 1.064 μm perpendicularly to the sample and measured the reflection by an optical power meter. The measured reflectivity of the sample was 8 %.

Figure 4.3 shows the schematic diagram of the experimental setup for the PAID process. The sample with a size of ~5 mm × 5 mm was attached to the copper plate having the heater inside with a silicon grease which had a high thermal conductivity. A Nd: YAG laser (CVI, YAG-MAX Laser C-92) operating continuous wave and multimode with wavelength of 1.064 μm was used for the irradiation. The laser beam had a Gaussian profile as shown in Fig. 4.4 with a diameter of 1.6 mm. The power density at the sample was 1 W/mm^2. The beam alignment was done by using a He-Ne laser beam with wavelength of 632.8 nm, which was codirected previously with the Nd: YAG laser beam.

We first irradiated the sample at the room temperature for 10 min. The extent of the intermixing of the quantum well was characterized by the room temperature photo-luminescence (PL) measurement.

The PL measurement setup is schematically shown in Fig. 4.5. An argon ion laser with wavelength of 514.5 nm was used for the pump source. The laser beam was focused on the sample through a plano-convex lens. The luminescence was collected with a large diameter convex lens and introduced to a monochromator. In order to eliminate the line from the Ar ion laser, a high pass filter with cutoff wavelength of 1.1 μm was inserted just before the entrance of the monochromator. A spectrum was detected by a Ge pn-photodiode. The electric signal from the detector was amplified with a pre-amplifier and then a lock-in amplifier where the background noise was suppressed with a chopper inserted in an incident path. The output was sent to the computer, through a voltage-frequency converter, where the data was recorded while controlling the monochromator via RS-232C.

The PL spectra before and after the irradiation are shown in Fig. 4.6. No shift is found which indicates the temperature at the active layer did not reach the activation temperature where the intermixing occurs. The determination of the activation temperature will be discussed in Section 4.6.

Here we consider the relation between the temperature and the given power using the simple 1 dimensional model as shown in Fig. 4.7 where it is assumed that the interface between the material and the surrounding atmosphere is thermally isolated and a heat sink has a capability of absorbing heat from the material without the change of temperature itself. The temperature T_1, at the point where the power P is provided, is given by

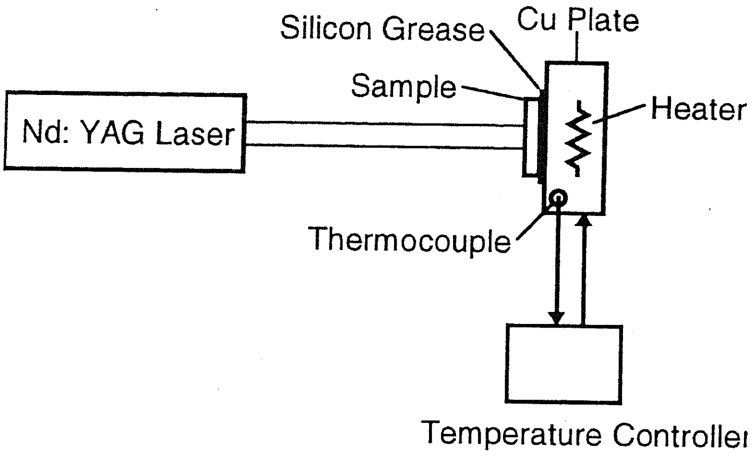

Fig. 4.3 Experimental setup for the photo-absorption-induced disordering.

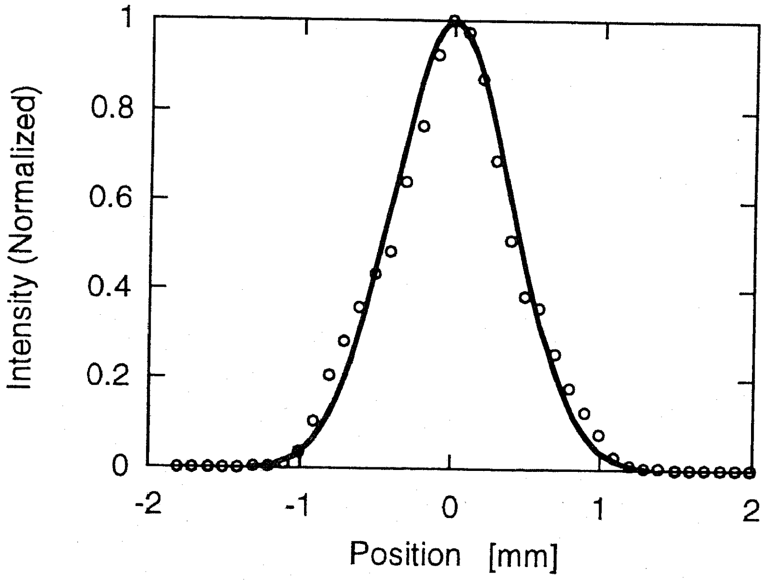

Fig. 4.4 Measured beam profile of a Nd: YAG laser for the photo-absorption induced disordering experiment.

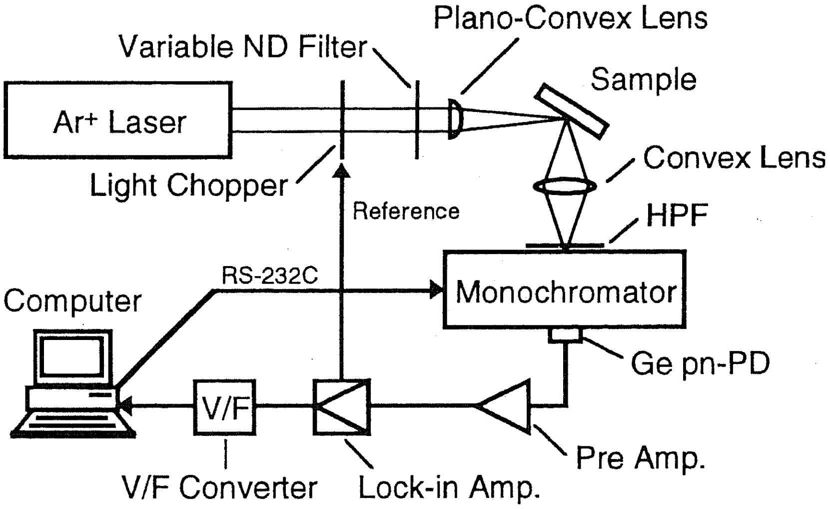

Fig. 4.5 Schematic diagram of the photo-luminescence measurement.

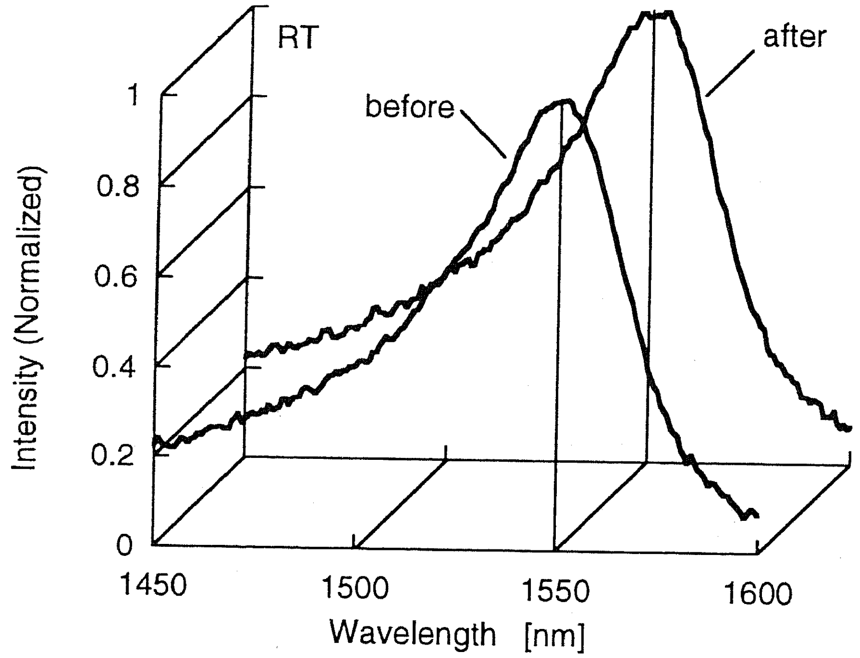

Fig. 4.6 Measured PL spectra of the sample irradiated with Nd: YAG laser at room temperature.

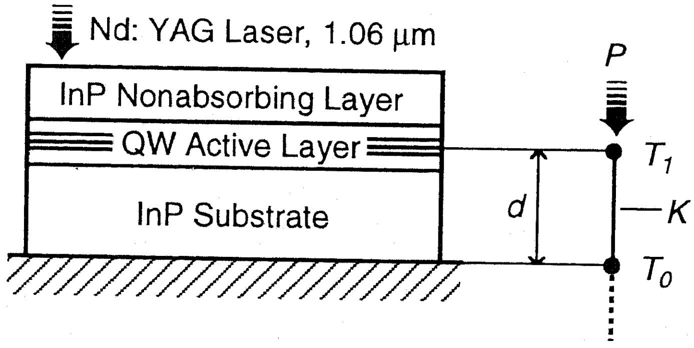

Fig. 4.7 A simple 1 dimensional model for the relation between the incident power and the temperature.

$$T_1 = T_0 + \frac{P}{Kd} \qquad (4.2)$$

where K is the thermal conductivity, d is the thickness, and T_0 is the heat sink temperature. This equation suggests that the activation temperature can be obtained by elevating the heat sink temperature without increasing the power of incident beam.

On the basis of this consideration, we increased the temperature of the copper plate to 240 °C and then repeatedly irradiated the sample. In order to evaluate the disordering which might be induced by the elevated temperature, another sample was simultaneously placed without the irradiation. The PL at room temperature was measured after each irradiation. The measured PL spectra are shown in Fig. 4.8. The PL peak shifted towards the shorter wavelength side as the irradiation time increased. After 3 min of irradiation, the shift was 3 nm. The total amount of the shift of 8 nm was obtained after 150 min of irradiation. As shown here, the band gap can be adjusted through the irradiation time. Fig. 4.9 shows the PL spectra of the sample without the irradiation. The PL peak wavelength did not change. From these results, we understood that the elevated temperature of the heat sink facilitated to reach the activation temperature without the increase of the incident power density, and also we confirmed that the sample structure was stable at 240 °C and the disordering was induced by the laser beam irradiation.

4.4 Device Structure and Fabrication Procedure

In the previous section, the quantum well disordering induced by the laser beam irradiation in the InGaAsP quaternary system grown on the InP substrate was characterized with regard to the band gap shift. The band gap shift is always accompanied by the refractive index change. We have applied this refractive index change caused by the PAID process to the oscillation wavelength adjustment of DFB lasers which oscillate at 1.55 μm.

A cross section of the device, together with the multiple quantum well band diagram is illustrated in Fig. 4.10, which we have used it for the wavelength trimming experiment. This is a conventional ridge waveguide index-coupled DFB laser.

The device fabrication sequence is illustrated in Figs. 4.11. In the first step growth, a n-InP (100 nm, 5×10^{17} cm^{-3}) buffer layer, an active region consisted of five compressively-strained 1.55 μm InGaAsP quaternary quantum wells with a separate confinement heterostructure (SCH), a p-InP (50 nm, 5×10^{17} cm^{-3}) guiding layer, a p-InGaAsP (λ_{PL} = 1.25 μm, 10 nm, 5×10^{17} cm^{-3}) grating layer, and a p-InP (10 nm, 5×10^{17} cm^{-3}) termination layer were grown on a (100)-oriented n^{+}-InP (2×10^{18} cm^{-3})

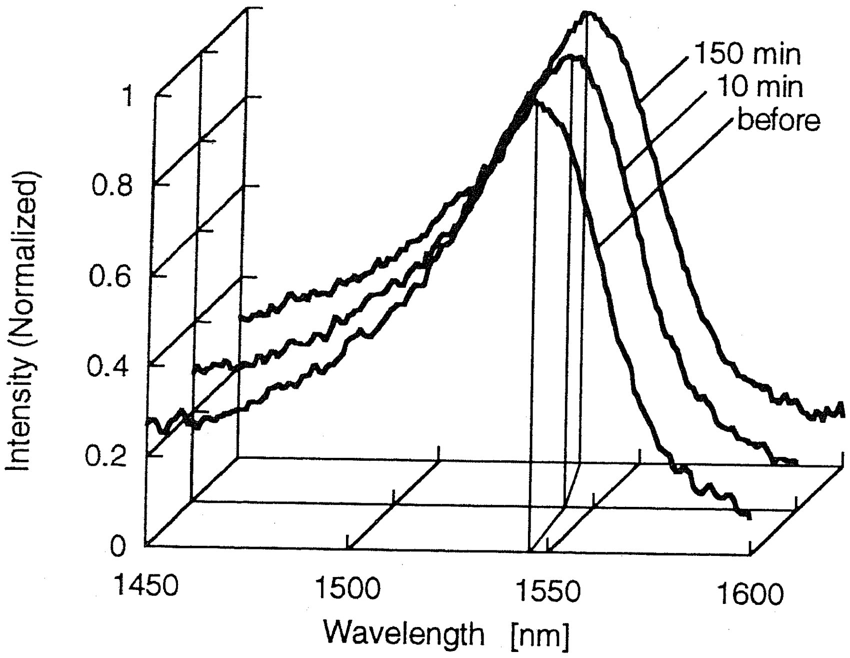

Fig. 4.8 Measured PL spectra of the sample irradiated with Nd: YAG laser at 240 °C.

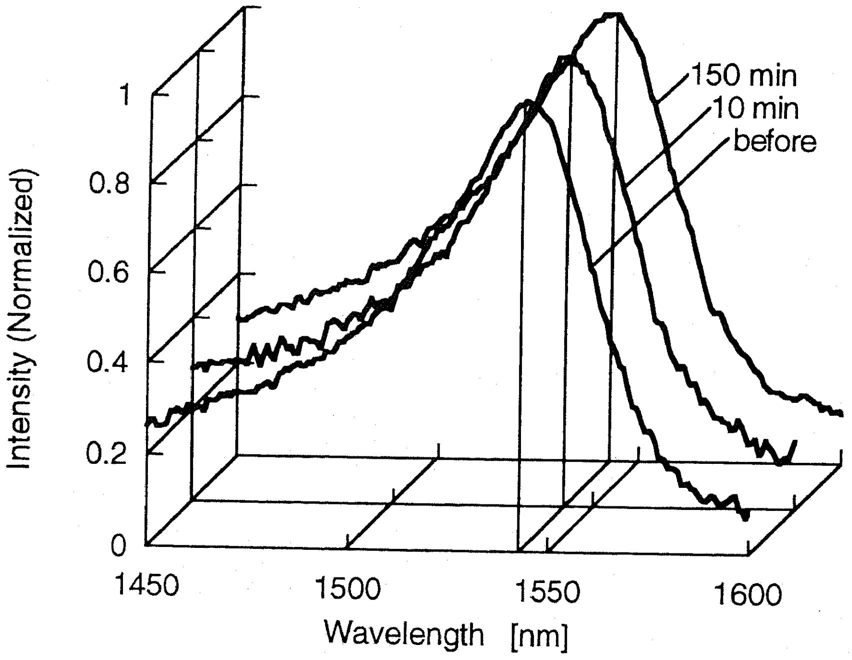

Fig. 4.9 Measured PL spectra of the sample kept at 240 °C without irradiation.

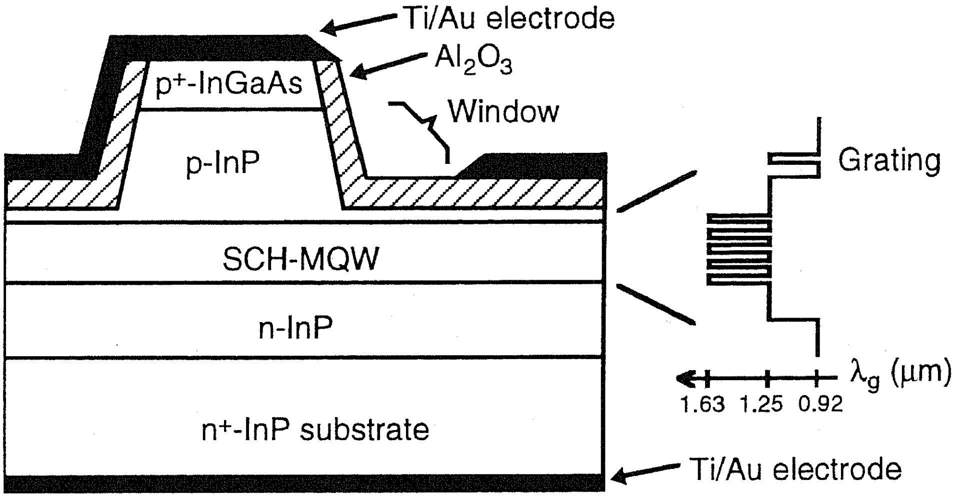

Fig. 4.10 Schematic lateral cross-section of the ridge waveguide DFB laser and the MQW band diagram.

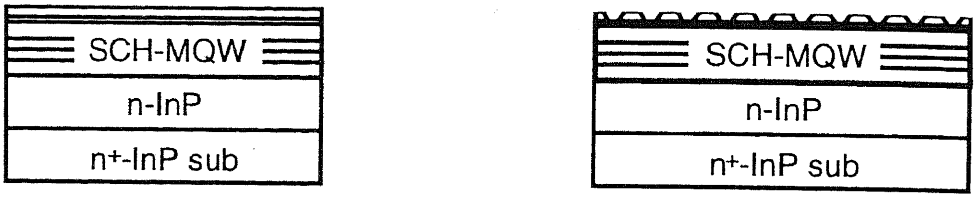

(a) 1st growth

(b) grating formation

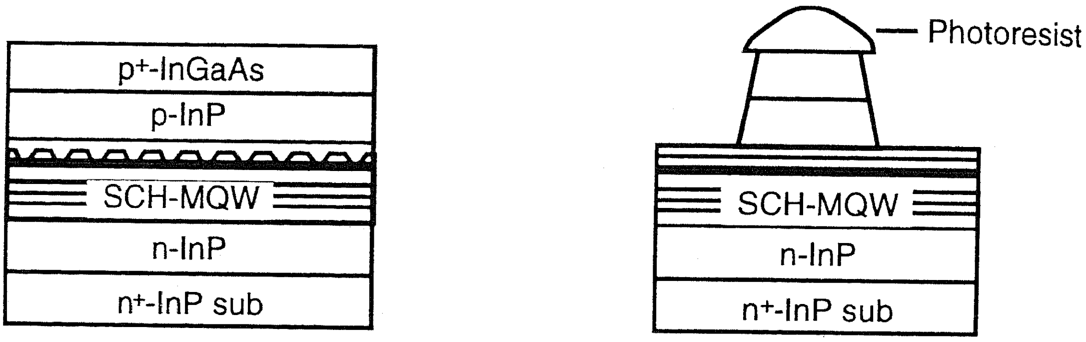

(c) 2nd growth

(d) mesa formation

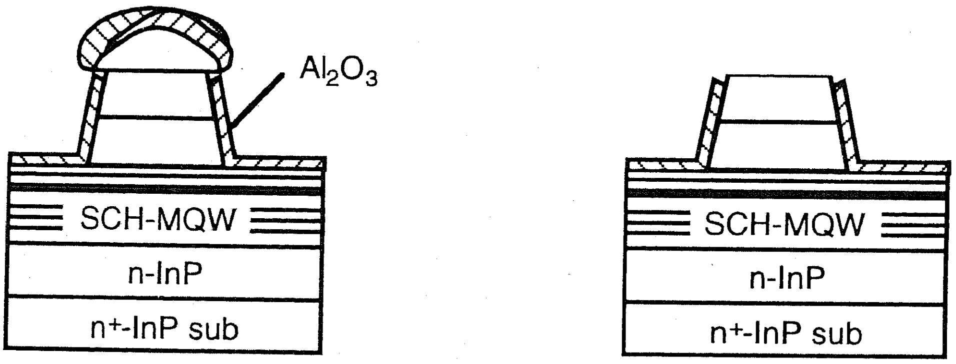

(e) Al_2O_3 deposition

(f) lift-off

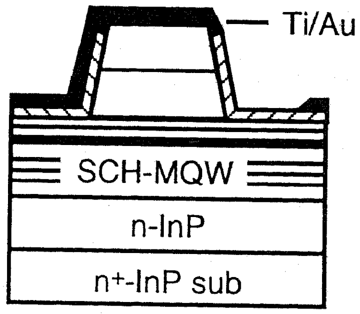

(g) Ti/Au evaporation

Fig. 4.11 The fabrication process sequence.

substrate (Fig. 4.11 (a)). The active region was identical to the structure which was used for the characterization of the PAID process described in Section 4.2. A first order uniform diffraction grating with a period of 240 nm was formed in the grating layer by the holographic exposure method and wet chemical etching (Fig. 4.11 (b)). The solution used was saturated bromine water (SBW) : HBr : H_2O (1 : 10 : 20, 20 °C). In the second step growth, a p-InP (80 nm, 5×10^{17} cm^{-3}) guiding layer, a p-InGaAsP (λ_{PL} = 1.25 μm, 3 nm, 3×10^{17} cm^{-3}) etch stop layer, a p-InP (700 nm, 5×10^{17} cm^{-3}) cladding layer, and a p^+-InGaAs (200 nm, 5×10^{19} cm^{-3}) contact layer were grown on the grating (Fig. 4.11 (c)). After the regrowth, the waveguide was formed by wet chemical etching. The solution used were the H_2SO_4 : H_2O_2 : H_2O (1 : 1 : 5, 5 °C) and HCl (20 %, RT) for the InGaAs contact layer and InP cladding layer, respectively. The etching was stopped at p-InGaAsP etch stop layer and thus the ridge waveguide was formed (Fig. 4.11 (d)). After the etching, the photoresist mask was not removed but it was left on the top of the waveguide to serve as a lift off mask. In the next step, an Al_2O_3 passivation layer with thickness of 200 nm was deposited on both sides of the waveguide (Fig. 4.11 (e)). The Al_2O_3 on top of the waveguide and photoresist mask were removed by a simple lift-off process in acetone and thus the opening for the contact was formed in a self-aligned manner (Fig. 4.11 (f)). Then the Ti/Au top electrode was evaporated as a p-type contact (Fig. 4.11 (g)). In order to form a window for the external light irradiation, the sample was hold at 45 ° off during the evaporation. The thickness of Ti and Au were 30 nm and 120 nm, respectively. Then the sample was thinned to about to 100 μm by lapping. Finally Ti/Au contact was deposited on the back side of the substrate as an n-type electrode by the same amount as the top one. The high doping level of the top contact layer and the rough surface of the lapped back facilitated the ohmic contact formation without the alloying step. The wafer was cleaved into discrete chips with both facets were left uncoated. The device was bonded on a chip carrier with tin. Scanning electron micrographs of the lateral cross section and the bird's-eye view of the device were shown in Figs. 4.12 (a) and (b), respectively. The window for the external light irradiation was formed the left side of the ridge waveguide with width of ~ 2 μm.

4.5 Wavelength Trimming Experiment

Next, we carried out the wavelength trimming experiment. The sample measured here had a ridge width of 4 μm and a cavity length of 400μm. Figure 4.13 shows a schematic diagram of the experimental setup for the laser beam irradiation. The sample was placed at an angle of 45 ° off on an aluminum plate with the heater inside. The temperature of the plate was kept constant at 240 °C. As described in

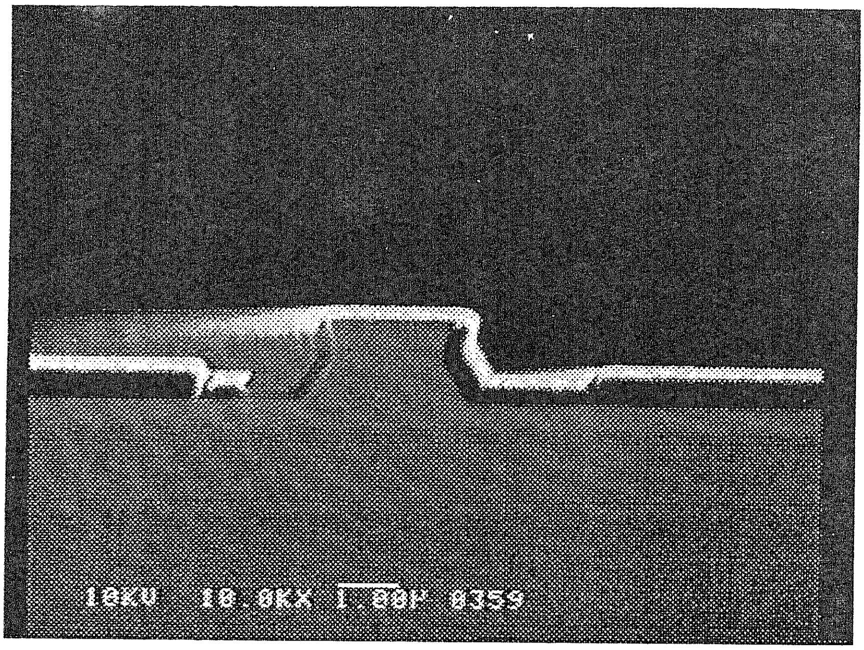

(a) cross-section

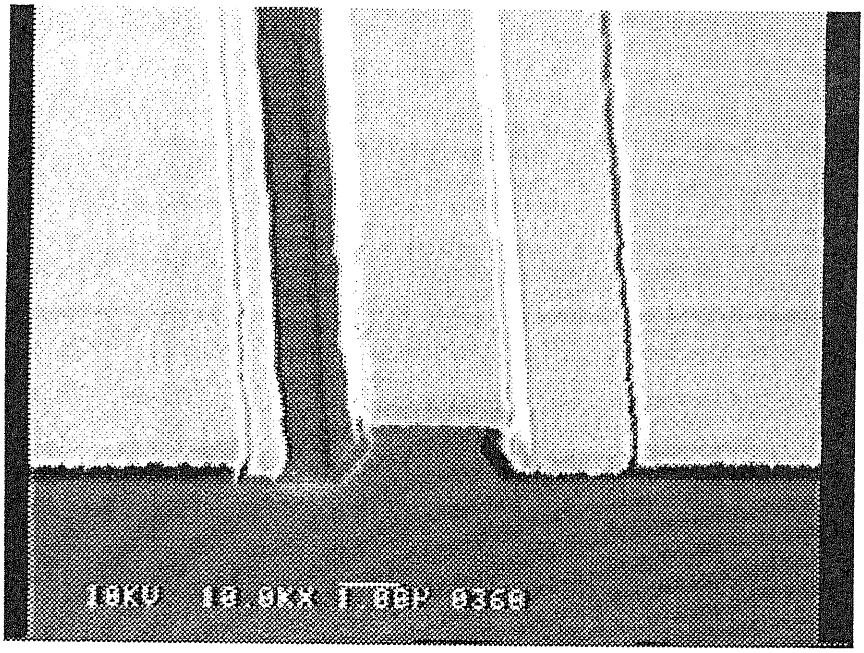

(b) bird's-eye view

Fig. 4.12 Scanning electron micrograph of (a) the cross-section and (b) the bird's-eye view of the sample.

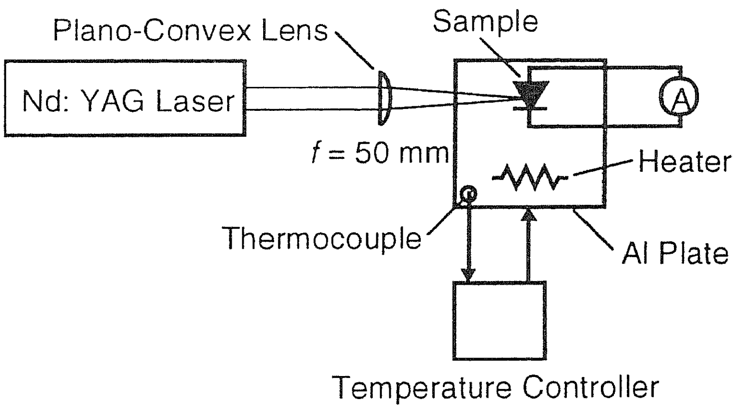

Fig. 4.13 A schematic diagram of the experimental setup for the wavelength trimming by photo-absorption-induced disordering.

the previous section, the elevated background temperature facilitates the reduction of the incident laser power required for the disordering to occur. A Nd: YAG laser (NEC, SL114) operating continuous wave and multimode with a wavelength of 1.064 μm, a beam diameter of 2 mm, and an output power of 10 W was used for the irradiation. The laser beam was concentrated on the center of the sample through a plano-convex condensing lens with a focal length of 50 mm and introduced to the active region through a window formed beside the laser stripe. The beam was aligned at the position where the absorption photo-current from the laser was maximized. The beam was kept at the same position during the irradiation.

The beam diameter and the power density at the focus were estimated to be 35 μm and 2×10⁴ W/mm², respectively, using [14],

$$\phi_o = \frac{\dfrac{f}{Z_0}}{\sqrt{1+\left(\dfrac{f}{Z_0}\right)^2}}\phi_i \qquad (4.3)$$

$$Z_0 = \frac{\pi\phi_i^2}{4\lambda} \qquad (4.4)$$

where ϕ_o and ϕ_i are the diameters of the output and the input beams, f is the focal length, and λ is the wavelength, and

$$I = \frac{8}{\pi\phi_o^2}P \qquad (4.5)$$

where I is the power density and P is the total power.

During the irradiation, the top Ti/Au electrode and the Al_2O_3 passivation layer acted as a total reflector and an anti-reflection coating for the incident beam, respectively. As a result, the energy from the Nd: YAG laser was absorbed only by the active region under the window. As compared with the width of the window (~2 μm), the beam diameter of the Nd: YAG laser was quite large (~35 μm). Therefore, most of the energy was reflected at the electrode and only a small part of the beam was introduced to the active layer. This mismatch resulted in the necessity of the high power density of the laser beam to heat the active layer to an activation temperature.

The rapid rise of temperature may cause a damage to a sample, since it consists of various materials with the different thermal expansion coefficient. In order to avoid the thermal shock, the output power of the Nd: YAG laser was gradually increased with a rate of 3 W/min. The duration of the irradiation was 30 min. No damage was found on the sample after the irradiation.

First we measured the absorption photo-current spectra from the sample at room temperature before and after the irradiation to observe the band gap shift induced by the intermixing. Figure 4.14 shows a schematic diagram of the measurement setup. The tunable light source was derived from a white light source consisted of a tungsten bulb coupled into a monochromator. The output was then concentrated on the sample and introduced to the active layer through the window. No reverse-bias voltage was applied to the sample. Figure 4.15 shows measured spectra of the photo-current near the band edge of the sample before and after the irradiation. The peaks around 1550 nm are associated with the exciton. As a consequence of the quantum well intermixing, the edge shifted towards the shorter-wavelength side by 5.9 nm. No observable broadening was found in the exciton peak.

The lasing characteristics were measured by keeping the temperature constant at 20 °C. Figure 4.16 shows the output power as a function of the driving current. The threshold current is increased from 15 mA to 17 mA by the irradiation. The PAID process may not involve the diffusion of dopants of the cladding layer into the active region, which incurs the free carrier absorption, thus, this slight increase in the threshold current is attributed to the gain decrease at the oscillation wavelength of 1550 nm, which can be inferred from Fig. 4.15.

Figures 4.17 (a) and (b) show the lasing spectra below (14 mA) and above (25 mA) the threshold currents, respectively. The wide gap around 1551.5 nm beside the main mode corresponds to the stop band.

Besides the threshold increase, the degradation of the lasing characteristic was found in the side mode suppression ratio at 25 mA where it was decreased from 46 dB to 40 dB through the irradiation. The origin of this variation will be discussed in the next section.

Here we look at the shift of oscillation wavelength. It shifted towards the shorter-wavelength side as the refractive index decreased by the quantum well intermixing. The amount of wavelength shift was 0.23 nm below the threshold. Above the threshold, the carrier density inside the cavity is clamped at the threshold value. The small increase in the threshold current in Fig. 4.16, and therefore the increase in the carrier density, decreased the refractive index further. It resulted in the total wavelength shift (including the effects of the intermixing and increased carrier density) of 0.36 nm in Fig. 4.17 (b). This shift is 2~3 times larger than the previous demonstration described in Chapter 2, where the wavelength trimming was realized by making use of the photo-induced refractive index change in chalcogenide glasses.

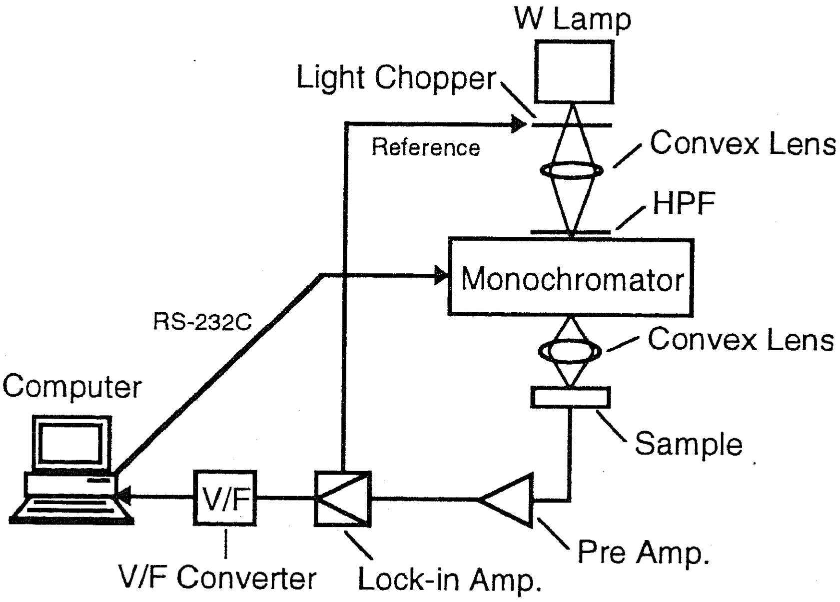

Fig. 4.14 A schematic diagram of the setup for the absorption photocurrent measurement.

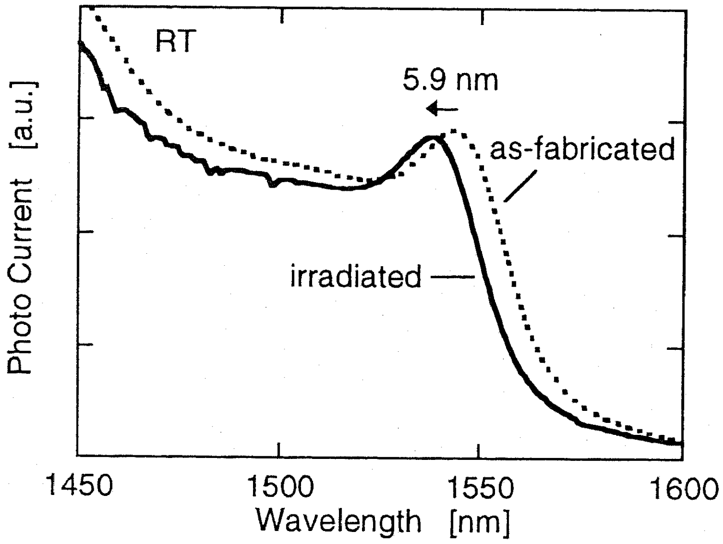

Fig. 4.15 Photocurrent spectra near the band edge of the active MQW layer before and after the Nd: YAG laser beam irradiation.

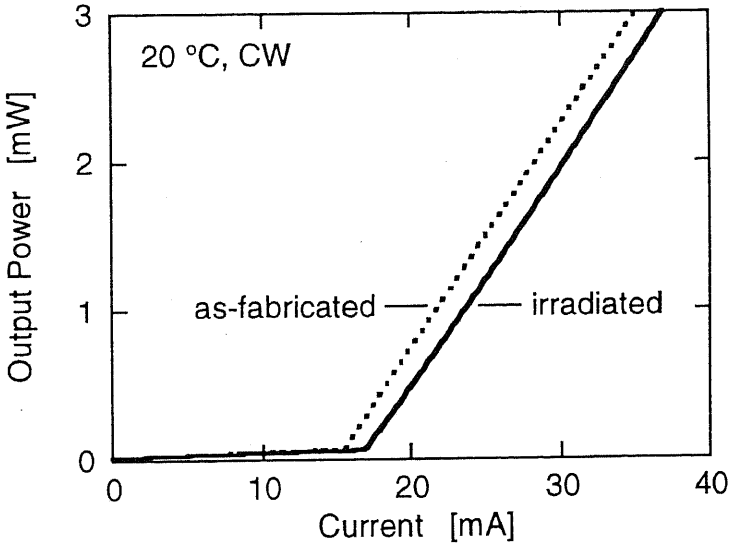

Fig. 4.16 CW light output vs. injection current characteristics at 20 °C.

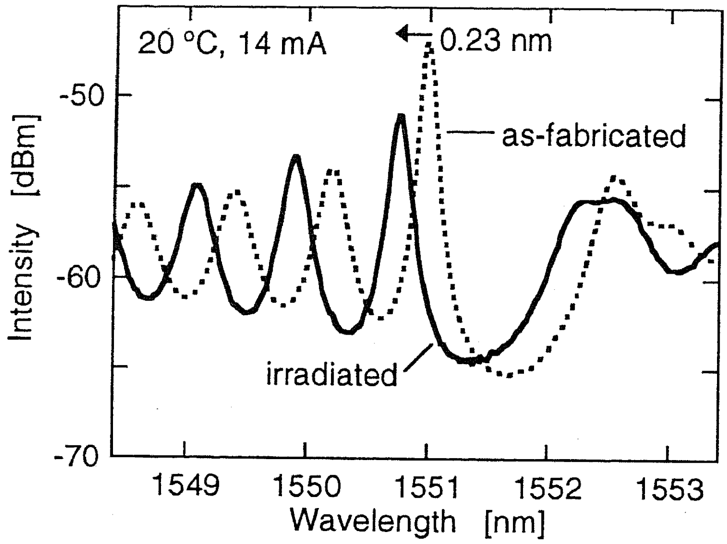

(a) below threshold

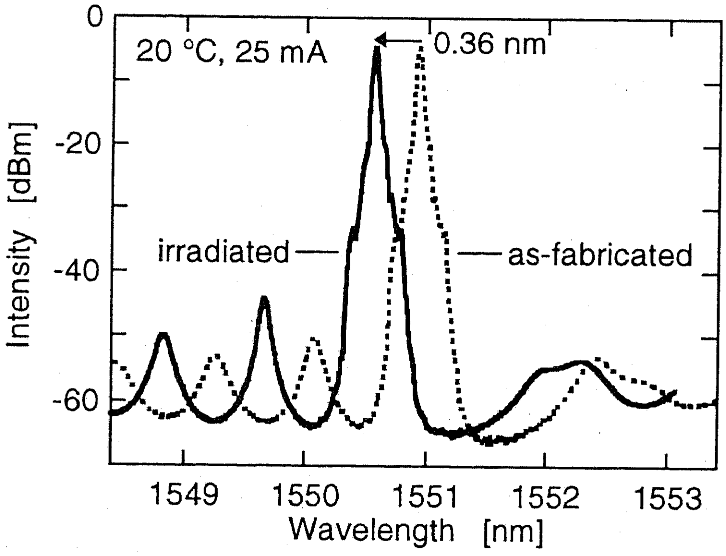

(b) above threshold

Fig. 4.17 Oscillation spectra before and after the Nd: YAG laser irradiation at currents below (a) and above (b) the threshold.

4.6 Control of PAID Process

In this section, we discuss crucial issues for quantitative control of the PAID process. Those include measurement of the temperature of the active layer during the process and the spatial distribution of the disordering. At the end of this section, we propose a process control of PAID through a monitor of the absorption photo-current from the sample.

4.6.1 *in-situ* Temperature Measurement

The disordering basically obeys the product of an interdiffusion rate of materials which compose quantum wells and duration of the process. The interdiffusion rate is a function of a temperature, therefore, measurement and control of the temperature are indispensable for the accurate control of the PAID process.

By the laser beam irradiation, carriers are excited in the active layer, and then most of them recombine accompanied by the radiation of photons and the remnants generate the heat through nonradiative recombination which results in the disordering. The luminescence from the sample is an accurate measure of the temperature in the active region, since its spectrum reflects the band gap energy which is a function of the temperature. We have examined a possibility of the determination of the temperature in the active region through the measurement of photoluminescence from the sample during the irradiation.

We first measured the photo-luminescence at various temperatures. The sample was identical to the structure which was previously shown in Fig. 4.2. Figure 4.18 shows the measured PL spectra at temperatures of -196, 25, 100, 150, 200, and 250 °C, respectively. For the measurement at -196 °C, the sample was immersed in liquid nitrogen. The heating was done by attaching the sample to the copper plate having the heater inside with the high thermal conductive silicon grease. A PbS photoconductor was used as a photodetector which had a sensitivity up to 3 μm. As the temperature increased, the PL peak shifted towards the longer-wavelength side, and at the same time, the width became broad. And furthermore, the intensity of luminescence rapidly decreased due to the broadening of the carrier distribution in energy. The dots in Fig. 4.19 show the PL peak wavelength derived from the Fig. 4.18 as a function of the temperature. The variation of bandgap with temperature $E_g(T)$ can be expressed approximately by a universal function [15],

$$E_g(T) = E_g(0) - \frac{\alpha T^2}{T+\beta}. \qquad (4.6)$$

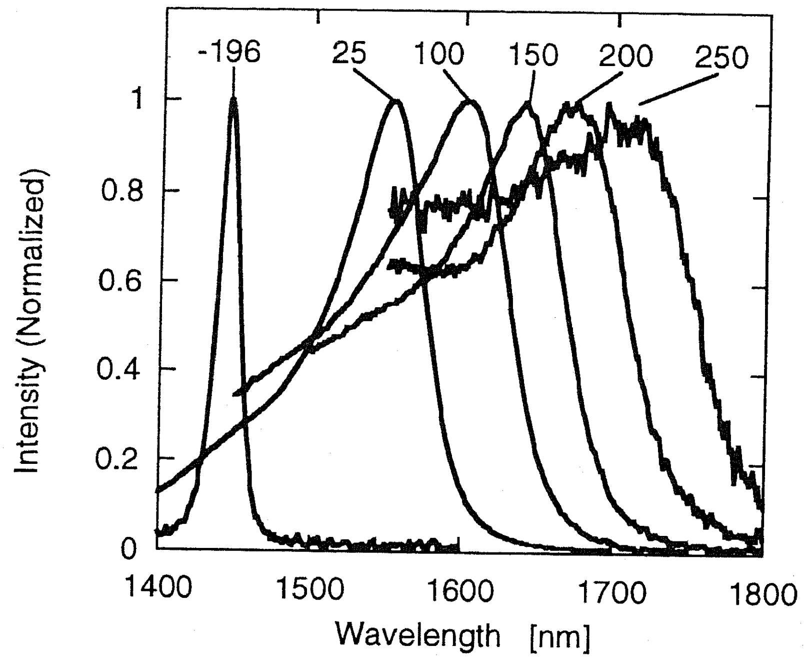

Fig. 4.18 Measured photo-luminescence spectra at various temperature.

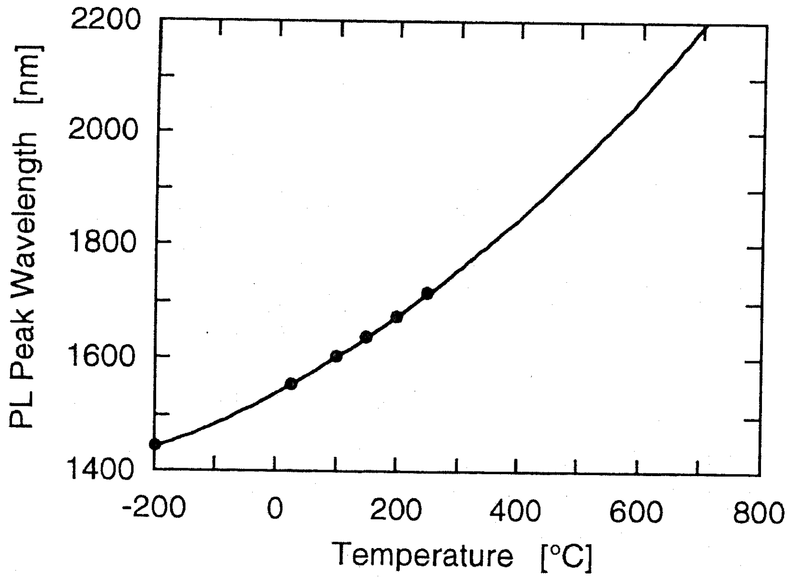

Fig. 4.19 PL peak wavelength as a function of temperature. Dots denote the measured points. A solid line is a fitting curve.

By fitting this equation to the measured PL peak wavelength, $E_g(0)$, α, and β can be determined as fitting parameters. The solid line shown in Fig. 4.19 is a fitting curve and parameters are, $E_g(0) = 0.86621$ eV, $\alpha = 0.00036821$, and $\beta = 183.32$, respectively. By making use of this curve, we can extrapolate the temperature from the PL peak wavelength during the PAID process.

Figure 4.20 shows a schematic diagram of a setup for an *in-situ* temperature measurement. A 600 μm diameter large-core optical fiber was placed in the close vicinity of the sample to collect the photo-luminescence. The output was coupled into the monochromator and then introduced to the PbS photoconductor.

The measurement was applied to the same sample. We successively irradiated the sample with different incident power density and measured the luminescence. The background temperature was kept at 240 °C. The measured spectra are shown in Fig. 4.21 at power densities of 0.7, 2.0, 3.4, 4.8, 6.8, 12.3, 17.0 W/mm^2.

It should be mention that the PL peak might shift towards the shorter-wavelength side during the measurement, since the incident power densities were large enough to induce the disordering.

The peak wavelength, together with the temperature extrapolated from Fig. 4.19 are shown in Fig. 4.22 as a function of the power density. At 0.7 W/mm^2, the peak shows the temperature of the heat sink which was kept at 240 °C. As the power density increased, the peak wavelength monotonously shifted towards the longer-wavelength side, which clearly indicated that the active region was heated by the laser beam irradiation. The relation between the temperature and the power density is not linear but it shows a saturable tendency. The measured temperature was reached to 350 °C at power density of 17.0 W/mm^2. After the irradiation, we have measured the room temperature PL of the sample to verify whether the disordering took place or not. The measured PL spectra before and after the irradiation in Fig. 4.23 clearly indicates that the substantial disordering was induced.

These results posed us a difficult question. The quantum well structure of the sample should be stable up to its growth temperature of 610 °C. How could it be possible to induce the quantum well intermixing at temperature less than 350 °C?

The determination of the temperature in the active region through the measurement of photo-luminescence from the sample during the irradiation is subject to considerable uncertainty. The temperature of the sample is not uniform due to a part of the sample is irradiated with nonuniform laser beam. Thus the PL spectrum does not indicate the maximum temperature, but it shows an average of the whole area. As described above, the PL intensity rapidly decreases as the temperature increases. As a result, the luminescence from the low temperature area governs the whole spectrum.

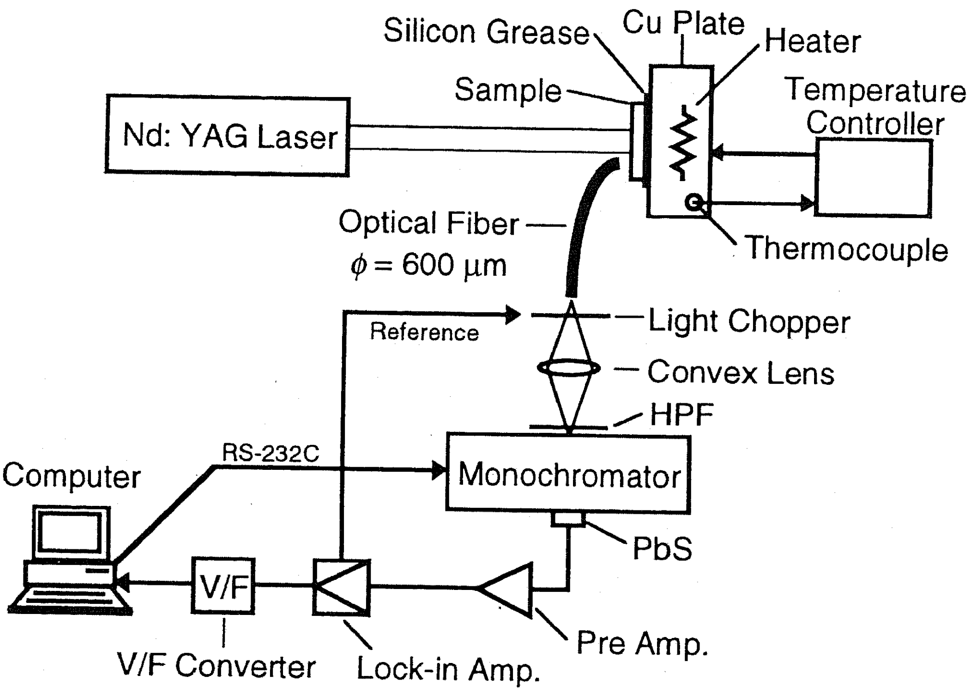

Fig. 4.20 A schematic diagram of the setup for *in-situ* photoluminescence measurement.

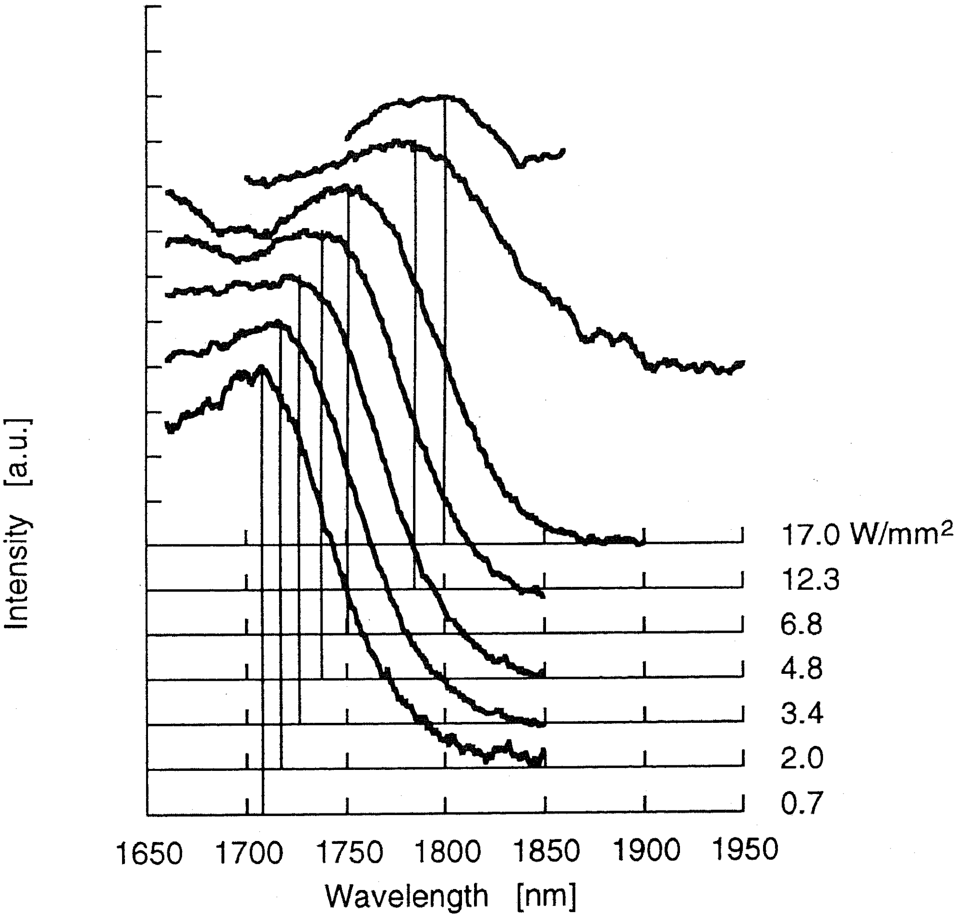

Fig. 4.21 Measured photo-luminescence spectra at various incident power density of Nd: YAG laser.

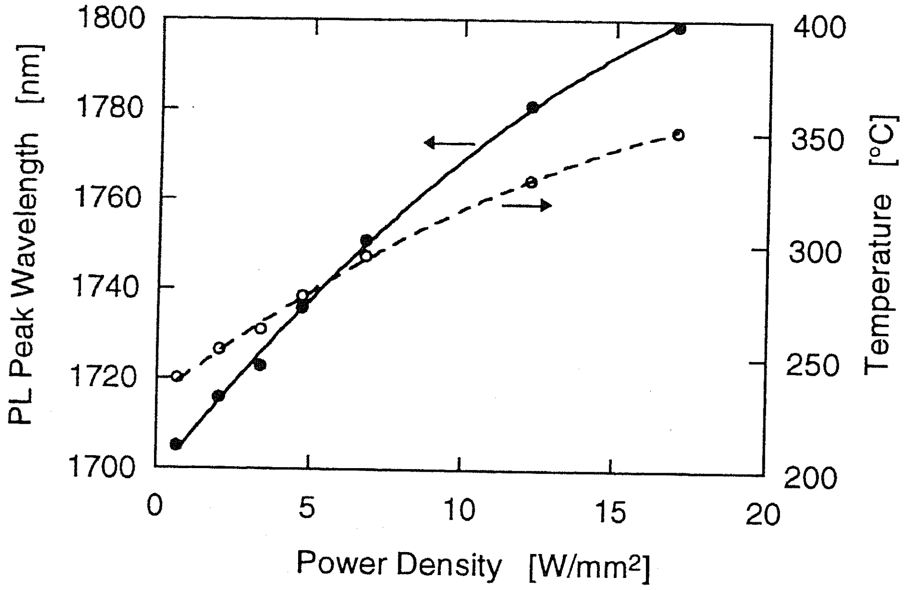

Fig. 4.22 Measured PL peak wavelength and temperature extrapolated in Fig. 4.19 as a function of the incident power density of Nd: YAG laser.

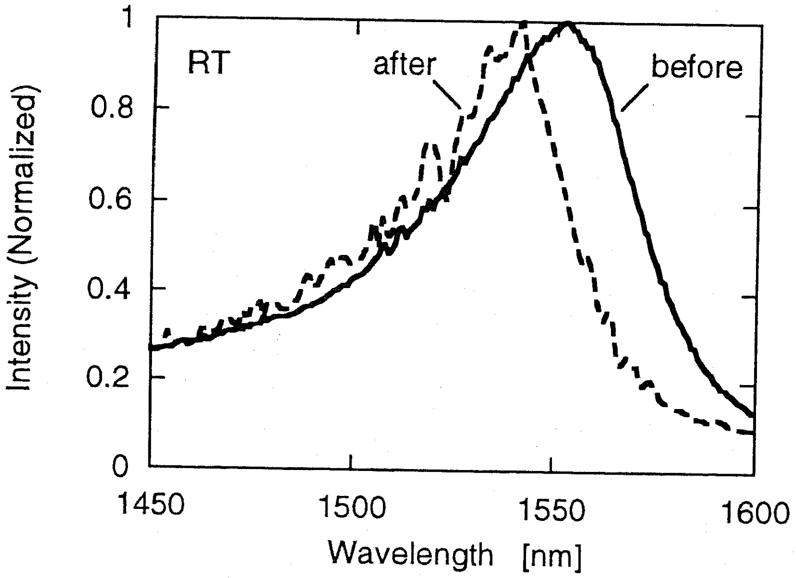

Fig. 4.23 Measured PL spectra before and after the irradiation.

In spite of this uncertainty in the temperature, this method is useful for the control of the PAID process where a monitoring of the relative temperature between each process is necessary, instead of the absolute temperature.

Next, we have carried out the conventional furnace annealing inside the reactor of the MOVPE to estimate the activation temperature where the disordering occurs. The layer structure of the sample was the same as described above. In order to investigate the dependency of the disordering on dielectric caps on the samples, three types of samples were prepared, without cap, with SiO_2 cap, and with Al_2O_3 cap, respectively. The SiO_2 with thickness of 180 nm and the Al_2O_3 with thickness of 150 nm were deposited by the magnetron sputtering and the electron-beam evaporation. During the annealing inside the reactor of the MOVPE, phosphorus was supplied for the sample without cap to prevent its desorption from the surface. The temperatures we tried were 400, 500, 600, and 700 °C, respectively. The photoluminescence spectra were measured before and after the annealing with an Ar ion laser as a pump source. Table 4.1 lists the result of the furnace annealing. Dots denote the substantial disordering did occur. On the other hand, marks an X on the list denote that shifts in PL peaks were not observed. At 700 °C, all types of samples were disordered. Below 700 °C, only the sample with SiO_2 cap was disordered even at 400 °C. The point defect which is induced in the crystal by the thermal annealing with dielectric caps at very high temperature typically above 800 °C, did not involve this disordering which occurred at 400 °C.

These results suggest that the disordering was induced by the thermal stress which arose from the different thermal expansion coefficients between the cap and the InP. A thermal expansion coefficient of Al_2O_3 is close to that of InP, therefore, the thermal stress at the interface between them is small. As a consequence, the disordering occurred only at 700 °C where the sample without cap was simultaneously disordered. On the contrary, the difference of the thermal expansion coefficient is large between SiO_2 and InP. As a result, the sample was easily disordered at low temperature.

In the PAID process, a large thermal stress between the active layer and the surrounding region is induced, since only the active region is selectively heated while the surrounding region includes the dielectric cap keeps the low temperature. As a consequence, irrespective of the material of the dielectric cap, the disordering is easily induced at very low temperature through laser beam irradiation.

The low process temperature is preferable, however, the involvement of the thermal stress in the disordering makes the analysis on the process complicated. Thus, the geometrical structure must be taken into account for the analysis and control of the PAID process.

TABLE 4.1 Cap dependency of disordering by furnace annealing.

Temperature	Cap		
	—	SiO_2	Al_2O_3
700 °C	●	●	●
600 °C	×	●	×
500 °C	×	●	×
400 °C	×	●	×

Another factor which dominates the disordering process is the composition of wells and barriers. The intermixing occurs between two layers with different composition, and it ceases when each composition becomes the same. In our structure, both wells and barriers are the InGaAsP quaternary systems and the composition difference is only in the group V materials of the phosphorus and the arsenic while the contents of the group III materials of the indium and the gallium are the same. Therefore, the disordering results from the difference in the group V contents.

Besides the composition difference, the strain which is introduced to wells plays an important roll in the disordering. The disordering process progresses towards the state where the total energy is minimum. Thus the strain decreases as the disordering progresses which results in the change of the band structure of the active layer.

4.6.2 Spatial Distribution of Disordering

Next we have characterized the PAID process in terms of the spatial distribution of the disordering. The longitudinal and the lateral distributions were measured through the microscopic electro-luminescence and photo-luminescence measurement, respectively.

Figure 4.24 shows a schematic diagram of the setup for the measurement of longitudinal distribution of the disordering. The sample used in Section 4.4 was operated at 14 mA, and its temperature was kept constant at 20 °C. Spatially selective electro-luminescence measurements were performed using a fiber probe with a core diameter of 10 μm and the tip radius of 20 μm. This fiber probe was mounted on a translation stage.

The spontaneous emission was collected along the cavity at intervals of 50 μm through the window formed beside the ridge waveguide by the fiber probe, and then introduced to the optical spectrum analyzer.

Figure 4.25 shows the longitudinal distribution of measured spontaneous emission spectra of the sample. Although the positions of band edges are almost the same throughout the cavity, the emissions around the center region have broad peaks and they are located shorter-wavelength side as compared with the emission near the facets. The broad peak indicates that the shape of quantum well is changed from abrupt to graded by the disordering through the laser beam irradiation. This distribution along the cavity is attributed to the nonuniform irradiation, since the laser beam with diameter of 35 μm was concentrated on the center of the sample and it was kept at the same position during the irradiation.

This longitudinal distribution of the disordering introduces the nonuniform

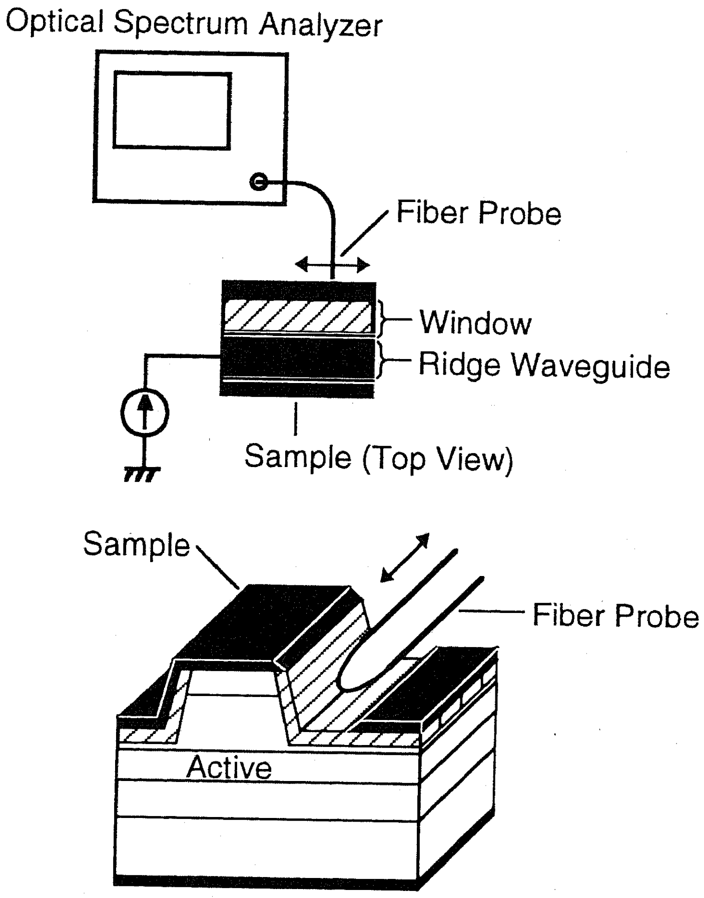

Fig. 4.23 A schematic diagram of the setup for the microscopic electroluminescence measurement.

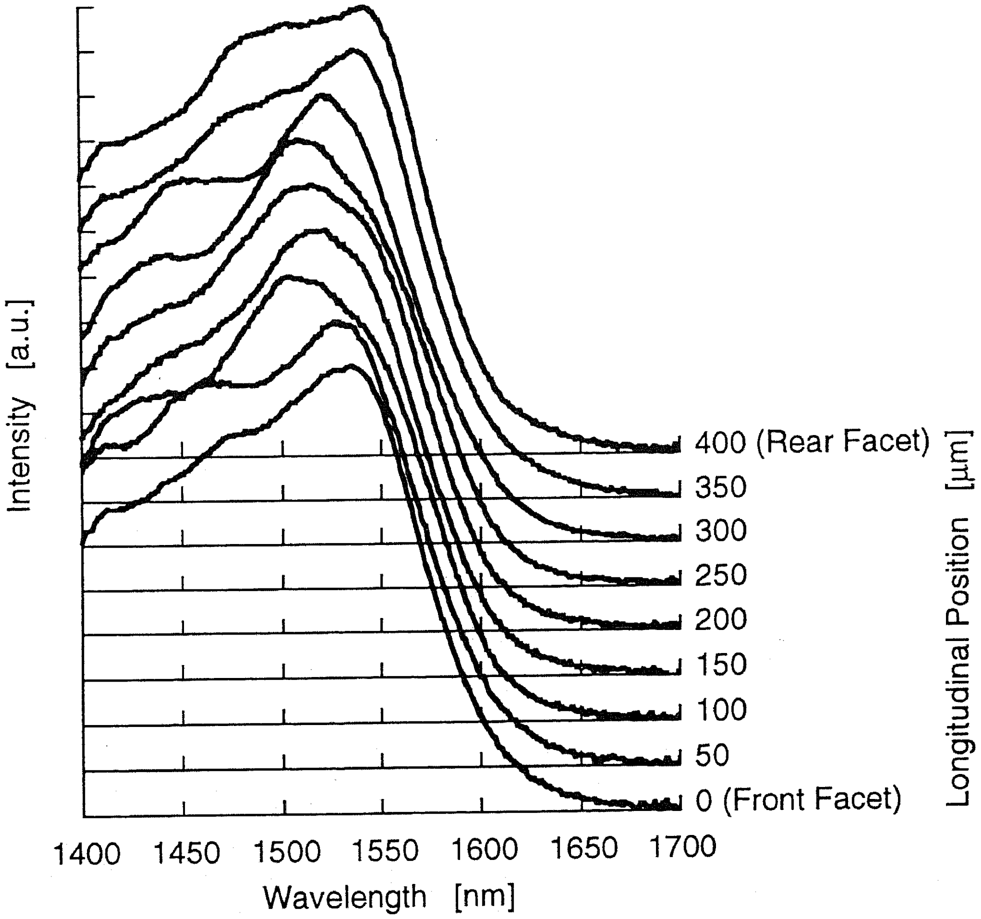

Fig. 4.24 Spontaneous emission spectra along the cavity.

refractive index distribution into the laser cavity. The wavelength shift in a Fabry-Perot cavity through the refractive index change is determined by the average of refractive index change along the whole cavity. On the other hand, in a cavity which consists of the diffraction grating, the phase shift is induced by the refractive index distribution, therefore, not only the total amount of the refractive index change, but also the position where its refractive index changes affect the resonance condition. As a consequence, the different shifts of the DFB and Fabry-Perot (FP) modes are observed in Figs. 4.17. In Fig. 4.17 (a), below the threshold, the total amount of the shift in FP mode was 0.31 nm while the shift of DFB mode was 0.23 nm. On the other hand in Fig. 4.17 (b), above the threshold, the total amount of the shift in FP mode was 0.42 nm while the shift of DFB mode was 0.36 nm. Around 1552 nm next to the stop band, it can be observed that the change in peak profile due to the interference between the FP mode and the DFB mode. Likewise, the degradation of the side mode suppression ratio in Fig. 4.17 (b) can be attributed to the nonuniform refractive index distribution along the cavity.

This distribution can be avoided by using the cylindrical lens to collimate only one axis of the beam perpendicular to the laser waveguide, or scanning the beam along the cavity. The uniform disordering may contribute to the further increase of wavelength shift.

Next, we have carried out the measurement of the lateral distribution of the disordering. High spatial selectivity of the PAID process, especially in the lateral direction is necessary for the application of the PAID process to multiple-wavelength DFB laser arrays where each DFB laser is closely placed.

The lateral distribution was characterized through measuring the photo-luminescence from the output facet. Figure 4.26 shows a schematic diagram of the measurement setup. An Ar ion laser operating continuous wave at wavelength of 514.5 nm was used for the pump source. This pump light was coupled into the fiber probe via a coupler. The fiber probe was used for the irradiation of the pump light, and at the same time, the collection of the photo-luminescence from the output of the sample. The alignment of the fiber probe was done by monitoring the absorption photo-current from the sample. The PL spectra were observed by the optical spectrum analyzer.

Figure 4.27 shows the PL spectra from the facet of the sample measured at different positions in the lateral direction. Due to the sweep out of the excited carriers from the active region, the intensity of the luminescence at the ridge waveguide is weak thus it contains large noise. The luminescence far from the waveguide is not affected by this carrier sweep effect since the diffusion length of the exited carrier is around 1 μm.

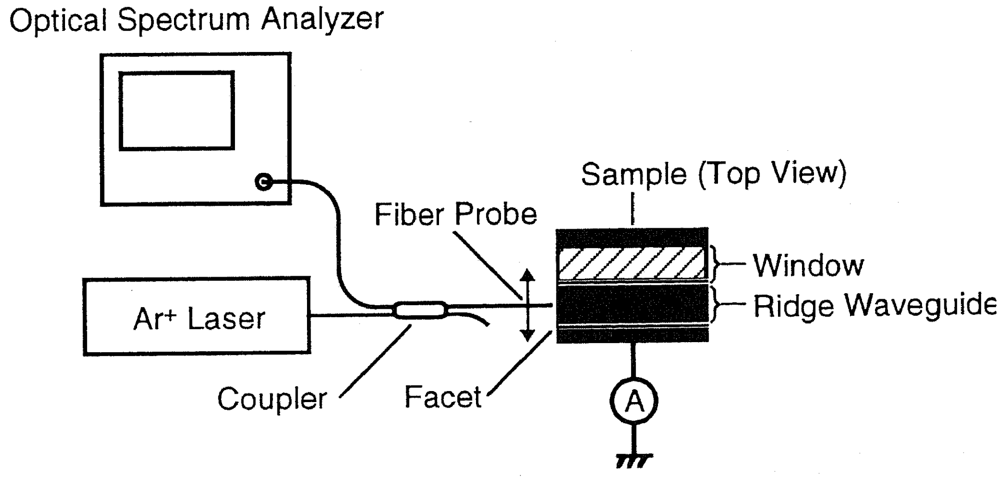

Fig. 4.25 A schematic diagram of the setup for the microscopic photoluminescence measurement.

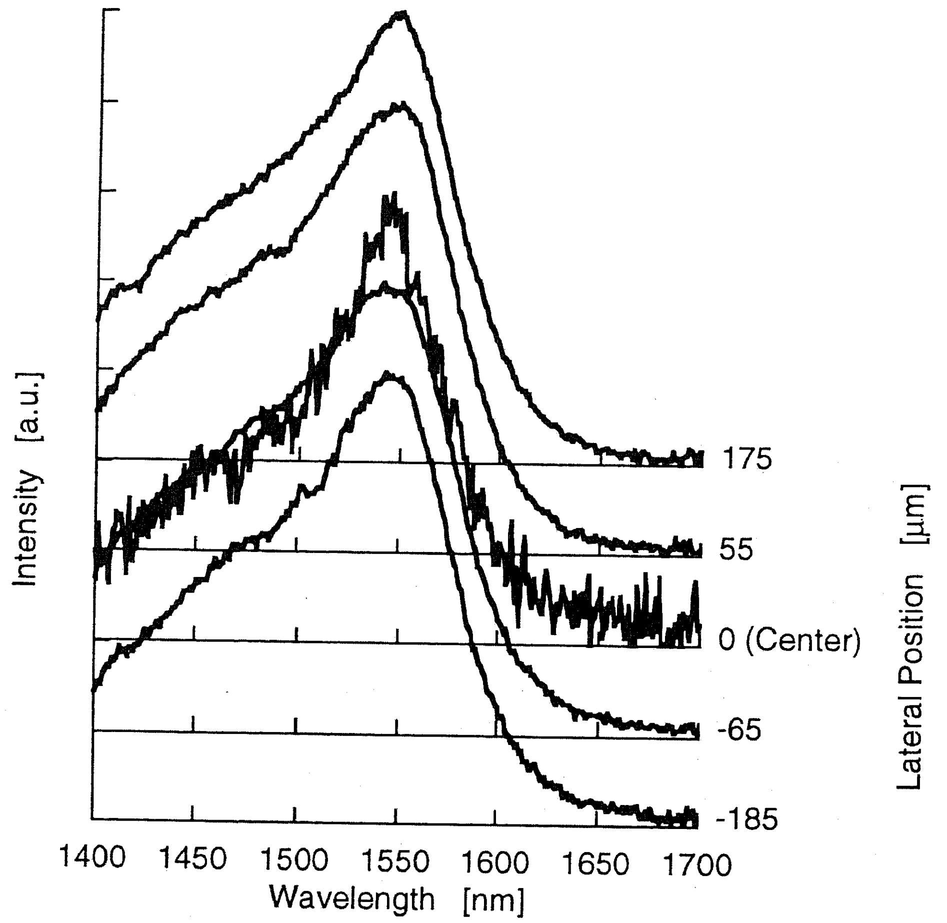

Fig. 4.26 Photo-luminescence spectra along the output facet.

No observable shift in the PL spectra was found in the lateral direction. From the previous measurement of the longitudinal distribution of the disordering, the extent of the disordering near the facet was small, therefore, the PL from the facet reflects only a part of the information on the lateral distribution of the disordering. In conclusion, further investigation on this topic is necessary for the application of the wavelength trimming by the PAID process to the laser arrays.

4.6.3 Process Control by Absorption Photocurrent Monitoring

Here we propose a process control of PAID through the absorption photo-current monitoring. As described above, the disordering obeys the product of the temperature and the duration of the process. In practice, the absolute temperature is not necessary for the process control. The temperature is determined by the incident power density, thus the quantitative control of the temperature between each process can be realized by monitoring the absorption photocurrent from the sample, since it is proportional to the incident power. This method is quite simple and it is an in-situ monitoring of the process.

4.7 Conclusions

In this chapter, we have proposed the use of PAID process for the wavelength trimming, in order to expand the wavelength adjustment range. The amount of the wavelength shift through the effective refractive index change is determined by the product of the refractive index change and the optical confinement factor, thus, the increase of both parameters are required to accomplish the substantial wavelength adjustment. The PAID process enables us to do a permanent change of refractive index in quantum well active layer, where most of the optical field is confined, through external laser beam irradiation. We have applied this process to the conventional 1.55 μm ridge waveguide index-coupled DFB laser and demonstrated 0.36 nm trimming. This shift is 2~3 times larger than the previous demonstration described in Chapter 2, where the wavelength trimming was realized by making use of the photo-induced refractive index change in chalcogenide glasses.

This method does not need any uncommon material nor special process. Moreover it relies only on the preferential absorption of the laser beam energy in quantum well active regions, thus being applicable to any type of waveguide structures.

References

[1] L. L. Chang and A. Koma, "Interdiffusion between GaAs and AlAs", Appl. Phys. Lett., vol. 29, pp. 138-141, 1976.

[2] W. D. Laidig, N. Holonyak, Jr., M. D. Camras, K. Hess, J. J. Coleman, P. D. Dapkus, and J. Bardeen, "Disorder of an AlAs-GaAs superlattice by impurity diffusion", Appl. Phys. Lett., vol. 38, pp. 776-778, 1981.

[3] N. Holonyak, Jr., W. D. Laidig, M. D. Camras, J. J. Coleman, and P. D. Dapkus, "IR-red GaAs-AlAs superlattice layer monolithically integrated in a yellow-gap cavity", Appl. Phys. Lett., vol. 39, pp. 102-104, 1981.

[4] J. H. Marsh, S. I. Hansen, A. C. Bryce, and R. M. De La Rue, "Applications of neutral impurity disordering in fabricating low-loss optical waveguides and integrated waveguide devices", Opt. Quantum Electron., vol. 23, pp. 941-957, 1991.

[5] M. Kawabe, N. Matsuura, N. Shimizu, F. Hasegawa, and Y. Nannichi, "Disordering of a Si-doped AlAs/GaAs superlattice by annealing", Jpn. J. Appl. Phys., vol. 23, pp. L623-624, 1984.

[6] R. Thornton, J. E. Epler, and T. L. Paoli, "Monolithic integration of a transparent dielectric waveguide into an active laser cavity by impurity induced disordering", Appl. Phys. Lett., vol. 51, pp. 1983-1985, 1987.

[7] J. J. Coleman, P. D. Dapkus, C. G. Kirkpatrick, M. D. Camras, and N. Holonyak, Jr., "Disorder of an AlAs-GaAs superlattice by silicon implantation", Appl. Phys. Lett., vol. 40, pp. 904-906, 1983.

[8] D. G. Deppe, L. J. Guido, N. Holonyak, Jr., K. C. Hsieh, R. D. Burnham, R. L. Thornton, and T. L. Paoli, "Stripe-geometry quantum well heterosutructure $Al_xGa_{1-x}As$-GaAs lasers difined by defect diffusion", Appl. Phys. Lett., vol. 49, pp. 510-512, 1986.

[9] C. J. McLean, J. H. Marsh, R. M. De La Rue, A. C. Bryce, B. Garrett, R. W. Glew, "Layer selective disordering by photoabsorption-induced thermal diffusion in InGaAs/InP based multiquantum well structures", Electron. Lett., vol. 28, pp. 1117-1119, 1992.

[10] C. J. McLean, A. McKee, J. H. Marsh, R. M. De La Rue, "Lateral control of the bandgap in GaInAs/GaInAsP MQW structures using photoabsorption-induced disordering", Electron. Lett., vol. 29, pp. 1657-1659, 1993.

[11] G. Lullo, A. McKee, C. J. McLean, A. C. Bryce, C. Button, J. H. Marsh, "Fabrication of electroabsorption optical modulators using laser disordered GaINAs/GaInAsP multiquantum well structures", Electron. Lett., vol. 30, pp. 1623-1625, 1994.

[12] A. McKee, C. J. McLean, A. C. Bryce, R. M. De La Rue, J. H. Marsh, C. Button, "High quality wavelength tuned multiquantum well GaInAs/GaInAsP lasers fabricated using photoabsorption induced disordering", Appl. Phys. Lett., vol. 65, pp. 2263-2265, 1994.

[13] C. J. McLean, A. Mckee, G. Lullo, A. C. Bryce, R. M. De La Rue, J. H. Marsh, "Quantum well intermixing with high spatial selectivety using a pulsed laser technique", Electron. Lett., vol. 31, pp. 1285-1286, 1995.

[14] A. Yariv, "Optical electronics", 3rd ed., Holt, Rinehart and Winston, Inc., New York, 1985.

[15] S. M. Sze, "Physics of semiconductor devices", 2nd ed., John Wiley & Sons, Inc., New York, 1981.

Chapter 5

Wavelength Trimming by Magneto-Optic Effect

5.1 Introduction

So far, we have demonstrated the wavelength trimming by making use of the photo-induced refractive index change in Chapter 3 and the photo-absorption-induced disordering in Chapter 4. Both methods utilize the effective refractive index change through the external light irradiation. As described in Chapter 2, the oscillation wavelength of DFB lasers is affected by the structure and optical properties of the laser waveguide. Thus, there is another possibility to realize the wavelength trimming without using the change of effective refractive index. In this chapter, we propose a new method which enables the wavelength trimming through a change of resonance condition. This method makes use of the magnetic material which is widely used as a memory. We will consider recording the resonance condition in a magnetic material through the magneto-optic effect, that is an interaction between the magnetic material and the optical field.

5.2 Magneto-Optic Effect

A variety of interactions between the magnetic field and the optical field in the material are known as the magneto-optic effect. Here, the Faraday effect and the Kerr effect which affect the polarization of the optical field are considered [1]. Both effects are schematically illustrated in Fig. 5.1. The magnetic field H is applied parallel to the propagation direction of the incident optical field E. In the Faraday effect, the polarization of transmitted optical field through the magnetic material rotates. On the other hand in the Kerr effect, the polarization of reflected optical field rotates. These effects are used in an optical isolator and a magneto-optic disk as a memory, respectively. The principle of both effects is the same and the rotation angle of the polarization is proportional to the intensity of magnetic field. We consider applying the Kerr effect to the wavelength trimming.

5.3 Concept of Wavelength Trimming by Kerr Effect

Figure 5.2 illustrates a concept of wavelength trimming in a Fabry-Perot semiconductor laser by making use of the Kerr effect. The cavity consists of the left facet of the active medium and the interface between the active medium and the magnetic

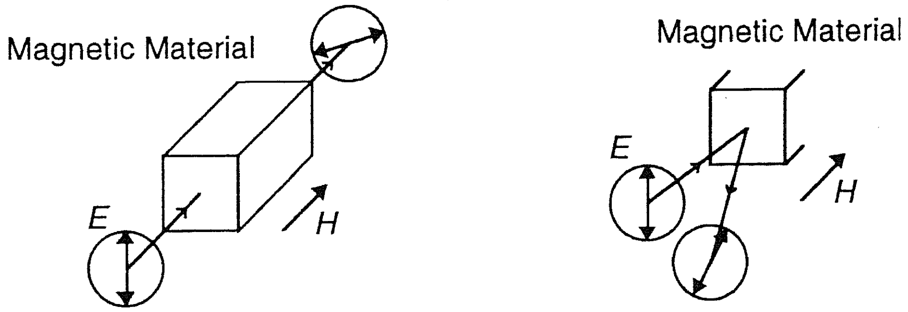

(a) Faraday effect (b) Kerr effect

Fig. 5.1 Concepts of magneto-optic effects.

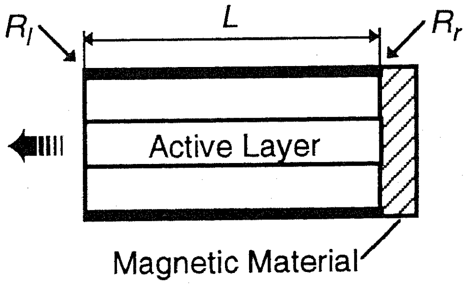

Fig. 5.2 Concept of wavelength trimming by magneto-optic effect in Fabry-Perot laser.

material. The cavity length is L, and the reflectivities of the left and right facets are R_l and R_r, respectively. It is assumed that the gain in the active medium has an anisotropy and contributes to a mode with a specific polarization. When the magnetic material is not magnetized, the optical field incident on the right mirror reflects without rotating its polarization. The reflectivity of the right facet R_r in this case is defined as R_{r0}. When the magnetic material is magnetized by applying the external magnetic field, the polarization of the reflected optical field rotates. This means that a new mode with polarization perpendicular to the original mode is excited. The gain in the active medium does not contribute to this new mode, therefore, the reflectivity of the right facet is effectively reduced. Assuming that the rotation angle of the polarization is θ, the reflectivity of the right facet can be expressed as

$$R_r = R_{r0} \cos\theta . \quad (5.1)$$

Next, we consider the shift in oscillation wavelength caused by the reflectivity change. Here it is explained in a qualitative manner. In the semiconductor laser, the carrier density in the cavity is always clamped at the threshold condition where the gain is equal to the loss. By applying the external magnetic field to the mirror which consists of the magnetic material, the reflectivity is reduced. This reduction of the reflectivity results in the increase of the loss, and therefore, the carrier density increases to maintain the threshold condition. In the semiconductor active medium, not only the gain but also the refractive index is changed by the carrier density variation. Near the band edge of the semiconductor active medium where the laser oscillates, the refractive index decreases as the carrier density increases. Consequently, the oscillation wavelength shifts towards the shorter wavelength side by applying the external magnetic field.

By using the ferromagnetic material having the coercive force as a mirror, the record of the resonance condition can be realized without applying the external magnetic field.

We expand this concept toward the wavelength trimming in DFB lasers. Figure 5.3 illustrates a longitudinal cross section of a DFB laser having the diffraction grating which consists of the magnetic material. In this DFB laser, the coupling coefficient κ which corresponds to the reflectivity of the facet in the Fabry-Perot laser can be controlled by the external magnetic field, and it can be described as the same form of equation (5.1), thus

$$\kappa = \kappa_0 \cos\theta \qquad (5.2)$$

where κ_0 is the coupling coefficient of non-magnetized diffraction grating. The shift of the oscillation wavelength In DFB lasers through the change of the coupling

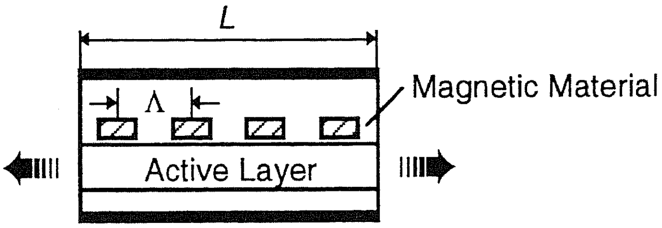

Fig. 5.3 Concept of wavelength trimming by magneto-optic effect in DFB laser where grating consists of magnetic material.

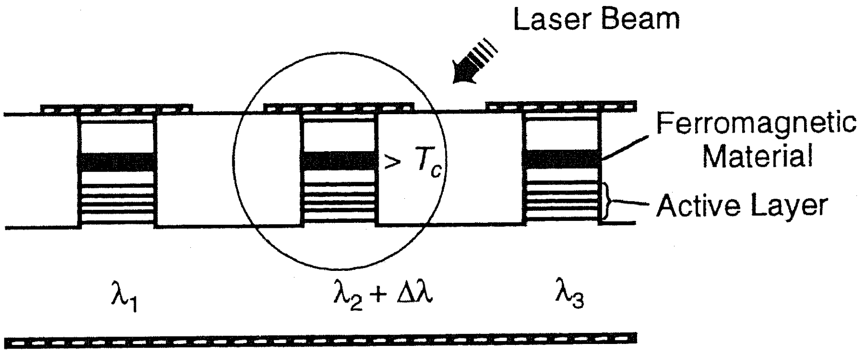

Fig. 5.4 A concept of the wavelength trimming by magneto-optic effect in a multiple-wavelength DFB laser array. An external laser beam is incident on an elemental laser, which has an oscillation wavelength error, to heat the grating consists of ferromagnetic material to a temperature above the Curie point.

coefficient can be basically explained by the same way as described above.

Next, we consider the wavelength trimming in a multiple-wavelength DFB laser array by the magneto-optic effect. In order to control the oscillation wavelength of each DFB laser in the array, it is necessary to localize the magnetization. This can be realized by pointing the high power laser beam on the DFB laser whose oscillation wavelength has an error and heating it to a temperature above the Curie point of the ferromagnetic material where it looses the ferromagnetism and becomes the paramagnetic material. Under a certain intensity of external magnetic field, the material is easily magnetized, and after stopping the irradiation that status is recorded. The concept of the wavelength trimming in a multiple-wavelength DFB laser array by the magneto-optic effect is schematically shown in Fig. 5.4. The principle described here is completely the same as used in the magneto-optic disc where each bit corresponds to an elemental DFB laser in an array.

5.4 Analysis of Wavelength Trimming by Kerr Effect

In order to estimate how large the oscillation wavelength can be changed by the magneto-optic effect, we will carry out the theoretical analysis in this section. As described in Chapter 2, the oscillation wavelength of DFB lasers is determined by the coupled-wave equation. The threshold analysis of the coupled-wave theory is summarized in Appendix A. For simplicity, both facets of the DFB laser are assumed to be anti-reflection coated. In this case, the threshold condition can be obtained by solving the eigen value equation given by [2],

$$\alpha - j\delta = \gamma \coth \gamma L. \quad (5.3)$$

Here γ is

$$\gamma^2 = \kappa^2 + (\alpha - j\delta)^2. \quad (5.4)$$

where κ is the coupling coefficient, α is the threshold gain, and δ is the normalized frequency parameter, respectively. We have numerically solved this complex transcendental equation by utilizing the Brent's method (which can be found in the mathematical subprogram library of MSL II) [3], and obtained the change in resonance condition through the coupling coefficient change.

Figures 5.5 (a) and (b) show the change in the threshold gain a and the normalized frequency parameter δ as a function of the normalized coupling coefficient κL where L is the cavity length. Both of them are normalized by the change of the coupling coefficient. In the pure index-coupling where the coupling coefficient κ is a real number, the two modes which have the same threshold gain are exist and are symmetrical with respect to the Bragg frequency.

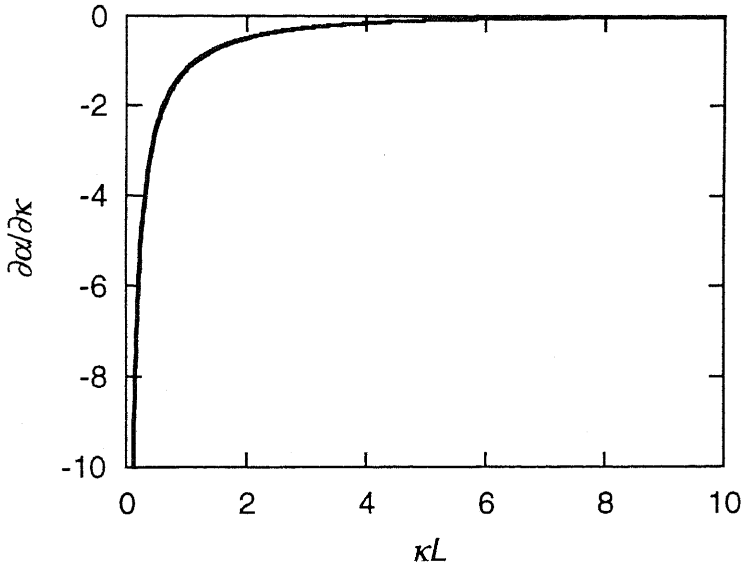

(a) threshold gain change

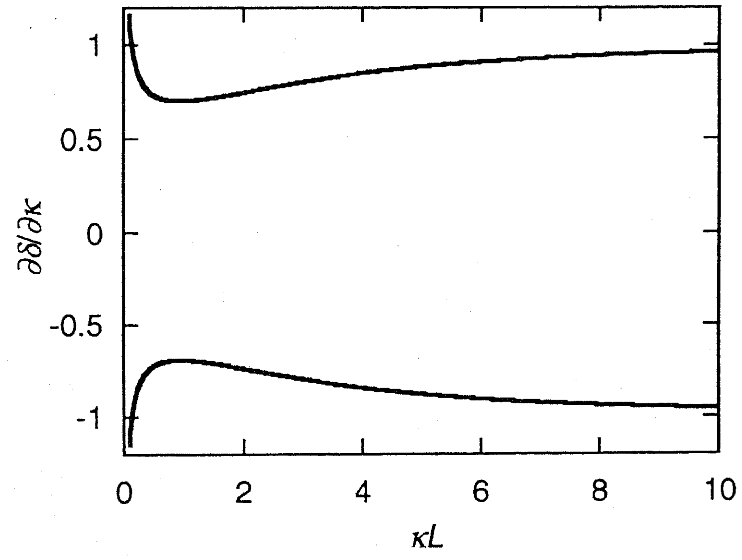

(b) resonant frequency change

Fig. 5.5 Resonant condition changes caused by coupling coefficient change.

Next, we will derive the relation between the oscillation frequency change and the resonance condition change [4]. The normalized frequency parameter δ is defined as

$$\delta \equiv \frac{\omega - \omega_b}{v_g} \qquad (5.5)$$

where ω is the oscillation frequency, ω_b is the Bragg frequency, and v_g is the group velocity. From equation (5.5), the relation between the oscillation frequency change $\Delta\omega_1$ and the change in the normalized frequency parameter is readily derived as

$$\Delta\omega_1 = v_g \frac{\partial\delta}{\partial\kappa}\Delta\kappa. \qquad (5.6)$$

The change in oscillation frequency $\Delta\omega_2$ for a change in threshold gain $\Delta\alpha$ is

$$\Delta\omega_2 = \frac{\partial\omega}{\partial\beta}\frac{\partial\beta}{\partial\alpha}\Delta\alpha \qquad (5.7)$$

where β is a propagation constant. The first term in the right side can be represented by

$$\frac{\partial\omega}{\partial\beta} = v_g. \quad (5.8)$$

The second term becomes

$$\frac{\partial\beta}{\partial\alpha} = \frac{\frac{2\pi\partial n_r}{\lambda}}{\frac{2\pi\partial n_i}{\lambda}} \qquad (5.9)$$

$$= \frac{\partial n_r}{\partial n_i} \qquad (5.10)$$

where λ is the free space wavelength, ∂n_r and ∂n_i are the change in the real and imaginary part of the refractive index, respectively. The ratio of ∂n_r and ∂n_i is a linewidth enhancement factor a defined as [5],

$$a \equiv \frac{\partial n_r}{\partial n_i}. \qquad (5.11)$$

Finally, we obtain

$$\Delta\omega_2 = v_g a \frac{\partial\alpha}{\partial\kappa}\Delta\kappa. \qquad (5.12)$$

Therefore, the total amount of oscillation frequency shift caused by the resonance condition change is

$$\Delta\omega = \Delta\omega_1 + \Delta\omega_2$$

$$= \frac{v_g}{L}\left(a\frac{\partial\alpha}{\partial\kappa} + \frac{\partial\delta}{\partial\kappa}\right)\Delta\kappa L. \qquad (5.14)$$

Here, using equation (5.14), we will estimate the order of uppermost oscillation frequency shift by the wavelength trimming through the magneto-optic effect. Assuming that $v_g = 1\times10^8$ m/s, $a = 6$, $L = 200$ μm, and $\kappa_0 L = 1$, respectively. In Fig. 5.5, $\partial\alpha/\partial\kappa$ and $\partial\delta/\partial\kappa$ at $\kappa L = 1$ are -1.2 and -0.7, respectively. Here, the mode which has the normalized frequency parameter shift towards the minus direction is chosen. Using these values in equation (5.14) gives

$$\Delta\omega \approx -4\times10^{12}\Delta\kappa L. \qquad (5.15)$$

We shall assume a diffraction grating consists of a Cobalt having the Kerr rotation angle θ of 1 °. Thus, the change of normalized coupling coefficient is

$$\Delta\kappa L = \kappa_0 L(\cos\theta - 1) \qquad (5.16)$$

$$\approx -1.5\times10^{-4}$$

Substituting this value into equation (5.15), we obtain the frequency shift Δf of ~100 MHz. Although this value is small under the conditions assumed above, it can be increased by using the ferromagnetic material with large Kerr rotation angle.

5.5 Conclusions

In this chapter, we have proposed the wavelength trimming through the resonance condition change by the magneto-optic effect. By using the ferromagnetic material having the coercive force, the resonance condition can be changed and recorded by applying the external magnetic field. We have carried out the theoretical analysis on the frequency change in the DFB laser with the diffraction grating consisted of the magnetic material, and reached the conclusion that it is necessary to develop the ferromagnetic material with large Kerr rotation angle to achieve the substantial change in oscillation wavelength through the resonant condition change.

References

[1] M. Born and E. Wolf, "Principle of optics", 6th ed., Pergamon, 1980.

[2] H. Kogelnik and C. V. Shank, "Coupled-wave theory of distributed feedback lasers", J. Appl. Phys., vol. 43, pp. 2327-2335, 1972.

[3] J. J. More and M. Y. Cosnard, "Numerical solution of nonlinear equations", ACM Transaction on Mathematical Software, vol. 5, no. 1, pp. 64-85, March 1979.

[4] T. Tamir, ed., "Guided-wave optoelectronics", 2nd ed., Springer-Verlag, Berlin, Heidelberg, 1990.

[5] C. H. Henry, "Theory of the linewidth of semiconductor lasers", IEEE J. Quantum Electron., vol. QE-18, pp. 259-264, 1982.

Chapter 6

Conclusions

The securement of wavelength reproducibility is urgent and vital task for the realization of multiple-wavelength distributed-feedback semiconductor laser arrays. In order to cope with this difficulty, we have proposed the wavelength trimming technology where the oscillation wavelength error is corrected after the device fabrication without using external active tuning, and realized this concept in different methods.

Our wavelength trimming concept came from an analogy to the trimming technology in analogue integrated circuits.

The key issue for embodying the concept of wavelength trimming is how to incorporate a material whose optical property is changeable after the device fabrication by a simple and low temperature process into the laser waveguide. This process should not induce any physical damage in the laser. Furthermore, long-term stability of the optical properties after processing is also requested.

On the basis of these requirements, we have examined the possibility of wavelength trimming by the photo-induced refractive index change in chalcogenide glasses, the photo-absorption-induced quantum well disordering, and the magneto-optic effect. First two methods utilized the refractive index change of the material through the external light irradiation. The use of the external light beam for the wavelength trimming allows us to localize the region where the refractive index changes, and thereby it is possible to adjust oscillation wavelength of elemental DFB lasers, one after another, within an array. The last method made use of the resonant condition change. The following are the conclusions of each method.

Wavelength Trimming by the Photo-Induced Refractive Index Change

We have utilized the Se-based chalcogenide glass having the photo-induced refractive index change of 1 % as a constituent of the laser waveguide, and demonstrated the wavelength trimming of 0.14 nm in a 1.55 μm index-coupled DFB laser. Using this method, the oscillation wavelength of the DFB laser is adjustable through the irradiation time. Although the direction of the oscillation wavelength shift induced by the light irradiation is towards the shorter-wavelength side, it is possible to restore the trimmed wavelength to the initial value through the heat treatment.

Wavelength Trimming by the Photo-Absorption-Induced Disordering

The amount of the wavelength shift through the effective refractive index change is determined by the product of the refractive index change and the optical confinement factor, thus, the increase of both parameters is required to accomplish the substantial wavelength adjustment. The PAID process enables us to do a permanent change of refractive index in quantum well active layer, where most of the optical field is confined, through external laser beam irradiation. We have applied this process to the conventional 1.55 μm ridge waveguide index-coupled DFB laser and demonstrated 0.36 nm trimming. This shift is 2~3 times larger than the previous demonstration, where the wavelength trimming was realized by making use of the photo-induced refractive index change in chalcogenide glasses.

This method does not need any uncommon material nor special process. Moreover it relies only on the preferential absorption of the laser beam energy in quantum well active regions, thus being applicable to any type of waveguide structures.

Wavelength Trimming by the Magneto-Optic Effect

We have proposed the wavelength trimming by the magneto-optic effect as one example among various possibilities.

By using the ferromagnetic material having the coercive force, the resonance condition of lasers can be changed and recorded by applying the external magnetic field. This wavelength trimming does not involve the refractive index change of the material, but it utilizes the rotation of the polarization of the optical field through the magneto-optic effect. We have carried out the theoretical analysis on the frequency change in the DFB laser with the diffraction grating consisted of the magnetic material.

The straightforward way to counter the variation in oscillation wavelength of DFB lasers is the improvement of global uniformity in growth and fabrication. This method is the best of all countermeasures including the wavelength trimming technology. Although there have been significant improvements in the epitaxial growth and dry etching technologies, the current uniformity is still insufficient. Even in the well-matured electronics, the trimming technology is widely used to compensate the variation of the characteristics caused by the fabrication error, thus our wavelength trimming technology will surely make a contribution to the improvement of the wavelength reproducibility and, consequently, the device yield of multiple-wavelength DFB laser arrays.

Appendix

Coupled-Wave Theory of DFB Lasers

Here we summarize the coupled-wave theory of DFB lasers and its threshold analysis [1]-[3]. Assuming that a DFB laser considered here has a cavity length of L, reflectivities of left and right facets of R_l and R_r, and a periodic variation in the refractive index $n(z)$ and in the gain constant $a(z)$ of the form,

$$n(z) = n + \Delta n \cos\left(\frac{2\pi z}{\Lambda} + \Omega\right) \qquad \text{(A.1a)}$$

$$\alpha(z) = \alpha + \Delta\alpha \cos\left(\frac{2\pi z}{\Lambda} + \Omega\right), \qquad \text{(A.1b)}$$

where n and α are the average values, and Δn and $\Delta\alpha$ are the amplitude variations with spatial period Λ and phase Ω. Here z is measured along the laser from $-L/2$ to $L/2$. The complex reflectivities can be written as

$$R_l = |R_l| \exp\left(-\frac{j\pi}{\Lambda} L + \Omega\right) = |R_l| \exp(j\theta_l) \qquad \text{(A.2a)}$$

$$R_r = |R_r| \exp\left(-\frac{j\pi}{\Lambda} L - \Omega\right) = |R_r| \exp(j\theta_r), \qquad \text{(A.2b)}$$

where θ_l and θ_r are the facet phases, which represent the relative positions of the facets to the grating phases at $z = -L/2$ and $z = L/2$, respectively. The scalar wave equation for the electric field E with time dependence of $\exp(j\omega t)$ satisfies,

$$\frac{\partial^2}{\partial z^2} E(z) + k^2(z) E(z) = 0, \qquad \text{(A.3)}$$

where

$$k^2(z) = \beta^2 + 2j\alpha\beta + 4\kappa\beta \cos(2\beta_0 z + \Omega) \qquad \text{(A.4)}$$

Here

$$\beta_0 \equiv \pi/\Lambda \qquad \text{(A.5a)}$$

$$\beta \equiv n\omega/c \qquad \text{(A.5b)}$$

and κ is the coupling coefficient given by

$$\kappa = \frac{\beta}{2}\frac{\Delta n}{n} + \frac{j\Delta\alpha}{2} \qquad \text{(A.6)}$$

Without loss of generality, the electric field in the DFB structure can be expressed as the sum of two counterrunning waves $R(z)$ and $S(z)$, therefore,

$$E(z) = R(z)\exp(-j\beta_0 z) + S(z)\exp(j\beta_0 z). \quad \text{(A.7)}$$

Substituting the equation (A.7) into the scalar wave equation (A.3), the coupled-wave equations are derived as,

$$-\frac{\partial R(z)}{\partial z} + (\alpha - j\delta)R(z) = j\kappa S(z) \qquad \text{(A.8a)}$$

$$\frac{\partial S(z)}{\partial z} + (\alpha - j\delta)S(z) = j\kappa R(z). \qquad \text{(A.8b)}$$

The parameter δ is a normalized frequency parameter defined by

$$\delta \equiv \frac{\beta^2 - \beta_0^2}{2\beta} \approx \beta - \beta_0 = \frac{n}{c}(\omega - \omega_0). \qquad \text{(A.9)}$$

The general form of solution of coupled-mode equation is

$$R = r_1 e^{\gamma z} + r_2 e^{-\gamma z} \qquad \text{(A.10a)}$$

$$S = s_1 e^{\gamma z} + s_2 e^{-\gamma z} \qquad \text{(A.10b)}$$

with the complex propagation constant γ obeying the dispersion relation

$$\gamma^2 = \kappa^2 + (\alpha - j\delta)^2. \quad \text{(A.11)}$$

For the special case with no reflection at both facets, γ is the solution of the eigen-value equation

$$\kappa = \frac{\pm j\gamma}{\sinh \gamma L}. \qquad \text{(A.12)}$$

For the general case with reflectivities of R_l and R_r at the left and right facets, γ is the solution of the transcendental equation

$$\frac{\left(1 - R_l \dfrac{\Gamma}{j\kappa}\right)\exp(-\gamma L)}{\left(R_l - \dfrac{\Gamma}{j\kappa}\right)} = \frac{\left(R_r - \dfrac{\Gamma}{j\kappa}\right)\exp(\gamma L)}{\left(1 - R_r \dfrac{\Gamma}{j\kappa}\right)} \qquad \text{(A.13)}$$

where

$$\Gamma = -\gamma + \alpha - j\delta. \qquad \text{(A.14)}$$

The solution of equation (A.12) or (A.13) gives us the resonant condition, namely, the gain and the frequency at threshold.

References

[1] H. Kogelnik and C. V. Shank, “Coupled-wave theory of distributed feedback lasers”, J. Appl. Phys., vol. 43, pp. 2327-2335, 1972.

[2] S. R. Chinn, “Effects of mirror reflectivity in a distributed-feedback laser”, IEEE J. Quantum Electron., vol. QE-9, pp. 574-580, 1973.

[3] W. Streifer, R. D. Burnham, and D. R. Scifres, “Effect of external reflectors on longitudinal modes of distributed feedback lasers”, IEEE J. Quantum Electron., vol. QE-11, pp. 154-161, 1975.